Heat Transfer in Large Two-Stroke Marine Diesel Engines

Jensen, Michael Vincent

Publication date:
2013

Document Version
Publisher's PDF, also known as Version of record

Heat Transfer in Large Two-Stroke Marine Diesel Engines

PhD Thesis

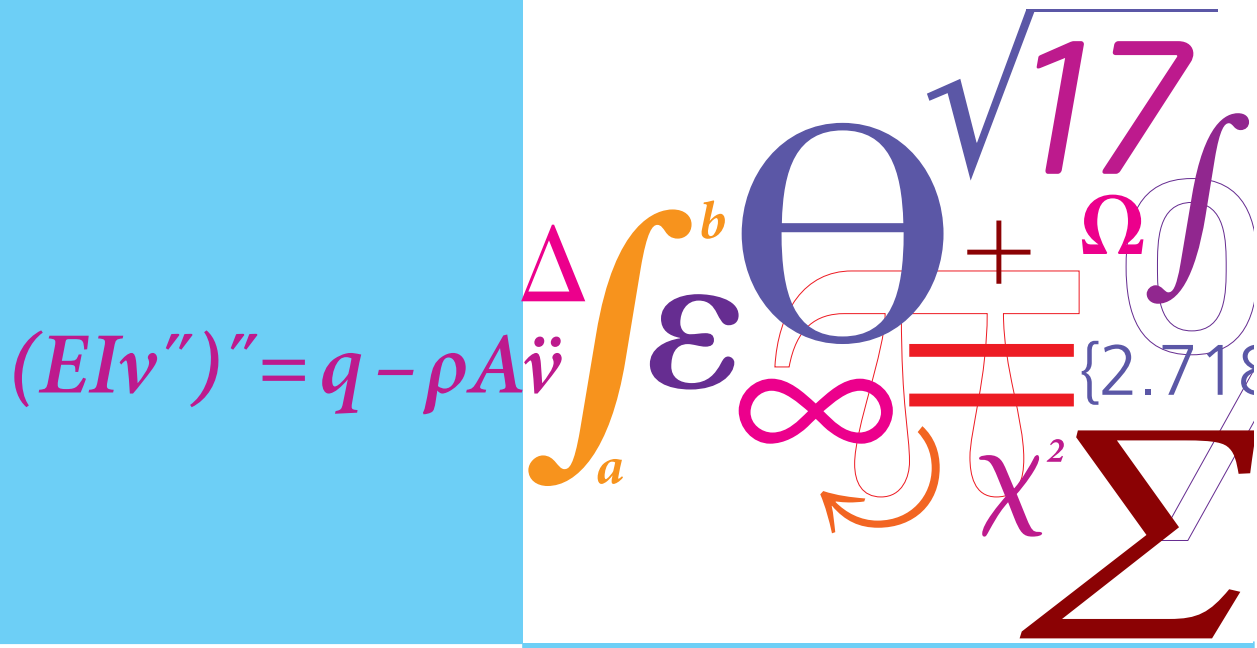

Michael Vincent Jensen
DCAMM Special Report No. S157
August 2012

DTU Mechanical Engineering
Department of Mechanical Engineering

Heat Transfer in Large Two-Stroke Marine Diesel Engines

by

Michael Vincent Jensen

A thesis submitted in partial fulfillment of the requirements for the degree of

DOCTOR OF PHILOSOPHY

at the

TECHNICAL UNIVERSITY OF DENMARK

2012

Heat Transfer in Large Two-Stroke Marine Diesel Engines

Michael Vincent Jensen

Section of Fluid Mechanics, Coastal and Maritime Engineering
Department of Mechanical Engineering
Technical University of Denmark
Nils Koppels Allé, Bld. 403
DK-2800 Kgs. Lyngby
Denmark

Ph.D. Thesis

ISBN: 978-87-7475-364-3
DCAMM Special Report no.: S157

Preface

This thesis is submitted in partial fulfillment of the requirements for the Ph.D. degree in Mechanical Engineering at the Technical University of Denmark.

The work presented in the thesis was carried out at the Department of Mechanical Engineering at the Technical University of Denmark in the period from February 2007 to August 2012 under the supervision of Associate Professor Jens Honoré Walther, Professor Henrik Carlsen and Associate Professor Jesper Schramm.

The work was conducted in collaboration with MAN Diesel & Turbo, and it was funded by the Technical University of Denmark, MAN Diesel & Turbo and the Danish Center for Applied Mathematics and Mechanics, DCAMM.

During the work, an external research stay was conducted at the Engine Research Center at the University of Wisconsin-Madison in the USA in the period from May 2009 to August 2009 under the guidance of Professor Christopher Rutland.

Kgs. Lyngby, August 2012

Michael Vincent Jensen

Abstract

Heat transfer between the cylinder gas and the piston surface during combustion in large two-stroke uniflow scavenged marine diesel engines has been investigated in the present work. The piston surface experiences a severe thermal load during combustion due to the close proximity of the combustion zone to the surface. At the same time, cooling of the piston crown is relatively complicated. This can cause large thermal stresses in the piston crown and weakening of the material strength, which may be critical as it can lead to formation of cracks. Information about the piston surface heat transfer is thus important for the engine manufactures.

The piston surface heat transfer was studied in the event of impingement of hot combustion products on the piston during combustion, and an estimate was obtained of the peak heat flux level experienced on the piston surface. The investigation was carried out numerically by performing simulations with a CFD code of the heat transfer between gas and wall in a jet impingement configuration where a hot round turbulent gas jet impinged normally onto a wall under conditions approximating the in-cylinder conditions in the engine during combustion.

A jet impingement reference case was first established based on estimations of the in-cylinder conditions during combustion. Subsequently, variations of different jet impingement parameters were performed and the influence on the wall heat transfer was observed. In all the cases, the ratio between the jet inlet to wall distance, H, and the jet diameter at the inlet, D, was $H/D = 2$. The jet Reynolds number, Re, varied between $1.10 \cdot 10^5$ and $6.64 \cdot 10^5$. The resulting Nusselt numbers along the wall were calculated for dimensionless radial distances from the stagnation point, r/D, between 0 and 6.

The maximum Nusselt number was located in the stagnation point in most of the investigated cases, and an analysis was performed of the variation of the stagnation point Nusselt number, Nu_0, with the jet Reynolds number and the jet turbulence intensity at the jet inlet, TI. Based on the observed relations, a correlation between Nu_0, Re and TI is suggested for high jet Reynolds number cases. A satisfactory validation of the correlation was not possible to perform due to insufficient available experimental data. A comparison of the correlation predictions to existing experimental data indicated however an overprediction of Nu_0 in the magnitude of 50% – 100%. The overprediction is considered to be caused primarily by incorrect numerical model predictions.

Based on the performed jet impingement heat transfer investigations, an estimate is provided of the peak convective piston surface heat flux level experienced in the considered large marine diesel engines. The contribution from thermal radiation to the piston surface heat flux was not investigated in the present work, but a coarse estimation of the magnitude was performed. The obtained estimations indicate a peak piston surface heat flux level in the interval from about 1 MW/m^2 and up to 9.5 MW/m^2 with the actual value probably being in the lower part of this interval. This is about the same magnitude as that previously reported for automotive size diesel engines. The obtained interval is

relatively large, but a more accurate prediction is difficult to achieve with the applied method due to limited knowledge about the actual local in-cylinder conditions during combustion. Therefore, further research in this area is encouraged.

Resumé (abstract in Danish)

Varmetransmissionen mellem cylindergassen og stempeloverfladen under forbrændingsprocessen i store to-takts marine-dieselmotorer med længdeskylning er blevet undersøgt i dette arbejde. Stempeloverfladen udsættes for en hård termisk belastning under forbrændingen, da forbrændingszonen er relativt tæt på overfladen. Stempelkronen er samtidig relativt kompliceret at køle. Dette kan forårsage store termiske spændinger i stempelkronen og svækkelse af materialets styrke, hvilket kan være kritisk, da det kan føre til revnedannelse. Information om varmetransmissionen til stempeloverfladen er således vigtig for motorproducenterne.

Varmetransmissionen til stempeloverfladen ved kollision mellem varme forbrændingsprodukter og stempeloverflade under forbrændingsprocessen er blevet undersøgt, og niveauet af den maksimale varmeflux, som forekommer på overfladen, er blevet estimeret. Undersøgelsen blev foretaget numerisk ved at udføre simuleringer med et CFD program af varmetransmissionen mellem gas og væg i en konfiguration, hvor en varm rund turbulent gas jet kolliderede med en væg vinkelret på jetten under forhold, som tilnærmer forholdene i motoren under forbrændingsprocessen.

Et reference case blev først etableret baseret på estimater af forholdene i motoren under forbrændingsprocessen. Efterfølgende blev en variation af forskellige konfigurationsparametre foretaget, og indflydelsen på varmetransmissionen mellem gas og væg blev observeret. Forholdet mellem afstanden fra jetindløb til væg, H, og jetdiameteren ved indløbet, D, var $H/D = 2$ i alle de undersøgte tilfælde. Jet Reynolds-tallet, Re, varierede mellem $1.10 \cdot 10^5$ and $6.64 \cdot 10^5$. De resulterende Nusselt-tal langs væggen blev beregnet for dimensionsløse radiale afstande fra stagnationspunktet, r/D, mellem 0 og 6.

I de fleste undersøgte tilfælde forekom det højeste Nusselt-tal i stagnationspunktet, og en analyse blev foretaget af variationen af Nusselt-tallet i stagnationspunktet, Nu_0, med jet Reynolds-tallet og turbulensintensiteten i jetten ved jetindløbet, TI. Baseret på de observerede relationer er en korrelation mellem Nu_0, Re og TI foreslået for tilfælde med høje jet Reynolds-tal. Det har ikke været muligt at foretage en tilfredsstillende validering af den foreslåede korrelation, da tilstrækkelige eksperimentelle data ikke har været til rådighed. En sammenligning af Nu_0-resultater beregnet med den foreslåede korrelation og eksisterende eksperimentelle data viste dog at korrelationsresultaterne lå i størrelsesordenen 50% – 100% over de eksperimentelle data. Formentlig skyldes uoverensstemmelsen hovedsagligt ukorrekte modelforudsigelser i de numeriske simuleringer.

Baseret på de foretagne varmetransmissionsundersøgelser er et estimat givet af det maksimale konvektive varmefluxniveau, som forekommer på stempeloverfladen i de betragtede store marine-dieselmotorer. Bidraget fra termisk stråling til varmefluxen på stempeloverfladen blev ikke undersøgt i dette arbejde, men et groft estimat af bidragets størrelsesorden er foretaget. De opnåede estimater indikerer at niveauet af den maksimale

varmeflux på stempeloverfladen ligger i intervallet fra omkring 1 MW/m^2 og op til 9.5 MW/m^2 og sandsynligvis i den nedre del af dette interval. Det er i samme størrelsesorden som niveauer målt i mindre dieselmotorer. Det estimerede interval er relativt stort, men det er vanskeligt at foretage et mere præcist estimat med den anvendte metode på grund af begrænset viden omkring de faktiske lokale forhold i de betragtede motorer under forbrændingsprocessen. Der opfordres derfor til fortsat arbejde indenfor dette område.

Acknowledgements

I would like to express my gratitude to my supervisors, Associate Professor Jens Honoré Walther, Professor Henrik Carlsen and Associate Professor Jesper Schramm, for their guidance and support. In particular, I thank my principal supervisor Associate Professor Jens Honoré Walther for many hours of constructive discussions and numerous helpful suggestions and advices as well as for continued encouragement and inspiration during the work on this thesis.

I would also like to thank MAN Diesel & Turbo for the collaboration as well as for financing part of this work. Section Manager Stefan Mayer and Research Engineer Simon Matlok from MAN Diesel & Turbo have made valuable contributions to the present work through relevant discussions and exchange of ideas and by providing important data and measurements.

The Danish Center for Applied Mathematics and Mechanics, DCAMM, is also acknowledged for its co-funding of the present work.

I am also grateful to Professor Christopher Rutland for interesting and fruitful discussions and helpful advices during my period at the Engine Research Center and for making the research stay possible, which has been a highly positive and inspiring experience both academically and personally. My thanks also go to the students at the Engine Research Center for a very inspiring, warm and welcoming atmosphere.

I would also like to thank colleagues and fellow Ph.D. students at the Department of Mechanical Engineering at DTU, and specially the people in the internal combustion engine group (ICEG), for a constructive and friendly environment to carry out the work. Particularly, I would like to thank my office roommate Caspar Ask Christiansen for many valuable conversations and a good friendship.

Finally, I am deeply grateful to my family and friends and especially to my girlfriend Nora for invaluable continued support and encouragement, and most of all, for patience and understanding throughout the work on this thesis.

List of publications

The results of the work reported in this thesis are presented in different publications, which are listed below.

I. ISI Journal Paper

M. V. Jensen and J. H. Walther, "Numerical analysis of jet impingement heat transfer at high jet Reynolds number and large temperature difference", Accepted for publication in *Heat Transfer Engineering*, vol. 34, no. 10, 2013.

The manuscript is included in Appendix B.

II. Proceedings Paper – Peer Reviewed Manuscript

M. V. Jensen and J. H. Walther, "Piston surface heat transfer during combustion in large marine diesel engines", in *Proceedings of the 26th CIMAC World Congress, Paper No. 187*, Bergen, Norway, 2010.

III. Proceedings Paper – Peer Reviewed Manuscript

M. V. Jensen and J. H. Walther, "Jet impingement heat transfer at high Reynolds numbers and large density variations", in *Proceedings of the 7th International Conference on Heat Transfer, Fluid Mechanics and Thermodynamics (HEFAT 2010),* Antalya, Turkey, 2010, pp. 925-930.

Contents

Nomenclature

Latin symbols

A	area
a	coefficient in stagnation point Nusselt number correlation
B	cylinder bore
b	coefficient in stagnation point Nusselt number correlation
C	coefficient in stagnation point Nusselt number correlation
C_1, C_2, C_{KT}	turbulence model constants
C_{ε_1}, C_{ε_2}, C_{ε_3}	turbulence model constants
C_L, C_η, C_μ	turbulence model constants
c_1, c_2, c_3, c_4	constants in stagnation point Nusselt number correlation
c_p	specific heat capacity at constant pressure
CF_T, CF_{Pr}	correction factors in Nusselt number correlation
D	jet diameter at inlet; pipe diameter; nozzle diameter
D_m	mass diffusivity
d_0	nozzle hole diameter in fuel injector
E	wall function constant
Ec	Eckert number
F	view factor
f	redistribution parameter in the V2F turbulence model
$\vec{f}$	body force pr. unit volume
Fr	Froude number
g	gravitational acceleration
H	distance between jet inlet and wall; distance between pipe exit and wall; distance between nozzle exit and wall
h	heat transfer coefficient; enthalpy
h'	enthalpy fluctuation
k	turbulent kinetic energy
k_1, k_2, k_3	constants in stagnation point Nusselt number correlation
L	distance from fuel injector nozzle; turbulence length scale; characteristic length
Nu	Nusselt number
Nu_0	stagnation point Nusselt number
Pr	Prandtl number
Pr_j	Prandtl number evaluated at jet inlet conditions
Pr_s	Prandtl number evaluated at surface conditions
Pr_∞	Prandtl number evaluated at free stream conditions
p	pressure
$\dot{Q}$	heat transfer rate
q	heat flux
q_{cd}	conductive heat flux
q_{cv}	convective heat flux
q_{rad}	radiative heat flux

q_w	wall heat flux
Re	Reynolds number; jet Reynolds number
r	radial distance from stagnation point
$\vec{r}$	position vector
S_{ij}	strain-rate tensor
Sc	Schmidt number
Sc_t	turbulent Schmidt number
T	temperature
T_a	ambient gas inflow temperature
T_f	film temperature
T_g	gas temperature
T_j	jet temperature at inlet; jet temperature at pipe exit
T_s	surface temperature
T_w	wall temperature
T_∞	free stream temperature
T^+	dimensionless temperature
t	time; pipe wall thickness
TI	turbulence intensity; jet turbulence intensity at inlet
TL	dimensionless turbulence length scale
U	jet velocity at inlet; local velocity magnitude
U_b	bulk velocity of pipe flow
U_i	mean velocity component along the *i*th coordinate direction
u	velocity parallel to wall
u_i	velocity component along the *i*th coordinate direction
u_i'	fluctuating velocity component along the *i*th coordinate direction
u_τ	friction velocity
u^+	dimensionless velocity parallel to wall
V	characteristic velocity
$\overline{v_2}$	turbulence velocity scale in the V2F turbulence model
$\vec{v}$	velocity vector
w	representative in-cylinder flow velocity
w_s	spray width
x_i	*i*th Cartesian coordinate
y	normal distance to nearest wall
y^+	dimensionless normal distance to nearest wall
z	vertical distance from wall

Greek symbols

β	turbulence model constant; exponent in correction factor in Nusselt number correlation; coefficient of thermal expansion
γ	exponent in stagnation point Nusselt number correlation
$\Delta T_{aj}{}^*$	dimensionless temperature difference between jet temperature at inlet and ambient gas inflow temperature
δ	Kronecker unit tensor
δ_{ij}	Kronecker delta

δ_t	thermal boundary layer thickness
ε	dissipation rate of turbulent kinetic energy; emissivity
ε^+	dimensionless dissipation rate of turbulent kinetic energy
$\dot{\varepsilon}$	strain-rate tensor
η_0	turbulence model constant
κ	von Kármán constant
λ	thermal conductivity
μ	dynamic viscosity
μ_t	turbulent viscosity
ν	kinematic viscosity
ρ	density
σ	Stefan-Boltzmann's constant
$\sigma_{h,t}$	turbulent Prandtl number
σ_k	turbulent Prandtl number in turbulent kinetic energy equation
σ_{wf}	turbulent Prandtl number in temperature wall function
σ_ε	turbulent Prandtl number in equation for dissipation rate of turbulent kinetic energy
τ	viscous stress tensor
τ_{ij}	viscous stress tensor
τ_w	wall shear stress
τ_t	turbulence time scale
Φ	dissipation function
φ	sublayer resistance factor

Abbreviations

BDC	Bottom dead center
CAD	Crank angle degrees
CFD	Computational fluid dynamics
DNS	Direct numerical simulation
FVM	Finite volume method
LES	Large eddy simulation
RANS	Reynolds-averaged Navier-Stokes (equations)
RCM	Rapid compression machine
RNG	Renormalization group
RSM	Reynolds stress model
TDC	Top dead center

1 Introduction

The majority of the vessels in the world merchant fleet today use large two-stroke diesel engines as prime movers. These engines differ both in size and design from conventional automotive diesel engines. The power output of the large two-stroke marine diesel engines is in the magnitude from a few MW and up to about 90 MW. The largest of these engines have bores about 1 m and strokes exceeding 2.5 m, while the engine speed is about 80 - 90 rpm at full load conditions. An example of this type of engine is shown in Fig. 1.1. The figure shows a cross section of a 12 cylinder MAN Diesel & Turbo two-stroke marine diesel engine with a power output at full load of 69 MW. The bore is 98 cm, and the engine speed at full load is 94 rpm.

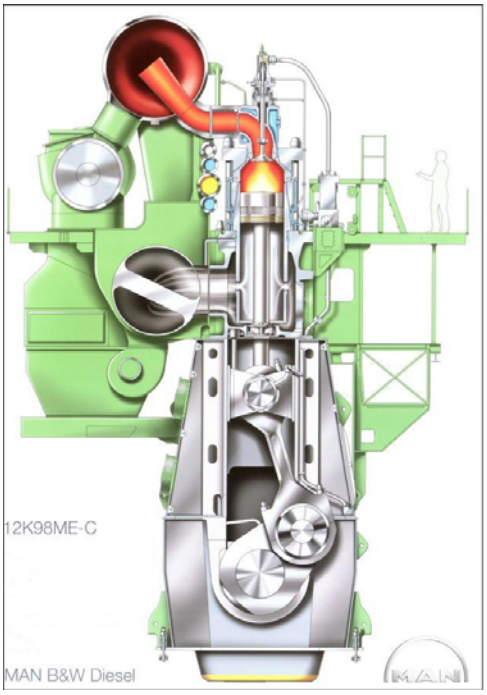

Fig. 1.1 Large two-stroke marine diesel engine.

A reason for the choice of large two-stroke diesel engines as prime movers in merchant vessels is their high efficiency. These engines are highly developed and are the most efficient internal combustion engines existing today with efficiencies about 50%, i.e. about half of the energy supplied to the engine in terms of fuel gets converted into mechanical work on the output shaft. Another beneficial feature of these engines is that they are able to run on very poor, and thus cheap, fuels. Typically a residual fuel oil is used, the so-called heavy fuel oil, which contains considerable more sulfur and impurities than conventional diesel oil.

Engine manufactures of large marine diesel engines are, similar to other engine manufactures, constantly working on improving the engines with respect to higher efficiency and lower emission level as well as higher specific power output. This is based on increasing demands from ship owners, which again are motivated by increasing fuel oil prices, stricter global and local emission legislations and general increasing merchant vessel sizes. The fuel oil price level has increased significantly during the last 10 years as indicated in Fig. 1.2, and a further increase is expected in the future. The figure illustrates the crude oil price development since 1987 in U.S. Dollars pr. barrel crude oil (Brent Crude).

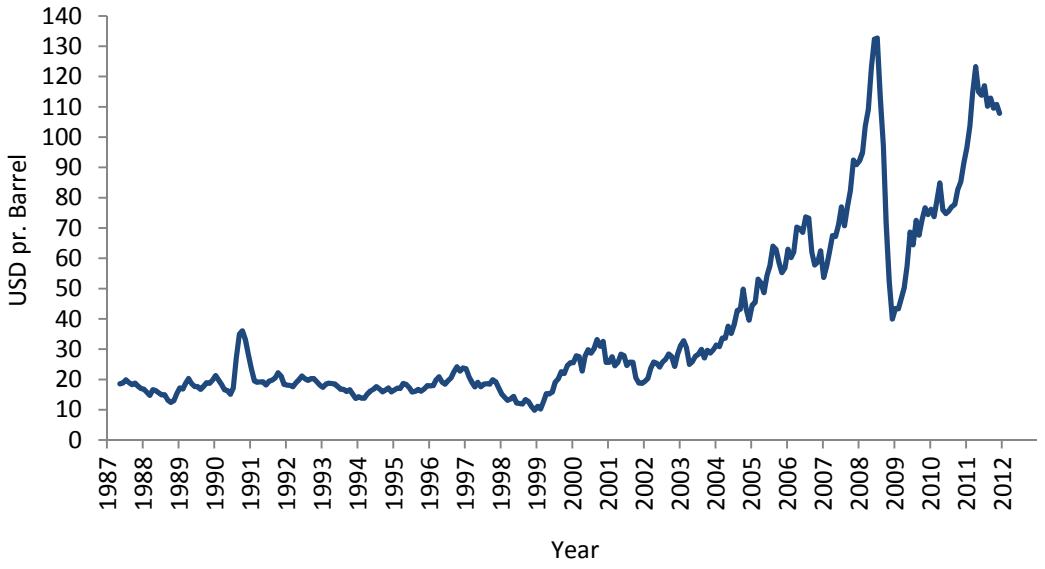

Fig. 1.2 Crude oil price development in the last 25 years (Brent Crude) based on data from the U.S. Energy Information Administration [1].

Currently, tightening of maritime emission limits is also taking place. This is illustrated in Fig. 1.3 and Fig. 1.4. Fig. 1.3 shows the maritime NO_x emission limits regulated by the International Maritime Organization (IMO). The Tier I limit entered into force in 2005 and applied retroactive to new engines installed on vessels after 2000. The Tier II limit applies to new engines installed after 2011, while Tier III is to enter into force in 2016. Tier I and Tier II are global limitations, whereas Tier III only applies to so-called local Emission Control Areas (ECA). The NO_x Emission Control Areas (NECA) include most of the coastal areas in the U.S. and Canada and parts of the Caribbean Sea [2]. Maritime SO_x emissions are indirectly regulated by limiting the sulfur content of the fuel oil. The sulfur content limits are presented in Fig. 1.4. The SO_x Emission Control Areas (SECA) include the Baltic Sea, the North Sea and most of the coastal areas in the U.S. and Canada, while parts of the Caribbean Sea will be included in 2014 [2]. Alternative methods for limiting the SO_x emissions, e.g. application of devices for exhaust gas cleaning, are allowed instead of complying with the fuel oil sulfur content limits. In the SECAs for instance, the SO_x emissions are then limited to 6 g/kWh [2].

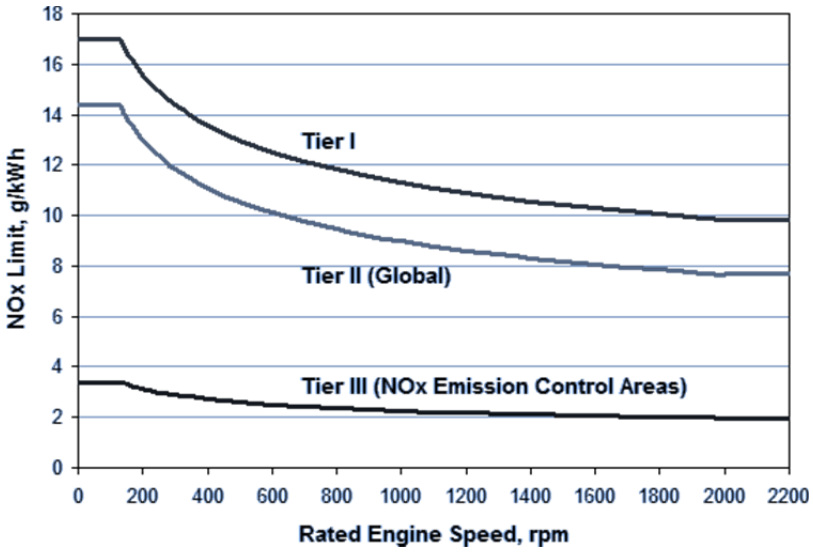

Fig. 1.3 Maritime NO_x emission limits regulated by the International Maritime Organization (IMO). Tier I applies to engines installed after 2000, while Tier II applies to engines installed after 2011. Tier III is to enter into force in 2016. The figure is reproduced from DieselNet [2].

The introduction of maritime emission limits for CO_2, particulates and unburned hydrocarbons may additionally be expected in the future [3] as well as an extension of the ECAs. Due to the mentioned different factors, continued research and development in large two-stroke marine diesel engines are of importance.

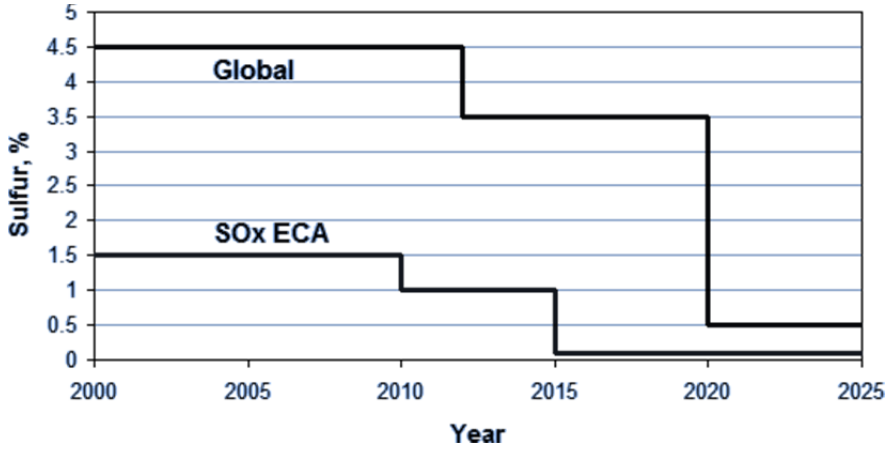

Fig. 1.4 Limits for the sulfur content of fuel oil (on a mass basis) regulated by the International Maritime Organization (IMO). The figure is reproduced from DieselNet [2].

1.1 Working principle of the two-stroke marine diesel engine

The working principle of the two-stroke marine diesel engine with uniflow scavenging is briefly described in the following by going through an engine cycle. Snapshots of the engine cycle are shown in Fig. 1.5.

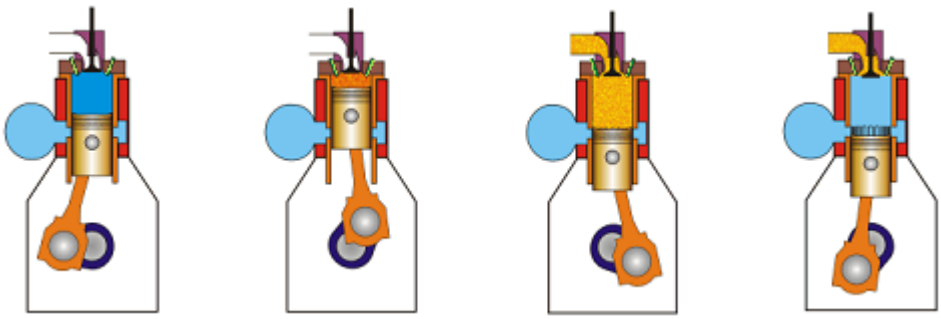

Fig. 1.5 Working principle of the two-stroke marine diesel engine. The figures are reproduced from Marinediesels.co.uk [4].

In the compression phase the piston moves upwards, and the fresh charge air trapped in the cylinder is compressed. At about the time when the piston is at the top position, i.e. top dead center (TDC), fuel is injected from fuel injectors located in the periphery of the cylinder cover (indicated by green bars in Fig. 1.5). Typically there are two or three fuel injectors pr. cylinder. The droplets in the atomized fuel spray evaporate quickly, and the fuel is ignited shortly after the piston has passed TDC due to the high gas temperature in the cylinder. Combustion occurs, while fuel continues to be injected, and the increasing cylinder pressure forces the piston down. At about 110 crank angle degrees (CAD) after TDC the exhaust valve in the top of the cylinder opens, and cylinder gas starts flowing out of the cylinder in the blow-down process. About 30 CAD after the opening of the exhaust valve the piston uncovers the scavenging ports. Fresh charge air enters the cylinder, and remaining combustion products and charge air are pushed out of the cylinder. This is termed the scavenging process. The scavenging continues, while the piston passes the lowest position, i.e. bottom dead center (BDC), and starts moving up again. The scavenging process is sufficiently long to allow fresh charge air to pass through the whole cylinder and out into the exhaust duct. This is done in order to minimize residual combustion products in the cylinder at the start of the next engine cycle. The exhaust valve typically first closes after the piston has completely covered the scavenging ports. When the exhaust valve has closed, the cylinder is again a closed chamber, and a new compression begins.

1.2 In-cylinder heat transfer in two-stroke marine diesel engines

Research and development areas in relation to large two-stroke diesel engines used as prime movers for ships are numerous. One research area is in-cylinder heat transfer, which is the overall topic of the present thesis. In-cylinder heat transfer refers to the heat transfer occurring in the engines between combustion chamber surfaces and the gas in the chamber. The combustion chamber is confined by the surfaces of the cylinder cover, liner, piston and exhaust valve spindle as indicated in Fig. 1.6. Cooling of the liner and cover is achieved by water cooling, whereas the piston is cooled by oil splashing in the interior of the piston. Cooling of the exhaust valve spindle is achieved when fresh charge air flows through the cylinder in the scavenging period of the engine cycle and passes the exhaust valve spindle. The fresh charge air also contributes to the cooling of the other combustion chamber surfaces.

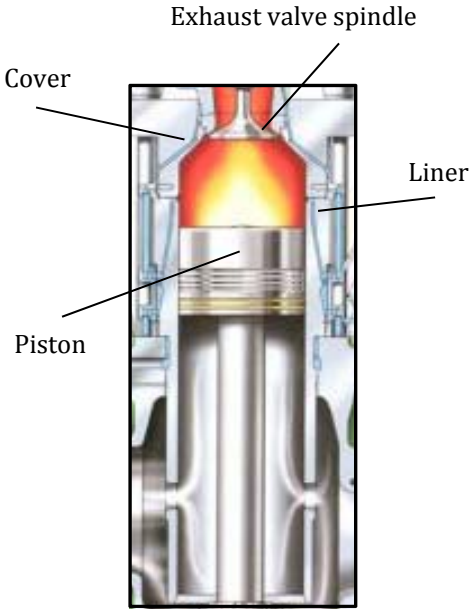

Fig. 1.6 Engine components confining the combustion chamber.

In-cylinder heat transfer is an important aspect in the design of two-stroke marine diesel engines as it affects important engine parameters. The influence on engine parameters is discussed in the following.

The in-cylinder heat transfer between cylinder gas and combustion chamber surfaces determines the total in-cylinder heat loss. The magnitude of the heat loss in turn affects the indicated efficiency of the engine, which expresses how much of the fuel energy input gets converted into mechanical work on the piston. A higher heat loss to the combustion chamber surfaces leaves less energy for conversion into mechanical work on the piston. The in-cylinder heat loss in two-stroke marine diesel engines amounts to 5-10% of the fuel energy input [5], [6]. This is relatively low compared to smaller automotive engines,

where the heat loss is typically about 25-30% of the fuel energy input [7]. A reason for the lower relative heat loss in large marine diesel engines is that these engines have a so-called quiescent type combustion chamber geometry without significant squish[1] zones, whereas smaller high speed automotive diesel engines usually have a bowl-in-piston type combustion chamber geometry [8]. Thereby the dominating squish influence on the flow field in automotive diesel engines near the time when the piston is at TDC, and consequently the increased heat transfer rates to the surfaces, are not present to the same extent in large two-stroke marine diesel engines. The two combustion chamber geometries are illustrated in Fig. 1.7.

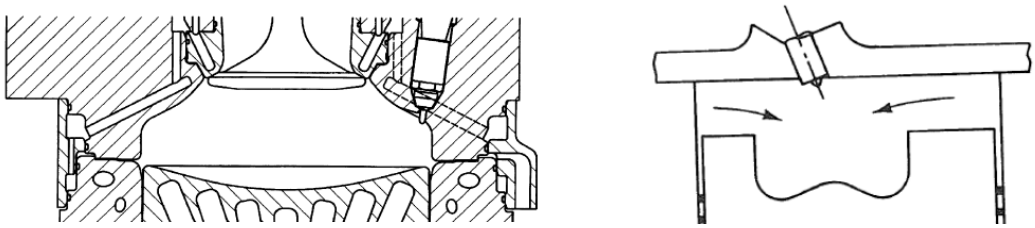

Fig. 1.7 Different combustion chamber geometries. Left: A quiescent type combustion chamber geometry of a large marine diesel engine. Right: A bowl-in-piston type combustion chamber geometry of an automotive diesel engine. The figures are reproduced from [9] (left) and [10] (right).

Another reason for the lower relative heat loss is that large marine diesel engines have a larger combustion chamber volume to surface area ratio compared to conventional automotive engines, which additionally contributes to reduce the relative in-cylinder heat loss [8]. The low relative heat loss in large marine diesel engines is a reason for their high efficiency. The effective or brake efficiency of these engines is, as mentioned earlier, about 50%, whereas the brake efficiency of automotive diesel engines is typically about 35% [11].

The in-cylinder heat transfer between cylinder gas and combustion chamber surfaces is also important due to the (indirect) effect on emission formation in the combustion chamber [12], [7]. The heat loss influences the temperature magnitude and distribution in the engine combustion chamber, and the temperature in turn affects the rate of the chemical reactions taking place and hence the formation of emissions. For instance the formation of NO_x is highly temperature sensitive, and higher gas temperatures would promote NO_x formation. On the other hand, a decrease in gas temperature is likely to result in increasing soot emissions as lower gas temperatures would limit the in-cylinder oxidation of soot formed under combustion.

Another important parameter, which is a direct result of the in-cylinder heat transfer between cylinder gas and combustion chamber surfaces, is the thermal load experienced on the chamber surfaces. High variation in the surface heat flux with time and location leads to uneven and time varying surface temperature distributions. Especially

[1] Squish is the radially inward or transverse gas motion occurring in an engine combustion chamber, when a portion of the piston surface approaches closely the cylinder head in the end of the compression stroke.

impingement of hot combustion products on the surfaces causes high surface heat fluxes. Too high surface temperature variations can be critical for the combustion chamber components, as it can lead to excessive thermal stresses, which may cause structural failure in terms of fatigue cracking [10]. Too high surface temperatures can also reduce the strength of the chamber components, which may be critical as well. The surface temperature of the cylinder liner is also important for the lubricating oil film on the liner. The oil properties deteriorate at too high temperatures, which can cause increased friction between piston rings and liner [10].

Better knowledge about the in-cylinder heat transfer is thus valuable for engine manufactures of large two-stroke marine diesel engines due to the above mentioned reasons. With a better estimation of the heat transfer magnitude, spatial distribution and variation over the engine cycle, predictions of other engine parameters can be improved, which may eventually lead to improved engine designs.

1.3 Thesis focus and motivation

The overall topic of the present thesis is in-cylinder heat transfer in large two-stroke diesel engines used as prime movers in ships, as mentioned above. The specific focus of the work is on heat transfer between the cylinder gas and the piston surface. The motivation for this focus is outlined in the following.

Knowledge about the in-cylinder heat transfer is important for several reasons as mentioned in the previous section. The main reason for the present work is based on the last point mentioned, i.e. the risk of piston damage as a consequence of the thermal load on the piston surface resulting from the in-cylinder heat transfer. The piston surface experiences a severe thermal load during the combustion phase of the engine cycle due to the close proximity of the combustion zone to the surface. Direct impingement of hot combustion products on the piston surface is likely to occur, and at the same time cooling of the piston crown[2] is relatively complicated. These conditions pose a challenge for the piston crown design and material selection, and typically chrome-molybdenum steel alloys are used, which are able to withstand high temperatures. Occurrence of holes or cracks in the piston crown resulting in contact between hot cylinder gas and cooling oil can be disastrous for the engine. Knowledge about heat transfer between piston surface and cylinder gas in two-stroke marine diesel engines is however limited, especially in terms of distribution and instantaneous magnitude. Better knowledge of the thermal load on the piston surface can lead to improved design of the piston crown, as it can help improving estimations of thermal boundary conditions used in structural calculations on the piston. An improved knowledge of the piston surface heat transfer may also be valuable for the estimation of other heat transfer contributions to the total in-cylinder heat transfer.

[2] The crown is the upper part of the piston, the lower part is termed the piston skirt.

1.4 Thesis objective

Based on the above mentioned motivation, the aim of the present study is to investigate the piston surface heat transfer in the event of impingement of hot combustion products on the piston surface and to provide an estimate of the potential peak piston surface heat flux, which is assumed to occur under this impingement process.

1.5 Procedure

The approach applied in the present work for studying the piston surface heat transfer in the event of impingement of hot combustion products is outlined and discussed below.

Information of the heat transfer to the piston can be obtained by means of experimental measurements or by numerical approaches. In this work the last method has been employed, i.e. a numerical approach using computational tools. This choice was based on different factors. Direct measurements on large two-stroke marine diesel engines are associated with relative high costs, as running tests on these engine are expensive both in terms of instrumentation, fuel and man power compared to tests on conventional automotive engines. Therefore manufactures of large marine diesel engines often have very tight schedules on their research engine facilities and more studies may be performed simultaneously. An additional complication is that equipment for surface heat transfer measurements to be used inside the engine should be able to withstand a very harsh environment in the engine during combustion with high pressures and temperatures and possibly corrosive deposits of e.g. sulfur oxides. Measurements could as well have been performed in an experimental setup simulating the impingement of hot combustion products on the piston surface during combustion. This approach was however planned to be employed in another study on the same subject and undertaken about the same time as the present study. This also made it interesting to apply a numerical method in the present work, so results of different approaches could be compared. This other study, however, later changed direction, and an experimental setup was not build. Another motivation for employing a numerical approach was that only limited numerical work appeared to have been performed on localized in-cylinder wall heat transfer in the event of impingement of hot combustion products on the combustion chamber surfaces.

Numerical approaches for estimating in-cylinder heat transfer in engines range from use of simple empirical correlation formulas to application of advanced computational fluid dynamic (CFD) modeling of the engine process. The relative simple correlation formulas for estimating in-cylinder engine heat transfer are typically based on dimensional analysis leading to correlations between the Nusselt, Reynolds and Prandtl numbers for expressing the heat transfer coefficient h in terms of engine parameters. Definitions of the Reynolds, Prandtl and Nusselt numbers are given in eqs. (1.1) - (1.3).

Reynolds number:

$$Re = \frac{\rho V L}{\mu} \tag{1.1}$$

Prandtl number:

$$Pr = \frac{c_p \mu}{\lambda} \tag{1.2}$$

Nusselt number:

$$Nu = \frac{hL}{\lambda} \tag{1.3}$$

V and L denote a characteristic velocity and length, respectively. ρ, μ, c_p and λ denote density, dynamic viscosity, specific heat capacity at constant pressure and thermal conductivity, respectively, and h is the heat transfer coefficient.

The first correlation for estimating engine heat transfer was proposed by Nusselt in 1923 [13] based on work on a spherical combustion bomb with combustion of a quiescent mixture of fuel and air. The formula of Nusselt was intended to predict time averaged heat transfer, but it has as well been applied in the prediction of instantaneous heat transfer [12]. Since then numerous correlations have been developed. The first correlation proposed for predicting instantaneous values of in-cylinder engine heat transfer is stated in the literature to be that of Eichelberg, proposed in 1939 [14]. A later correlation for instantaneous in-cylinder heat transfer estimation, which has been widely used, is that proposed by Annand in 1963 [15], who based his correlation on an extensive review of the correlations at that time. The perhaps the most widely used correlation for estimating the instantaneous in-cylinder heat transfer was developed by Woschni and proposed in 1967 [16]. Its popularity is probably due to its simplicity and still relative good prediction capability compared to other formulas. All the mentioned engine heat transfer correlations are however formulated for the prediction of the spatial averaged in-cylinder heat transfer. They are not intended for providing local instantaneous heat transfer estimates, which are of relevance in the present work. Correlations for the prediction of local instantaneous heat transfer have been proposed later by LeFevre et al. [17] and Dent and Sulaiman [18]. Their correlations are able to provide estimates of the local instantaneous heat flux on the piston or the cylinder head at a given radial distance from the bore axis. However, these correlations, as well as the others mentioned, are based on data from automotive engines, which have a different design than large marine engines. As the correlations are intended for the prediction of local heat flux values, it may thus be questionable how good predictions they can provide for other classes of engines. Two newer heat transfer correlations, which have been developed based on data for large low-speed two-stroke diesel engines, have been discussed and evaluated by Boulouchos and Brunner [19]. However, these correlations are not capable of providing local heat transfer values but only spatially averaged values. No empirical correlation formula seem to be available for the prediction of instantaneous local heat flux values in large marine diesel engines, which is in focus of the present work.

The empirical correlation type formulas mentioned above are often being used for estimation of the total instantaneous in-cylinder heat transfer, e.g. in 0-dimensional engine cycle models for prediction of overall engine performance parameters. Advanced multi-dimensional computational modeling tools as CFD are typically being used, when estimations of localized in-cylinder heat transfer values are required, because of the capability of providing far more detailed information than the empirical correlations. In the present work CFD has also been employed as the computational tool due to its potential to provide localized and detailed heat transfer information.

One approach to obtain the desired heat transfer information would be to perform CFD simulations of the full engine cycle using the real engine geometry and subsequently extract the localized heat transfer information. However, such a simulation is a quite complex task involving the application of several submodels to describe for instance piston movement, opening and closing of the exhaust valve, fuel injection with atomization and droplet evaporation, auto-ignition, chemical reactions during combustion, soot formation and oxidation, and thermal radiation. Additionally, turbulence modeling and especially near-wall treatment of the flow field are important for the heat transfer predictions. A problematic point in performing full engine cycle simulations is that there are many factors, which can influence the heat transfer results due to the many submodels involved. This complexity may cause difficulties in performing a validation of the heat transfer results and increase the risk of erroneous predictions, as the results will then depend on the quality of the many submodels. Therefore simulations of a more simple type were performed in the present work. These simulations focused on the process of impingement of hot combustion products on a surface under conditions approximating the conditions in the engine combustion chamber during combustion. Such simulations are considerably less complex than that of full engine cycle simulations and easier to validate. However, the task is then to impose representative conditions in the setup, so that the resulting thermal load on the surface during the impingement process corresponds to that experienced on the piston surface in the real engine.

The impingement process of hot combustion products on the piston surface can be simulated in different ways. A full or simplified combustion chamber geometry at the time of combustion could be simulated, i.e. a closed chamber with injection of liquid fuel, subsequent evaporation, ignition, combustion and wall impingement. Such a setup would still be complex in terms of the amount of submodels required. For instance fuel injection modeling, which is typically based on a Lagrangian description of the fuel droplets, has been reported to be rather difficult [20]. The modeling would include submodels for atomization, droplet beak-up, collision and coalescence apart from momentum, heat and mass transfer interaction with the surrounding fluid. Specially the modeling of the atomization process is still problematic and results in an inherent dependency of results on grid resolution [21]. This dependency is due to that the models assume a relative small volume occupied by liquid fuel compared to the volume of gas phase in the cells. Refining the mesh near the fuel injection orifice may violate this assumption, and

numerical difficulties can arise [22], [23]. An alternative approach might be to approximate the fuel spray with a gas jet. It has previously been reported that a gas jet injected with the same mass and momentum flow rate as a non-combusting diesel spray may reproduce the trends in penetration and dispersion angle of the spray well [24]. However, in the case of a combusting diesel spray the approximation by a combusting gas jet was reported to be less successful [23].

Due to the above mentioned problematic points and in order to keep the complexity and amount of influential submodels to a minimum while focusing on the impingement process, a different route for the numerical work was chosen. The heat transfer to the piston surface in the event of impingement of hot combustion products was investigated by simulating the impingement of a hot gas jet onto a surface under engine-like conditions. The gas jet represented the flow of hot combustion products impinging on the piston surface, and thereby the fuel injection and spray development did not need to be modeled, which significantly simplified the simulations. However, it is difficult to determine appropriate boundary conditions to impose in such simulations for parameters like velocity, temperature, turbulence and pressure, so that the jet impingement process will approximate the actual in-cylinder process. Hence, a reference case was established representing a best estimate of the actual in-cylinder conditions needed in the simulation. Subsequently, parameter variations were performed around the reference conditions in order to obtain a configuration space within which the actual impingement heat transfer situation would be represented. Observing the effect of the parameter variations on the surface heat transfer also provided information about the variation of the piston surface heat transfer with in-cylinder conditions.

The procedure followed in the work reported in this thesis can be summarized in main points as:

1. Define a jet impingement configuration that approximates the impingement of hot combustion products on the piston surface in large two-stroke marine diesel engines during the combustion phase of the engine cycle.

2. Model the defined jet impingement configuration using CFD software.

3. Perform simulations with the established model, and subsequently conduct an analysis of the results to study the piston surface heat transfer in the event of impingement of hot combustion products on the piston surface.

1.6 Structure of thesis

The thesis consists of nine chapters with each chapter divided into a number of sections. The contents of the chapters are outlined below.

The present chapter contains the introduction to the thesis topic and work.

The second chapter gives a more detailed overview of engine heat transfer and related theory. In this chapter previous studies and results relevant for the present work are presented and discussed.

In the third chapter, the jet impingement configuration considered in the present work is described. Differences between the impingement process in the considered configuration and the actual impingement process in the engine are also discussed.

The fourth chapter contains a description of the numerical modeling applied in the present work, i.e. an outlining of the governing equations and the applied numerical setup.

In the fifth chapter, a validation study of the numerical modeling is presented, where model results are compared to existing experimental jet impingement heat transfer data.

In the sixth chapter, the main results of the present work are presented and evaluated, i.e. the obtained heat transfer results from the performed simulations of the impingement process in the considered jet impingement configuration.

The seventh chapter contains a summary of the obtained results, and an estimation of the peak piston surface heat flux level is provided and discussed.

Conclusions of the performed work are provided in chapter eight, and some considerations and suggestions for further work related to the present study are given in chapter nine.

2 Previously obtained results

In-cylinder heat transfer studies of relevance for the present work are reviewed in this chapter in order to provide an overview of previously performed investigations and obtained in-cylinder heat flux magnitudes. Before reviewing and discussing the heat transfer results presented in the literature, it is of relevance first to introduce and comment on the different heat transfer modes occurring in internal combustion engines.

2.1 Heat transfer modes in engines

Heat transfer occurs in three different fundamental modes. The modes are conduction, convection (cumulative sum of conduction and advection due to bulk gas motion [25]) and thermal radiation. All of these modes of heat transfer are present in the case of engine heat transfer. This is illustrated in a simplified manner in figure Fig. 2.1, which depicts a part of an engine combustion chamber with associated heat transfer modes.

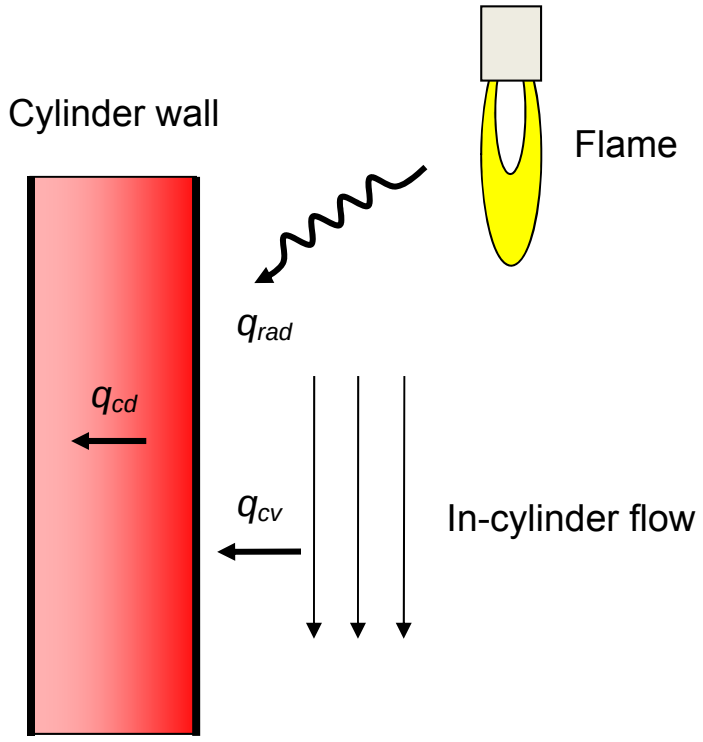

Fig. 2.1 Engine heat transfer mechanisms.

In-cylinder heat transfer consists of contributions from convection and thermal radiation as illustrated in Fig. 2.1 by the heat fluxes q_{cv} and q_{rad}, respectively. Heat conduction through the cylinder wall is illustrated by the heat flux q_{cd}. Convective heat transfer between gas and surfaces in the combustion chamber is the main contributor to the total

in-cylinder heat transfer. However, thermal radiation in diesel engines can constitute a significant part of the total in-cylinder heat transfer, whereas the relative heat transfer contribution from thermal radiation in gasoline engines is low. This is due to the formation of a large number of soot particles in the flame region in a diesel engine during combustion, as thermal radiation from soot particles is about five times that of gaseous combustion products [10].

2.1.1 Convection

Convective heat transfer between gas and surfaces in the combustion chamber is typically described by Newton's law of cooling:

$$q_{cv} = h\left(T_g - T_s\right) \tag{2.1}$$

q_{cv} denotes the convective heat flux to a surface [W/m^2], T_g is the gas temperature [K], T_s is the surface temperature [K], and h is the heat transfer coefficient [W/(m^{2}K)]. As mentioned in chapter 1, numerous empirical correlations have been developed to determine the heat transfer coefficient. The correlations are typically based on measured relationships between the Nusselt, Reynolds and Prandtl numbers defined in terms of in-cylinder parameters. As an example, a correlation that has been widely used is that of Woschni [16]. In the units given below it reads [10]:

$$h = 3.26\, B^{-0.2}\, p^{0.8}\, {T_g}^{-0.55}\, w^{0.8} \tag{2.2}$$

B denotes the cylinder bore [m], p the pressure [kPa], T_g the gas temperature [K], and w is a representative in-cylinder flow velocity [m/s]. The correlation provides instantaneous, but spatially averaged, values of the heat transfer coefficient h [W/(m^{2}K)], and hence the values of the parameters p, T_g and w are also given as instantaneous and spatially averaged values. It should be mentioned that eq. (2.2) is in fact stated to also take into account contributions from thermal radiation in a lumped form through appropriate formulation of w during combustion [16], [7].

2.1.2 Thermal radiation

Heat transfer contributions from thermal radiation can be described by equations based on the Stefan-Boltzmann law, which expresses that the emitted power by thermal radiation pr. unit surface area of a black body is directly proportional to the body's temperature to the fourth power. The radiation heat transfer rate $\dot{Q}_{1\to2}$ [W] between two grey and diffuse surfaces, which form an enclosure and have the areas A_1 and A_2 [m^2] and the temperatures T_1 and T_2 [K], is given by eq. (2.3) [25]:

$$\dot{Q}_{1\to2} = \frac{\sigma(T_1^4 - T_2^4)}{\frac{1-\varepsilon_1}{\varepsilon_1 A_1} + \frac{1}{A_1 F_{12}} + \frac{1-\varepsilon_2}{\varepsilon_2 A_2}} \tag{2.3}$$

$\sigma = 5.67 \cdot 10^{-8}$ W/(m^{2}K^4) is the Stefan-Boltzmann constant, ε_1 and ε_2 are the emissivities of the surfaces, and F_{12} is the view factor for surface 1 to surface 2. The soot covered surfaces in diesel engines have high emissivities, and the diesel flame itself, due to the presence of soot particles, has an emissivity close to one [11]. Cleaner surfaces and flames with few soot particles as found in gasoline engines have much lower emissivities. These conditions result in higher thermal radiation in diesel engines than observed in gasoline engines as mentioned earlier.

2.1.3 Conduction

Heat transfer by conduction occurs for instance in the combustion chamber walls as indicated in Fig. 2.1. Heat transfer by conduction is described by Fourier's law, where the heat flux vector $\vec{q}_{cd}$ is given by:

$$\vec{q}_{cd} = -\lambda \nabla T \tag{2.4}$$

λ is the thermal conductivity [W/(m K)]. The conductive heat flux [W/m^2] in direction i is thus given by:

$$q_{cd,i} = -\lambda \frac{\partial T}{\partial x_i} \tag{2.5}$$

Heat conduction in combustion chamber walls can often be treated as a steady state heat transfer case, because surface temperature oscillations usually only penetrate a few millimeters into the wall material [10]. The temperature gradient through a large part of the wall is thus practically stationary (for constant engine conditions).

After this brief description of heat transfer modes present in engine heat transfer, an overview of relevant magnitudes of in-cylinder engine heat transfer is given based on previous findings reported in the literature. As the focus is on in-cylinder heat transfer, only convective and radiation heat transfer magnitudes are considered.

2.2 General in-cylinder heat flux levels

Measurements of in-cylinder heat transfer in diesel engines have been performed intensively during the past five decades. Peak values of the in-cylinder heat flux on the combustion chamber surfaces have been stated to range from a few MW/m^2 [7] to about 10 MW/m^2 [12] for diesel engines. The variation of the instantaneous surface heat flux within the combustion chamber is significant. The heat flux can differ up to 5 MW/m^2 at

two locations that are only 1 cm apart as mentioned in [12]. This emphasizes the high influence of local instantaneous conditions on the local heat transfer. The highest heat flux levels are encountered primarily on the cylinder head and on the piston surface during the combustion phase due to the close proximity of these surfaces to the hot combustion products [10]. In contrast to this, peak heat flux levels on the cylinder liner are up to an order of magnitude lower than the peak levels on the piston and cylinder head. As noted previously, the contribution by thermal radiation to the total instantaneous heat transfer in diesel engines is important as opposed to the radiation contribution in gasoline engines. Peak values of the radiation contribution in diesel engines can constitute up to half of the total instantaneous heat flux as concluded in [12], whereas lower ratios between 0.2 and 0.3 are mentioned in [26].

2.3 Piston surface heat transfer investigations

Previous investigations on diesel engine in-cylinder heat transfer to the piston surface include that of Dent and Sulaiman [18]. They performed experimental investigations on a 3 cylinder direct injection four stroke diesel engine with a bore of 102 mm and measured instantaneous heat flux levels at the piston and cylinder head surfaces using thin film thermocouples. They also performed separate measurements of the thermal radiation contribution to the total heat transfer using a pyroelectric thermal detector. Instantaneous peak heat fluxes at the piston surface of about 3 – 4 MW/m^2 were observed by applying the thermocouples. However, these measurements were obtained at part load conditions (40% load) and higher values may be expected at full load conditions. Their measurements of the radiation heat transfer contribution showed peak values of the instantaneous radiation heat flux of about 10% of the total instantaneous heat flux, which is considered relatively low compared to other studies [12].

Later Kimura et al. [27] studied the heat transfer to the piston surface in a single cylinder experimental four stroke direct injection diesel engine with a bore of 85 mm for different combustion chamber specifications, swirl ratios and injection timings. Heat flux measurements were performed with thin film thermocouples and showed peak values on the piston of 2 – 4 MW/m^2.

Arcoumanis et al. [28] also performed heat flux measurements on the piston surface of a direct injection single cylinder research diesel engine with a fast response thermocouple for different swirl ratios. The research engine was based on a four-cylinder Ford York 2.5L DI diesel engine. They measured peak heat flux levels on the piston surface of about 2 MW/m^2 under firing conditions. Under motoring conditions[3] the heat flux level was an order of magnitude lower. Arcoumanis et al. also performed measurements of the thermal radiation contribution to the total instantaneous heat flux and reported peak values of the radiation contribution of 15% – 17% of the total instantaneous heat flux.

[3] Motoring condition refers to that the engine crankshaft is turned (motored) by external force, i.e. no combustion takes place inside the engine cylinder. Firing condition refers to that combustion takes place.

Ishii et al. [29] performed investigations on a single cylinder direct injection 85 mm bore diesel engine with the aim of observing the influence of soot deposits on the piston surface heat transfer. Piston surface heat flux measurements using thin film thermocouples were performed and showed peak heat flux levels of up to 4 MW/m^2 depending on location. After 270 minutes of engine operation at full load, the peak heat flux at the measurement locations most exposed to soot deposits was decreased to 1 – 2 MW/m^2.

The above mentioned measurements suggest that peak heat flux levels of up to about 4 MW/m^2 can be expected on the piston surface. However, the reported measurements were performed on four stroke automotive size diesel engines typically with bowl-in-piston type combustion chamber configurations. Hence, both in engine size, combustion chamber geometry and operating principle the engines differ from large two-stroke marine diesel engines, which are in focus in the present work. Therefore the heat flux levels mentioned may not be directly representative for levels in large marine diesel engines.

The difference in combustion chamber geometry is of relevance for the influence on the piston surface heat flux. As mentioned in section 1.2, a relative flat piston with low curvature is used in large marine diesel engines, whereas typically bowl-in-piston type pistons are used in automotive diesel engines (illustrated in Fig. 1.7). This is likely to result in higher squish motions in automotive diesel engine combustion chambers than in large marine diesel engine combustion chambers, and accordingly may enhance the convective heat transfer in the automotive diesel engines. Hence, the peak piston surface heat flux in large marine diesel engines may be lower than that reported for automotive diesel engines. On the other hand, an enhanced swirling flow field during combustion may be experienced in large two-stroke marine diesel engines. This is due to the inlet port geometry in the bottom of the cylinder liner of these engines, which promotes a highly swirling flow field in the cylinder during the scavenging process. The strength of the swirling motion during combustion is however subject to a significant uncertainty.

The pressure level in large marine diesel engines is usually also higher than in automotive diesel engines. Peak pressure levels during combustion in large two-stroke marine diesel engines can reach 160 bar, whereas peak pressures levels of about 80 bar are common in automotive diesel engines. Increasing the pressure in the combustion chamber may increase the wall heat flux level as indicated in the study by Li et al. [30]. They observed an increase in the wall heat flux level in the magnitude of 30% – 40%, when doubling the pressure from 28 bar to 56 bar at the end of the compression (but without changing the temperature) in a rapid compression machine (RCM) simulating the compression and combustion processes in a diesel engine.

2.4 Heat transfer studies in large two-stroke diesel engines

Reported in-cylinder heat transfer measurements in large two-stroke marine diesel engines are very limited in the literature in contrast to measurements in automotive diesel engines. This may be due to the fact that the research community in the field of large marine diesel engines is significantly smaller than in the field of automotive engines. The complexities and relative high costs associated with measurements in large two-stroke marine diesel engines, as mentioned in section 1.5, are probably also influential.

Boulouchos et al. [8] reported heat transfer measurements, which were performed on a large Sulzer two-stroke marine diesel engine, similar to the engine type considered in the present work. The Sulzer engine was turbocharged and had a bore of 560 mm and a stroke of 1400 mm. The peak cylinder pressure was reported to be 125 bar, the maximum speed was 150 rpm, and the maximum brake middle effective pressure (bmep) was 15.5 bar. Measurements with both thermocouples and an optical pyrometer were performed. The measurement equipment was located in the cylinder cover periphery in the hole in which the starting air valve is usually mounted as indicated in Fig. 2.2. Hence, no measurements of the heat transfer to the piston surface were reported.

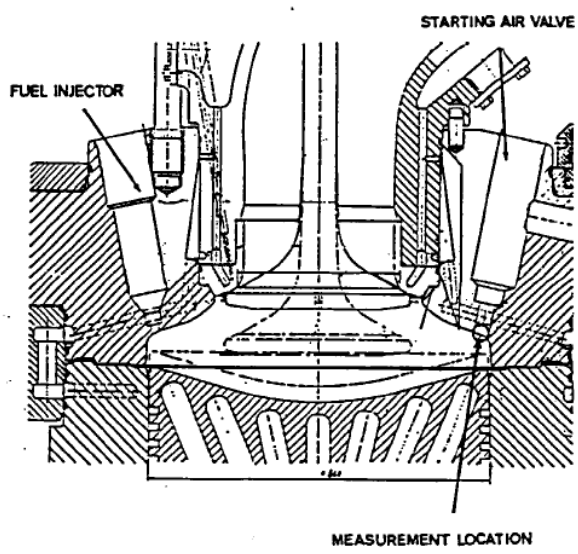

Fig. 2.2 Combustion chamber geometry and measurement location in the Sulzer two-stroke marine diesel engine in the investigation of Boulouhos et al. [8].

Based on their measurements, Boulouchos et al. reported peak heat flux levels at the combustion chamber surface in the magnitude of 1.2 MW/m^2. The surface heat flux values were calculated from thermocouple measurements of the wall temperature 0.2 mm below the surface. The measured wall temperatures 0.2 mm below the surface were reported to exhibit an oscillation over the engine cycle with an amplitude of 13K and peak temperatures about 302°C. Boulouchos et al. also estimated the thermal radiation contribution to the total instantaneous heat flux and obtained a peak value about

0.9 MW/m^2. However, the estimation of the radiation contribution was based on a calculated estimate of the convective heat transfer contribution, which was subtracted from the measured total instantaneous heat flux. The obtained value for the radiation contribution should therefore be considered as a rather uncertain estimate. The authors also pointed out that the actual radiation contribution was expected to be somewhat lower. The total peak heat flux of 1.2 MW/m^2 is seen to be lower than that reported for automotive engines, and this was also observed by the authors. The difference in peak heat flux level may be due to differences between the engine types, as mentioned earlier, but may also be due to the measurement location, as local conditions in the combustion chamber have a significant influence on the local heat flux level.

2.5 Diesel flame impingement heat transfer studies

Investigation of local in-cylinder peak surface heat fluxes in diesel engines has been performed by some researchers by directly studying diesel flame impingement heat transfer in an experimental setup simulating the combustion chamber environment in diesel engines during combustion. This approach is along the lines of that taken in the present work, and which was described in section 1.5.

Kamimoto et al. [31] studied the wall heat flux resulting from a diesel flame impinging normally and under an angle onto a flat surface. The investigation was performed using a rapid compression machine in which gas in a closed chamber was compressed by a fast moving piston. Liquid fuel was injected after the compression, and evaporation and autoignition occurred in the chamber. Thus the machine simulated the compression, fuel injection and combustion phase in a diesel engine. Kamimoto et al. measured surface heat flux levels with surface thermocouples for impingement angles between flame and surface of 90° and 45° and distances between fuel injector and impingement point of 28 mm and 40 mm. The fuel injector nozzle orifice diameter was 0.2 mm. The pressure and temperature in the chamber at the time of fuel injection were 30 bar and 522 ± 5 °C, respectively, while the wall temperature was 57 ± 10 °C. The radiation heat transfer contribution in the study was claimed to be negligible based on experimental and theoretical estimations. They observed peak heat flux values of about 7 MW/m^2 and noted that it was higher than typically observed in diesel engine studies. They argued that the difference in heat flux level might be caused by differences in spray and impingement characteristics, but also pointed out that the measured heat flux levels in diesel engines may be lower than the actual true level because of soot contamination of the thermocouple surfaces in the engines. Kamimoto et al. also reported that the measured surface heat flux level in their investigation was practically the same for an impingement angle of 90° and 45°.

Wolf and Cheng [32] also performed investigations of the resulting wall heat transfer from an impinging diesel flame in a rapid compression machine. The combustion chamber of the machine was cylindrical with a bore of 101.6 mm, and the fuel injection was normal to the cylindrical combustion chamber wall, which was equipped with

surface thermocouples. The distance between injector nozzle and wall varied between 29 mm and 105 mm, and the nozzle orifice diameter was 0.254 mm. The pressure in the combustion chamber at the time of fuel injection was about 38 bar, while the temperature was not reported. The initial wall temperature before compression was about 70°C. Peak surface heat flux values of about 4 MW/m^2 were observed. The heat flux level was observed to be relatively constant irrespective of the distance between nozzle and wall. A deflection of the flame impingement point of 10 mm was observed, when applying a swirl in the cylindrical chamber of 2500 rpm. The resulting heat flux level was however similar to the non-swirl cases. Wolf and Cheng estimated the radiation contribution to be about 20 – 30% of the measured total heat flux. They also argued that the relative constant heat flux that was measured, when varying the impingement distance, was due to the significant radiation contribution and small scale turbulence in the flame generated by the combustion. This was based on that a comparative non-combusting case, in which the air in the combustion chamber was replaced by nitrogen, showed a strong decrease in heat flux level when increasing the distance between nozzle and wall.

Another study of surface heat transfer resulting from an impinging diesel flame is that of Li et al. [30] who also performed investigations using a rapid compression machine to simulate the conditions in an automotive diesel engine. They applied thin film thermocouples to measure the surface heat flux resulting from impinging diesel flames and non-combusting impinging diesel sprays for various values of injection pressure, combustion chamber pressure and injector nozzle orifice diameter. The distance between nozzle and impingement point was 30 mm, the nozzle orifice diameter was 0.15 mm and 0.20 mm, and the impingement angle was 80°. Peak heat flux levels of 10 – 15 MW/m^2 were observed in the case of flame impingement. The pressure and temperature in the combustion chamber at the start of injection were 56 bar and 412°C, respectively, while the wall temperature was 150°C. The measured peak heat flux levels are considered to be relatively high compared to results of other studies. It may be due to differences in the chamber configurations, which can lead to differences in the flow fields. Another influential factor may also be the higher pressure level in the combustion chamber in the study of Li et al. However, Li et al. did not present a comparison of their results with the results of other investigators, and consequently possible causes for the higher heat flux levels were not discussed.

2.6 Numerical in-cylinder heat transfer studies

Numerical investigations of local in-cylinder heat transfer in diesel engines usually consist of full engine cycle CFD simulations or CFD simulations limited to the compression, combustion and expansion phase of the engine cycle. Local instantaneous heat transfer predictions are subsequently extracted from the simulation results. Determination of accurate peak surface heat flux levels is however difficult when applying standard wall functions in the turbulence modeling. Han and Reitz [33] pointed out that the usually applied temperature wall functions are not suitable for engine applications, as they are based on the assumption of constant density across the wall

boundary layer, which is not the case in engines during combustion due to large temperature gradients. As a consequence the local heat flux levels are underpredicted. Full resolution of the wall boundary layer is however not practically possible in engine cycle CFD simulations due to limited computational resources. Therefore Han and Reitz developed a temperature wall function valid for variable density boundary layers, which they applied in engine simulations. They obtained heat flux level predictions of up to 10 MW/m^2 at the cylinder head over the piston bowl in a Caterpillar heavy-duty truck diesel engine with a bore of 137.2 mm.

Nuutinen et al. [34] recently developed a similar temperature wall function formulation valid for variable density wall boundary layers, which they applied in simulations of large diesel engines. They claim that their temperature wall function is more rigorously formulated and provides better predictions than that of Han and Reitz [33], which they found to overpredict the wall heat flux level. Nuutinen et al. performed simulations of a large diesel engine, where they applied their developed wall function [35]. The engine was a four stroke medium speed Wärtsilä diesel engine with a bore of 200 mm and a rated power output pr. cylinder of 200 kW. They obtained peak heat fluxes on the piston surface of about 39 MW/m^2. This seems relatively high compared to previous experimental measurements as those mentioned in section 2.3 although they were performed on smaller diesel engines, and even more when the contribution from thermal radiation was not taken into account in the simulations. Unfortunately, Nuutinen et. al did not comment on the high heat flux level or provide much details about the simulation results, so the accuracy of the predicted peak heat flux level is difficult to assess.

Although the improved wall functions mentioned above consider density variations near the wall, they are still developed for flows parallel to the wall and may therefore be unable to provide accurate heat transfer predictions in the case of impingement of hot combustion products on the wall under high inclination angles, i.e. when the impingement is more or less normal to the wall.

Numerical work on heat transfer predictions in large two-stroke marine diesel engines using CFD has not been found in the literature, which seems consistent with the very sparse literature apparently existing on experimental heat transfer investigations for this class of engines.

2.7 Summary

Based on the above mentioned results on in-cylinder engine heat transfer in the literature, peak heat flux values in the magnitude of 1 – 10 MW/m^2 may be expected on the piston surface in large marine diesel engines and presumably in the lower end of this range. It is a wide range, but as local conditions are highly influential on the local heat flux level, it is difficult to deduce accurate heat flux estimates for large marine diesel engines from results based on studies primarily obtained in automotive diesel engines.

As in the case of automotive diesel engines, the heat transfer contribution from thermal radiation may also be expected to constitute a significant part of the total instantaneous heat transfer in large marine diesel engines, perhaps up to 50% at peak values.

The relative sparse literature on in-cylinder heat transfer in the field of large two-stroke marine diesel engines also encourages work in this area in order to provide further information on in-cylinder heat transfer for this class of engines.

3 Jet impingement configuration

Jet impingement heat transfer was investigated in the present work at conditions approximating the in-cylinder conditions in large two-stroke marine diesel engines during the combustion phase of the engine cycle. As described in chapter 1, the investigation was performed in order to obtain information about the piston surface heat transfer in the event of impingement of hot combustion products on the piston in this class of engines. The jet impingement configuration applied in the investigation is described below, and differences between the impingement process in the configuration and the actual process occurring in the engine during combustion are subsequently discussed.

3.1 Geometry and conditions

In the jet impingement configuration, a hot round turbulent gas jet of diameter *D* issued from a region at a distance *H* above a wall. The angle between the jet axis and the wall, i.e. the angle of inclination of the jet impingement, was 90°. The configuration is illustrated in Fig. 3.1 by the black lines.

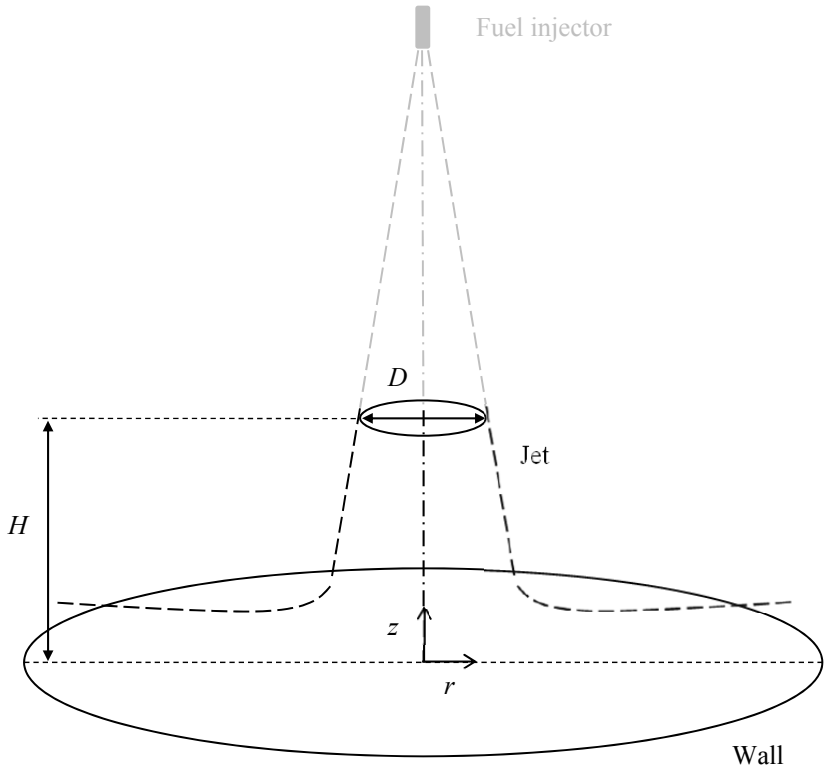

Fig. 3.1 Jet impingement configuration. *D* denotes the jet diameter at the distance *H* above the wall, *r* is the radial distance from the stagnation point, and *z* is the vertical distance from the wall.

The jet of diameter *D* issuing from the circular region was intended to represent a flow of hot combustion products approaching the piston surface, while the ambient gas represented the surrounding cylinder gas in the engine. The part of Fig. 3.1 in gray lines illustrates the imagined origin of the jet, i.e. a combusting fuel spray issuing as liquid fuel from an injector. This part was not modeled in the performed numerical investigation as mentioned in section 1.5. The region, from where the jet issues, is referred to as the jet inlet in the following.

Conditions and values for the geometrical parameters in the jet impingement configuration for a considered reference case are given in Table 3.1. Variations of some of the conditions have been performed in a parameter variation study, which is presented later. Both the jet gas and the ambient gas in the jet impingement configuration were air.

Jet impingement configuration – reference case	
Jet temperature at inlet	2000°C
Jet velocity at inlet	10 m/s
Jet diameter at inlet	0.05 m
Jet turbulence intensity at inlet	5%
Wall temperature	400°C
Pressure	180 bar
Ambient gas temperature	2000°C
Distance between inlet and wall	0.10 m

Table 3.1 Conditions and geometry for the jet impingement configuration in the reference case.

The background for the choice of the parameter values in Table 3.1 is given below. The values are based on dimensions and conditions during combustion in the combustion chamber of a large two-stroke marine diesel engine. The engine is the MAN Diesel & Turbo research engine, 4T50ME-X, with a bore of 500 mm.

3.1.1 Jet temperature at inlet

The jet in the configuration was intended to represent the combustion products approaching the piston surface in the engine. The jet temperature at the inlet was therefore chosen to approximate the temperature of the combustion products in the engine during combustion. This temperature was estimated to be about 2000°C [36].

3.1.2 Pressure

The pressure in the configuration represented the maximum pressure in the engine during the combustion process. The maximum pressure was estimated to be 180 bar [36], and hence this pressure was used in the reference case.

3.1.3 Wall temperature

The temperature of the wall was chosen to represent the piston surface temperature during combustion. Temperature measurements have been performed by MAN Diesel & Turbo in the piston crown of their research engine at approximately 5 mm below the piston surface [36]. The performed measurements provided information of the cycle mean temperature at the measurement location but not of the instantaneous values. The mean temperature was indicated to be in the order of 400°C at the measurement location. The piston surface temperature during combustion is probably higher than this value, but 400°C was assumed as a reference wall temperature in the jet impingement configuration based on these measurements.

3.1.4 Jet diameter at inlet and distance between inlet and wall

The diameter of the jet at the inlet and the distance between the inlet and the wall were based on fuel injector location relative to the piston in the engine at the time of injection, fuel spray direction and spreading of spray with distance from injector. The engine combustion chamber with the piston at TDC is shown Fig. 3.2 (fuel injection occurs at about the time when the piston is at TDC as mentioned in section 1.1). One fuel injector is shown with the direction of the fuel sprays indicated. The engine normally operates with either two or three injectors (with 180° and 120° between them, respectively), but only one injector is shown in Fig. 3.2 for better clarity. The exhaust valve is also not shown in the figure. The fuel injector has four nozzle holes and accordingly injects four sprays. The sprays are injected in different directions as indicated in Fig. 3.2. The two most downward directed sprays are likely to cause impingement of combustion products on the piston surface. Focusing on the most downward directed spray, a vertical cut was made through the combustion chamber along the spray direction in order to indicate a relevant distance for the choice of the inlet to wall distance in the jet impingement configuration. The vertical cut is shown in Fig. 3.3 with only the piston crown and fuel injector visible.

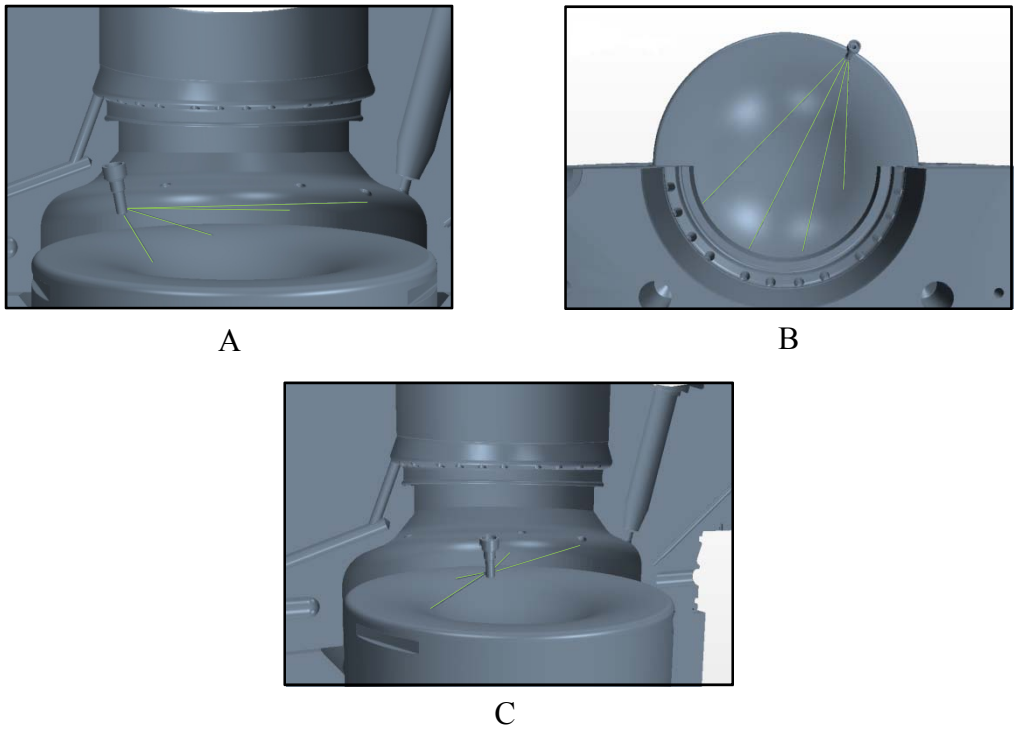

Fig. 3.2 Combustion chamber with piston at TDC. One fuel injector is shown with fuel spray directions indicated. Different views: A – Side view, B – Top view and C – Slightly inclined and turned side view.

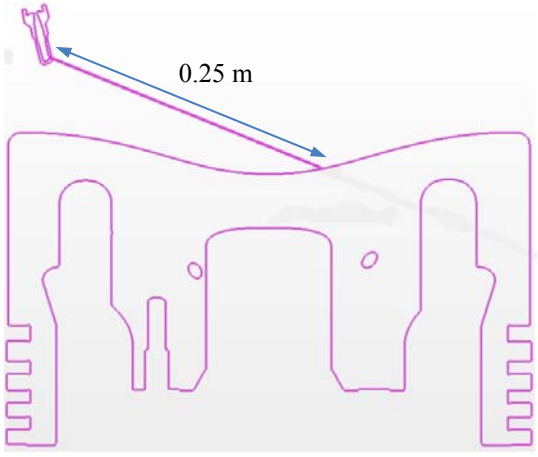

Fig. 3.3 Vertical cut through combustion chamber along spray direction. Only fuel injector and piston crown are shown.

Along the spray direction, the distance between the fuel injector and the piston surface is 0.25 m as indicated in Fig. 3.3. A distance of 0.10 m between the jet inlet and the wall in the jet impingement configuration was selected based on Fig 3.3, as a position along the spray direction 0.10 m from the piston surface was considered to be sufficiently far from the injector, so that the fuel droplets would have completely evaporated, and at the same time it was not too close to the piston surface. An estimation of the spreading of the fuel spray after injection was performed in order to determine an appropriate diameter of the jet at the inlet in the jet impingement configuration. The estimation was based on the work of Dam [37], who investigated fuel sprays in large two-stroke marine diesel engines. The work was however performed in an experimental setup with a quiescent atmosphere, atmospheric backpressure and without combustion. Measurements by Dam [37] of the spray width development of a fuel spray with distance from the fuel injector nozzle of a large marine diesel engine are shown in Fig. 3.4 in dimensionless form. The spray width and the distance from the nozzle are denoted by w_s and L, respectively, while d_0 is the nozzle hole diameter. The spray width increases approximately linearly with distance from the nozzle, but with a slightly different slope observed in the region close to the nozzle ($L/d_0 < \sim 16$) than further away from the nozzle. A linear fit to the spray width measurements was created in the region away from the nozzle.

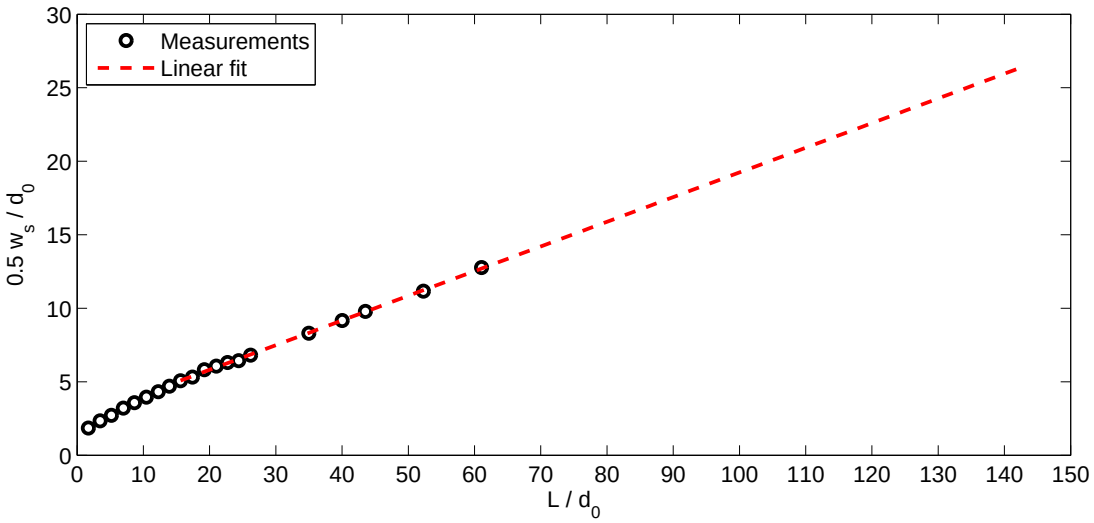

Fig. 3.4 Measurements of spray width w_s at different distances L from fuel injector nozzle in experiments by Dam [37] presented in dimensionless form. d_0 denotes nozzle hole diameter.

The linear fit was subsequently extrapolated to a dimensionless distance corresponding to a distance of 0.15 m from the fuel injector, i.e. 0.10 m from the piston surface in Fig. 3.3, in order to indicate a potential width at that distance. With a nozzle hole diameter of 1.05 mm as in the fuel injectors in the considered marine diesel engine, the dimensionless distance is 143. The width at that distance is in the order of 0.05 m according to Fig. 3.4. The fuel spray will however be ignited before it has traveled a distance of 0.15 m from the injector in the engine combustion chamber, but it was assumed that 0.05 m may also provide a representative value for the effective width of the resulting jet of combusting

gas and combustion products. A diameter of 0.05 m was therefore chosen for the jet diameter at the inlet in the jet impingement configuration.

The actual development of the width of the spray and the resulting jet of combusting gas and combustion products is likely to differ from that predicted from Fig. 3.4 due to different factors. The extrapolation in Fig. 3.4 of the tendency in the spray width development may be questionable as it is uncertain how far the linear tendency continues beyond the measurements. Another factor is the swirling motion of the ambient gas in the engine combustion chamber, which is likely to deflect the spray and thus change the spray route and the subsequent flow pattern and effective width of the jet of combustion products. The strength of the swirling motion at the time of fuel injection is however uncertain, and information about the actual flow field during the combustion phase in these engines is in general sparse. For simplicity, the effect of swirl was not included in the considered jet impingent case, but it would be of interest to investigate it in more advanced impingement cases. The actual spray and the resulting jet of combustion products also interact with the other sprays and jets of combustion products in the combustion chamber. This is likely to change the flow pattern of the individual sprays and flows of combustion products as well. Predictions based on the measurements by Dam probably also need to be modified in order to be valid for the actual spray development process in the engine, where there are combustion and a higher pressure level than in the experiments, in which the measurements were obtained.

Despite the above mentioned factors, a case with the chosen value for the jet diameter at the inlet at the selected distance from the wall in the jet impingement configuration was however considered to represent a potential impingent case in the engine, which could serve as a reference case for the heat transfer investigation in this work.

3.1.5 Jet velocity at inlet

The choice of jet velocity at the inlet was based on the work by Dam [37]. Dam reported measurements of the velocity decay of a fuel spray with distance from the fuel injector of a large marine diesel engine. The measured velocities were the velocity of the positive and negative spray border, respectively. The positive and negative spray borders are defined in Fig. 3.5 according to Dam [37].

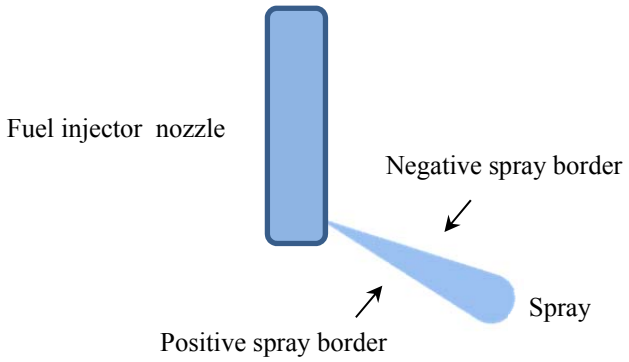

Fig. 3.5 Definition of positive and negative spray border.

The obtained velocity measurements are shown in Fig. 3.6. The velocity of the negative spray border is seen to decrease continuously in a linear manner with increasing distance from the nozzle. The velocity of the positive spray border also decreases in an approximately linear manner, but with an intermediate increase some distance from the nozzle. A linear fit to the spray border velocities was generated in the region after the intermediate acceleration of the positive border as indicated in Fig. 3.6. The linear fit was extrapolated to a distance of 0.15 m from the nozzle in order to indicate a possible velocity magnitude at that distance, corresponding to 0.10 m from the piston surface in Fig. 3.3.

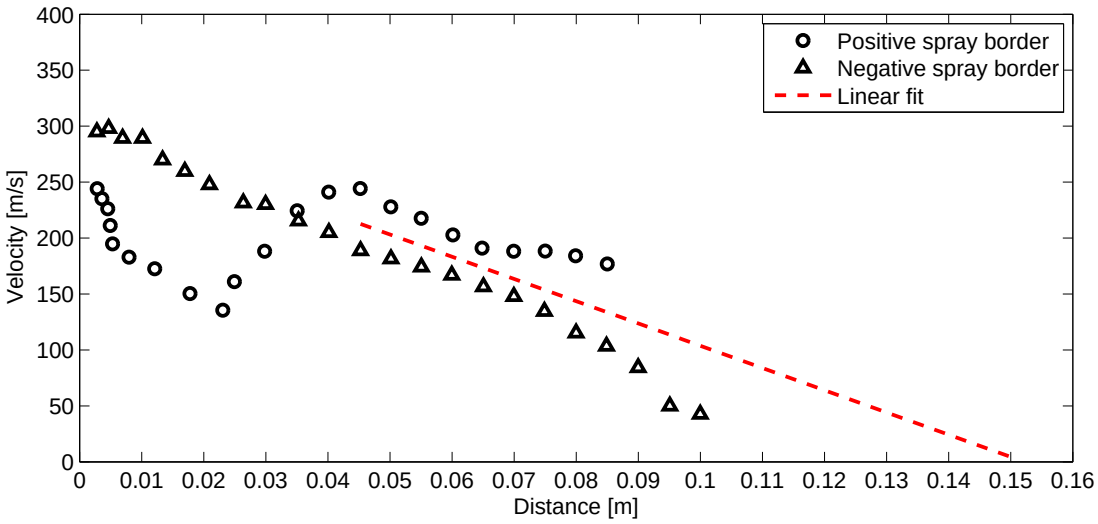

Fig. 3.6 Measurements of spray border velocity at different distances from fuel injector nozzle in experiments by Dam [37].

It was estimated that the velocity at a distance of 0.15 m from the injector nozzle could be in the order of 10 m/s, and this value was subsequently used for the jet velocity at the

inlet in the jet impingement configuration. It was however considered to be a rather rough estimate of a representative velocity for the actual process in the engine, as the measurements by Dam were performed in a quiescent atmosphere at atmospheric pressure without swirl and influence of other flows or combustion as mentioned earlier. The performed extrapolation, indicated in Fig. 3.6, may also be questionable as it is uncertain how the velocity decay will develop beyond the measurements. Therefore, a variation of the jet velocity at the inlet in the jet impingement configuration should be performed in order to study the influence of this parameter on the wall heat transfer.

3.1.6 Ambient gas temperature

The temperature of the ambient gas in the engine combustion chamber during combustion, i.e. the temperature of the gas outside the zones where combustion products are present, will be between the temperature of the combustion products and the compression temperature, which is the temperature of the cylinder gas at the end of the compression when the piston is at TDC and before combustion. For the considered marine diesel engine, a lower limit for the compression temperature was estimated to be about 600°C. Hence, the ambient gas temperature may be between 600°C and 2000°C during combustion and likely in the upper end of this interval, but the actual value is difficult to estimate. It was expected that it would be easier to obtain convergence in the numerical computations if the temperature of the ambient gas equaled that of the jet at the inlet. A temperature of 2000°C was therefore selected for the ambient gas in the jet impingement reference case. A variation of this temperature was performed later in order to observe the influence of the ambient gas temperature on the wall heat transfer.

3.1.7 Jet turbulence intensity at inlet

The turbulence intensity *TI* of the jet at the inlet was set to 5% in the jet impingement reference case. The turbulence intensity is given by eq. (3.1), where u_i' and U_i denote the fluctuating and mean velocity component, respectively, along the *i*th coordinate direction. Repeated subscripts denote summation of the term over all values of the subscript, and the overbar denotes time averaged value.

$$TI = \frac{\sqrt{\frac{1}{3}(\overline{u_i' u_i'})}}{\sqrt{U_i U_i}} \tag{3.1}$$

The intensity in the reference case was based on measured intensities at the pipe exit in jet impingement flows, where the jet emerged from a long pipe. The reported intensities were in the range from almost 0% to 5%, [38], [39] and [40]. The actual turbulence intensity in the gas of combustion products in the engine during combustion is not known, but might be somewhat higher than 5%. In flame impingement studies, values as high as between 20% and 30% have been reported [41]. A variation of the turbulence

intensity was therefore performed in order to observe the influence on the wall heat transfer.

3.1.8 General remark on the reference conditions and geometry

The jet impingement configuration with the above mentioned reference conditions and geometry is a relatively coarse approximation to the actual situation in the engine during combustion. The conditions in the combustion chamber during combustion are not well known in detail, and therefore there is quite some uncertainty on the estimated values used in the reference case. The applied values should thus only be seen as estimates of magnitudes representative for the impingement process in the engine and not as accurate or definitive values. A parameter variation study was therefore performed, where some of the parameter values in Table 3.1 were varied, and the influence on the resulting wall heat transfer was observed.

3.2 Jet impingement process versus actual process in engine

The jet impingement process in the configuration described above was aimed at approximating an actual impingement process of combustion products on the piston surface in the considered large marine diesel engine. However, a number of differences exist between the investigated impingement process and the actual process in the engine. These are mentioned and discussed below.

The main differences between the jet impingement process in the considered configuration and the actual process in the engine are:

- No combustion reactions take place in the jet impingement configuration
- Jet impingement is normal to the wall
- No cross flow is present in the jet impingement configuration
- Jet gas and ambient gas are air
- No soot deposits on the wall
- Jet cross-sectional shape is round
- Jet velocity is constant across the inlet and uniform in direction

The differences and their consequences are discussed in the following.

3.2.1 Combustion reactions

Combustion was not included in the jet impingement configuration due to simplicity and in order to establish a basic reference configuration. The effect of combustion may be localized points of heat release in the jet and an enhanced turbulence level as discussed by Wolf and Cheng [32]. This could cause an increased heat transfer to the wall, as a higher jet temperature and an increased turbulence level would be present closer to the wall.

3.2.2 Jet impingement normal to wall

The angle of inclination for the jet impingement was 90° in the considered configuration. In the actual impingement process in the engine, the angle of inclination is likely to be less than 90° as indicated in Fig. 3.2 and Fig. 3.3, but the effective angle is uncertain due to the complex conditions in the combustion chamber during combustion. An angle of 90° was therefore chosen as a reference case. The effects of a lower jet inclination angle on the wall heat transfer are a reduction in the magnitude of the maximum wall heat flux and a relocation of the position, where it occurs, as reported by Sparrow and Lovell [42] and mentioned by Martin [43] and Viskanta [44].

3.2.3 Cross flow

A cross flow may be used to simulate a swirling flow field in the engine during combustion, so the influence of swirl on the wall heat transfer can be studied. Cross flow was however omitted in the jet impingement configuration in order to simplify the configuration. The effect of cross flow is likely to reduce the local wall heat transfer as the jet to some degree would be deflected and consequently impinge on the wall at an angle less than 90°.

3.2.4 Use of air as jet gas and ambient gas

Both the jet gas and the ambient gas in the jet impingement configuration were air for simplicity. The gas in the impingement process in the engine during combustion is likely to be a mixture of combustion products and entrained charge air, but although the gas is not pure air, the main constituent of the mixture is however considered to be nitrogen, partly from entrained air and partly from unreacted nitrogen in the combustion products. The effect of having pure air as gas in the jet impingement configuration instead of a mixture of air and combustion products is therefore considered to be small with respect to the thermophysical properties of the gas. The effect on heat transfer by thermal radiation may however be significant as soot particles are the main source of thermal radiation in diesel engines. As noted earlier, the radiation from soot particles is about five times the radiation from the gaseous combustion products [10]. The most contributing gaseous species to thermal radiation are CO, CO_2 and H_2O, which were also not present in the jet

impingement configuration. As mentioned in chapter 2, thermal radiation has been stated to constitute up to about 50% of the instantaneous heat flux in diesel engines [12]. Hence, omitting soot particles and other combustion products reduces the thermal radiation and thereby the wall heat transfer.

3.2.5 Soot deposits

No soot deposits were present on the wall in the jet impingement configuration, whereas soot deposits on the piston surface in diesel engines during combustion are likely to exist. The soot acts as an isolating layer, and the consequence of not having soot deposits on the wall is likely to be a higher wall heat flux than if a soot layer was present. This was also indicated by measurement performed by Ishii et al. [29] and by Woschni and Huber [45] in diesel engines.

3.2.6 Jet shape

The jet in the impingement configuration was a round jet in order to simplify the configuration. The cross-sectional shape of the impinging combustion products in the engine is assumingly not round due to interaction with other flows in the combustion chamber. The effect on the wall heat transfer of a different jet shape than the actual cross-sectional shape of the impinging combustion products in the engine was not investigated. It was however believed that the impingement process in the considered jet impingement configuration would still provide heat transfer information relevant for the engine case, especially in the stagnation region, where the wall heat transfer was assumed to be less influenced by the jet shape.

3.2.7 Jet velocity

The jet velocity at the inlet in the jet impingement configuration was constant across the inlet and uniform in direction. In the actual process in the engine, the cross-sectional velocity profile of the impinging combustion products is however presumably non-constant. Although the profile may influence the resulting wall heat transfer, a profile of constant velocity was chosen as a first case for simplicity. The value applied for the velocity was based on measured spray border velocities as mentioned in section 3.1.5. The value can therefore be considered as a lower estimate of the real cross-sectional average velocity of the impinging combustion products as that would likely be higher than the velocity of the borders.

3.2.8 Summary

Based on the above discussion, it is obvious that there are some differences between the impingement process in the considered jet impingement configuration and the actual

impingement process in the engine, and that the differences are likely to influence the wall heat transfer to some extent. However, as mentioned previously, the jet impingement configuration was established in order to make a first simple case to investigate with as less complexity as possible.

4 Numerical modeling

This chapter contains an overview of the governing equations which form the basis for the numerical modeling of the jet impingement process described in chapter 3. The numerical modeling was performed in the CFD software package STAR-CD version 4.14. The STAR-CD code is based on the finite volume method (FVM), which is described in e.g. [46] and [47]. The numerical setup applied in the modeling is also described in this chapter. The numerical setup includes geometry and mesh, imposed boundary conditions, applied turbulence model, evaluation of thermophysical properties and density as well as the discretization scheme used, applied solution algorithm and convergence criteria.

4.1 Governing equations

The governing equations are the continuity, Navier-Stokes and energy equations. Due to the presence of a turbulent flow field in the considered jet impingement configuration and that direct numerical simulation (DNS) was computational too expensive in the scope of the present work, turbulence models were applied in the numerical modeling. Therefore, equations describing the applied turbulence models are additionally presented below. The governing and turbulence model equations are presented in Cartesian coordinate form as the applied CFD code solves the equations in this form. They are formulated using the Einstein notation, i.e. repeated subscripts denote summation. A general form of the governing equations is given first. The turbulence modeling is then discussed, which leads to some modifications of the equations. A set of governing equations with the modifications incorporated are then presented, which is the equation set solved by the applied code. Afterwards, equations constituting the turbulence models are presented.

The continuity equation is:

$$\frac{\partial \rho}{\partial t} + \frac{\partial \left(\rho u_j\right)}{\partial x_j} = 0 \tag{4.1}$$

ρ denotes density, t denotes time and u_j is the velocity component along the jth coordinate (x_j) direction.

The Navier-Stokes equations are given by:

$$\rho\left(\frac{\partial u_i}{\partial t} + u_j \frac{\partial u_i}{\partial x_j}\right) = -\frac{\partial p}{\partial x_i} + \frac{\partial}{\partial x_j}\left(\tau_{ij}\right) \tag{4.2}$$

where

$$\tau_{ij} = 2\mu S_{ij} - \frac{2}{3}\mu \frac{\partial u_k}{\partial x_k}\delta_{ij} \tag{4.3}$$

$$S_{ij} = \frac{1}{2}\left(\frac{\partial u_i}{\partial x_j} + \frac{\partial u_j}{\partial x_i}\right) \tag{4.4}$$

p denotes pressure, τ_{ij} is the viscous stress tensor and S_{ij} is the strain-rate tensor, μ denotes dynamic viscosity and δ_{ij} is the Kronecker delta, i.e. $\delta_{ij} = 1$ for i = j, and $\delta_{ij} = 0$ for i ≠ j. As indicated in eq. (4.2), buoyancy forces were not included. Calculations with buoyancy forces included in the flow computations have been performed, but showed negligible influence of buoyancy effects on the wall heat transfer due to high fluid momentum in the flow.

The energy equation is:

$$\rho\left(\frac{\partial h}{\partial t} + u_j \frac{\partial h}{\partial x_j}\right) = \frac{\partial}{\partial x_j}\left(-q_{cd,j}\right) + \frac{\partial p}{\partial t} + u_j \frac{\partial p}{\partial x_j} + \tau_{ij}\frac{\partial u_i}{\partial x_j} \tag{4.5}$$

where

$$q_{cd,j} = -\lambda \frac{\partial T}{\partial x_j} \tag{4.6}$$

h denotes enthalpy, and $q_{cd,j}$ is the diffusional (or conductive) heat flux in the jth coordinate direction given by Fourier's law as presented earlier in eq. (2.5). λ is the thermal conductivity, and T denotes temperature. Conversion between enthalpy h and temperature T is performed in the applied CFD code according to $h = \overline{c_p}T$, where $\overline{c_p}$ is the mean specific heat capacity at constant pressure, defined as:

$$\overline{c_p} = \frac{1}{T}\int_0^T c_p \, dT \tag{4.7}$$

As noted above, the jet flow in the considered jet impingement configuration is turbulent, and a turbulence model was therefore applied in the numerical simulations. However, jet impingement configurations have been stated to be a demanding class of cases to handle for turbulence models and have therefore been viewed as test cases for benchmarking of turbulence models [48], [49], [50]. As mentioned in [50] and [49], the difficulties for the turbulence models are caused by:

- A large acceleration of the flow after impingement followed by a deceleration.
- The existence of a laminar-turbulent transition in the wall jet.
- Entrainment of fluid into the jet from the surroundings.
- A relaminarization near the stagnation point.
- High streamline curvature.

The difficulties of modeling turbulent impinging jets have been recognized by the European Research Community on Flow, Turbulence and Combustion (ERCOFTAC), which has selected the case of an air jet impinging orthogonally onto a flat surface as a test case for turbulence models. ERCOFTAC has therefore posted flow and heat transfer measurements for such a case in their database to be used by modelers [51]. These and other data were used for validation of the numerical results of the present work. The validation study is presented in chapter 5. The decision of which turbulence model to use in the numerical simulations was based on two criteria:

- The model should be capable of providing accurate near-wall turbulence predictions in jet impingement configurations in order to obtain correct wall heat transfer results.
- The model should be computationally relatively cheap to use in order to save computation time, and so it could also be relevant in an industrial context.

The V2F turbulence model [52] was selected, which is a Reynolds-averaged Navier-Stokes (RANS) equations type eddy viscosity turbulence model. Thus, it is computationally cheaper than more advanced RANS type models such as Reynolds stress models (RSM) and other more demanding modeling approaches like large eddy simulation (LES) models. A RANS type model was also considered to be sufficient as heat flux fluctuations due to turbulent fluctuations in the flow were not important to resolve. The V2F model has been shown to be one of the most successful RANS type turbulence models for jet impingement heat transfer calculations, also in the stagnation point where other RANS type models are known to fail [53], [48], [50], [54]. The V2F model offers a good balance between prediction accuracy and computational cost and has been recommended as the preferred RANS type turbulence model for prediction of jet impingement heat transfer [53], [48]. It has also shown promising results for heat transfer predictions in more complex flows, e.g. [55], [56]. The V2F model does not apply wall functions and hence requires a very fine mesh near walls in order to fully resolve the wall boundary layer. Calculations with other RANS type eddy viscosity turbulence models were performed as well for comparison of their predictions with those of the V2F model. These models were a low Re k-ε model [57] and a k-ε RNG model (based on renormalization group theory) [58]. The k-ε RNG model employed wall functions to predict the velocity, temperature and turbulence distributions in the lower part of the wall

boundary layer. Hence, the needed number of cells near the wall was reduced and thereby the computation time.

The simulations were performed as steady state simulations because the focus was on the steady state wall heat transfer in the considered jet impingement configuration and not on the evolution in heat transfer until steady state conditions were reached. This was based on that the jet impingement configuration was considered as an approximation to a snapshot of the case where hot combustion products impinge on the piston surface in large marine diesel engines. Hence, the evolution in surface heat transfer during the impingement process was not addressed in this work.

The steady state Reynolds-averaged versions of the governing equations which were solved in the performed simulations are presented below in eqs. (4.8) - (4.13).

The continuity equation:

$$\frac{\partial(\rho u_j)}{\partial x_j} = 0 \tag{4.8}$$

The Navier-Stokes equations:

$$\rho\left(u_j \frac{\partial u_i}{\partial x_j}\right) = -\frac{\partial p}{\partial x_i} + \frac{\partial}{\partial x_j}(\tau_{ij}) \tag{4.9}$$

where

$$\tau_{ij} = 2\mu S_{ij} - \tfrac{2}{3}\mu \frac{\partial u_k}{\partial x_k}\delta_{ij} - \rho\overline{u_i' u_j'} \tag{4.10}$$

$$S_{ij} = \frac{1}{2}\left(\frac{\partial u_i}{\partial x_j} + \frac{\partial u_j}{\partial x_i}\right) \tag{4.11}$$

The energy equation:

$$\rho\left(u_j \frac{\partial h}{\partial x_j}\right) = \frac{\partial}{\partial x_j}(-q_{cd,j}) + u_j \frac{\partial p}{\partial x_j} + \tau_{ij}\frac{\partial u_i}{\partial x_j} \tag{4.12}$$

where

$$q_{cd,j} = -\lambda \frac{\partial T}{\partial x_j} + \rho \overline{u_j' h'} \tag{4.13}$$

The additional terms in eq. (4.10) and eq. (4.13) are the Reynolds stresses and the turbulent heat fluxes, respectively, which result from the Reynolds averaging of the Navier-Stokes and energy equations. The apostrophe denotes turbulent fluctuations, and the overbar denotes time averaged values of the fluctuation products. Variables without apostrophe represent time averaged values, while turbulent fluctuations in density, dynamic viscosity and thermal conductivity were not taken into account in the equations solved by the applied CFD code.

4.1.1 Turbulence modeling

As the turbulence models applied were eddy viscosity models, the Reynolds stresses and turbulent heat fluxes in eq. (4.10) and eq. (4.13), respectively, were modeled via the eddy viscosity concept. The Reynolds stresses were calculated as:

$$-\rho \overline{u_i' u_j'} = 2\mu_t S_{ij} - \frac{2}{3}\left(\mu_t \frac{\partial u_k}{\partial x_k} + \rho k\right)\delta_{ij} \tag{4.14}$$

In eq. (4.14), μ_t is the turbulent or eddy viscosity, which is modeled by the turbulence models, and k is the turbulent kinetic energy defined as:

$$k = \frac{1}{2}\overline{u_i' u_i'} \tag{4.15}$$

The turbulent kinetic energy is however not calculated directly from its definition in eq. (4.15) but is calculated via a transport equation for k in the turbulence models. The turbulent heat fluxes were calculated as:

$$\rho \overline{u_j' h'} = -\frac{\mu_t}{\sigma_{h,t}} \frac{\partial h}{\partial x_j} \tag{4.16}$$

$\sigma_{h,t}$ denotes a turbulent Prandtl number, and the value depends on the applied turbulence model. The models used in this work all treat $\sigma_{h,t}$ as a constant. The values for $\sigma_{h,t}$ are listed below in Table 4.1 to Table 4.3 together with the model constants of the different models.

The applied turbulence models are described in the following in terms of the model equations which constitute the models. As mentioned above, the models were a V2F turbulence model, a low Re k-ε model and a k-ε RNG model employing wall functions.

4.1.1.1 V2F turbulence model

The V2F turbulence model was proposed by Durbin [52]. It is can be considered as an extended version of a *k-ε* turbulence model and is given by the equations shown below [59]. The model constants are given in Table 4.1.

Turbulent kinetic energy equation:

$$\frac{\partial}{\partial x_j}\left[\rho u_j k - \left(\mu + \frac{\mu_t}{\sigma_k}\right)\frac{\partial k}{\partial x_j}\right] = \mu_t P - \rho\varepsilon - \frac{2}{3}\left(\mu_t \frac{\partial u_i}{\partial x_i} + \rho k\right)\frac{\partial u_i}{\partial x_i} \tag{4.17}$$

σ_k denotes a turbulent Prandtl number for the turbulent kinetic energy equation and is assumed constant, see Table 4.1. ε is the dissipation rate of turbulent kinetic energy, and P in the term accounting for the rate of production of k is given by eq. (4.18) with S_{ij} as defined in eq. (4.11).

$$P = 2S_{ij}\frac{\partial u_i}{\partial x_j} \tag{4.18}$$

Equation for the dissipation rate of turbulent kinetic energy:

$$\frac{\partial}{\partial x_j}\left[\rho u_j \varepsilon - \left(\mu + \frac{\mu_t}{\sigma_\varepsilon}\right)\frac{\partial \varepsilon}{\partial x_j}\right] = \frac{C_{\varepsilon_1}^z}{\tau_t}\left[\mu_t P - \frac{2}{3}\left(\mu_t \frac{\partial u_i}{\partial x_i} + \rho k\right)\frac{\partial u_i}{\partial x_i}\right] - \frac{C_{\varepsilon_2}}{\tau_t}\rho\varepsilon + C_{\varepsilon_3}\rho\varepsilon\frac{\partial u_i}{\partial x_i} \tag{4.19}$$

σ_ε denotes a turbulent Prandtl number for the equation for the dissipation rate of turbulent kinetic energy and is assumed constant, see Table 4.1. τ_t is a turbulence time scale and is presented later in eq. (4.25) and (4.26). C_{ε_2} and C_{ε_3} are constants, and $C_{\varepsilon_1}^z$ is given by eq. (4.20), where C_{ε_1} is a constant.

$$C_{\varepsilon_1}^z = C_{\varepsilon_1}\left(1 + 0.045\left(\frac{k}{\overline{v_2}}\right)^{1/2}\right) \tag{4.20}$$

The quantity $\overline{v_2}$ is given by the following transport equation:

$$\frac{\partial}{\partial x_j}\left[\rho u_j \overline{v_2} - \left(\mu + \frac{\mu_t}{\sigma_k}\right)\frac{\partial \overline{v_2}}{\partial x_j}\right] = \rho k f - 6\rho \overline{v_2}\frac{\varepsilon}{k} \tag{4.21}$$

$\overline{v_2}$ is a turbulence velocity scale, which can be interpreted as the mean square of velocity fluctuations normal to solid surfaces [49]. Far from solid surfaces $\overline{v_2}$ becomes proportional to k [49]. The term $\rho k f$ in eq. (4.21) accounts for the source of $\overline{v_2}$ [60], and f is given by:

$$L^2 \frac{\partial^2 f}{\partial x_j \partial x_j} - f = \frac{1 - C_1}{\tau_t}\left(\frac{2}{3} - \frac{\overline{v_2}}{k}\right) - C_2 \frac{\mu_t P}{\rho k} - 5\frac{\overline{v_2}/k}{\tau_t} \tag{4.22}$$

C_1 and C_2 are constants, and L is a turbulence length scale defined as [49]:

$$L = C_L \, max\left[L', C_\eta \left(\frac{\nu^3}{\varepsilon}\right)^{1/4}\right] \tag{4.23}$$

where

$$L' = min\left[\frac{k^{3/2}}{\varepsilon}, \frac{1}{\sqrt{3}}\frac{k^{3/2}}{\overline{v_2}}\frac{1}{C_\mu \sqrt{2 S_{ij} S_{ij}}}\right] \tag{4.24}$$

ν denotes kinematic viscosity, and C_L, C_η and C_μ are constants. When the length scale is based on the first expression in the square brackets in eq. (4.24), it is similar to the definition used in the standard k-ε turbulence model [61]. The second expression in the square brackets in eq. (4.24) represents an upper constraint on the length scale [48], [62], while the second expression in the square brackets in eq. (4.23) is a lower bound based on the Kolmogorov length scale. The turbulence time scale τ_t is defined as:

$$\tau_t = min\left[\tau_t', \frac{0.6}{\sqrt{3}}\frac{k}{\overline{v_2}}\frac{1}{C_\mu \sqrt{2 S_{ij} S_{ij}}}\right] \tag{4.25}$$

where

$$\tau_t' = max\left[\frac{k}{\varepsilon}, C_{KT}\left(\frac{\nu}{\varepsilon}\right)^{1/2}\right] \tag{4.26}$$

C_{KT} in eq. (4.26) is a constant. As in the definition of the turbulence length scale L, the last expression in the square brackets in eq. (4.25) represents an upper constraint on the

time scale [62], while the last expression in the square brackets in eq. (4.26) is a lower bound based on the Kolmogorov time scale.

The turbulent viscosity in the V2F turbulence model is given by:

$$\mu_t = \rho C_\mu \overline{v_2} \tau_t \tag{4.27}$$

The model constants in eqs. (4.17) - (4.27) are given in Table 4.1.

Model constants											
σ_k	σ_ε	$\sigma_{h,t}$	C_{ε_1}	C_{ε_2}	C_{ε_3}	C_1	C_2	C_L	C_η	C_μ	C_{KT}
1.0	1.3	0.9	1.4	1.9	-0.33	1.4	0.3	0.23	70.0	0.22	6

Table 4.1 Constants in the V2F turbulence model [59].

As the V2F turbulence model does not apply wall functions, a very fine mesh is required near walls in order to fully resolve the wall boundary layer, as mentioned earlier, and hence the y^+ value of the near-wall cells, i.e. the cells adjacent to the walls, should be of the order of 1 [59]. y^+ is a dimensionless wall distance and is defined as:

$$y^+ = \frac{u_\tau y}{\nu} \tag{4.28}$$

y is the normal distance to the nearest wall, ν is the kinematic viscosity, and u_τ is the friction velocity defined in eq. (4.29), where τ_w is the wall shear stress.

$$u_\tau = \left(\frac{\tau_w}{\rho}\right)^{1/2} \tag{4.29}$$

When using the V2F turbulence model, the wall heat flux is calculated according to eq. (4.13).

4.1.1.2 Low Re k-ε turbulence model

The low Re k-ε turbulence model applied in the present work was that of Lien et al. and is described in [57] and [59]. The model equations are given below, and the model constants are listed in Table 4.2.

Turbulent kinetic energy equation:

$$\frac{\partial}{\partial x_j}\left[\rho u_j k - \left(\mu + \frac{\mu_t}{\sigma_k}\right)\frac{\partial k}{\partial x_j}\right] = \mu_t P - \rho\varepsilon - \frac{2}{3}\left(\mu_t \frac{\partial u_i}{\partial x_i} + \rho k\right)\frac{\partial u_i}{\partial x_i} \tag{4.30}$$

The equation is the same as that applied in the V2F turbulence model. For explanation of variables, see therefore text below eq. (4.17).

Equation for the dissipation rate of turbulent kinetic energy:

$$\frac{\partial}{\partial x_j}\left[\rho u_j \varepsilon - \left(\mu + \frac{\mu_t}{\sigma_\varepsilon}\right)\frac{\partial \varepsilon}{\partial x_j}\right] = C_{\varepsilon_1}\frac{\varepsilon}{k}\left[\mu_t(P + P') - \frac{2}{3}\left(\mu_t \frac{\partial u_i}{\partial x_i} + \rho k\right)\frac{\partial u_i}{\partial x_i}\right] - C_{\varepsilon_2}\left(1 - 0.3e^{-Re_t^2}\right)\rho\frac{\varepsilon^2}{k} + C_{\varepsilon_3}\rho\varepsilon\frac{\partial u_i}{\partial x_i} \tag{4.31}$$

As in eq. (4.19), σ_ε denotes a turbulent Prandtl number, which is assumed constant and is given in Table 4.2 together with the constants C_{ε_1}, C_{ε_2} and C_{ε_3}. The term P' is given by:

$$P' = 1.33\left[1 - 0.3e^{-Re_t^2}\right]\left[P + 2\frac{\mu}{\mu_t}\frac{k}{y^2}\right]e^{-0.00375Re_y^2} \tag{4.32}$$

y is the normal distance to the nearest wall, and the Reynolds numbers Re_t and Re_y in eq. (4.31) and eq. (4.32) are defined as:

$$Re_t = \frac{k^2}{\nu\varepsilon} \tag{4.33}$$

$$Re_y = \frac{y\sqrt{k}}{\nu} \tag{4.34}$$

ν denotes kinematic viscosity.

For the near-wall cells (cells adjacent to the walls) the dissipation rate of turbulent kinetic energy is calculated according to:

$$\varepsilon = \frac{2\nu k}{y^2} \tag{4.35}$$

The turbulent viscosity is evaluated as:

$$\mu_t = f_\mu C_\mu \rho \frac{k^2}{\varepsilon} \tag{4.36}$$

C_μ is a constant, and f_μ is given by:

$$f_\mu = [1 - e^{-0.0198 Re_y}]\left(1 + \frac{5.29}{Re_y}\right) \tag{4.37}$$

The model constants for the low Re k-ε model are given in Table 4.2.

Model constants						
σ_k	σ_ε	$\sigma_{h,t}$	C_{ε_1}	C_{ε_2}	C_{ε_3}	C_μ
1.0	1.219	0.9	1.44	1.92	-0.33	0.09

Table 4.2 Constants in the low Re k-ε turbulence model [59].

When applying the low Re k-ε turbulence model, the y^+ value of the near-wall cells should be of the order of 1 [59]. The wall heat flux is calculated according to eq. (4.13).

4.1.1.3 k-ε RNG turbulence model

The applied k-ε RNG turbulence model of Yakhot et al. [58] differs from the two other models described above in that it employs wall functions and hence does not require a full resolution of wall boundary layers. The model equations [59] are given below with the model constants listed in Table 4.3.

Turbulent kinetic energy equation:

$$\frac{\partial}{\partial x_j}\left[\rho u_j k - \left(\mu + \frac{\mu_t}{\sigma_k}\right)\frac{\partial k}{\partial x_j}\right] = \mu_t P - \rho\varepsilon - \frac{2}{3}\left(\mu_t \frac{\partial u_i}{\partial x_i} + \rho k\right)\frac{\partial u_i}{\partial x_i} \tag{4.38}$$

The equation is the same as that applied in the V2F turbulence model. For explanation of variables, see therefore text below eq. (4.17).

Equation for the dissipation rate of turbulent kinetic energy:

$$\frac{\partial}{\partial x_j}\left[\rho u_j \varepsilon - \left(\mu + \frac{\mu_t}{\sigma_\varepsilon}\right)\frac{\partial \varepsilon}{\partial x_j}\right] = C_{\varepsilon_1}\frac{\varepsilon}{k}\left[\mu_t P - \frac{2}{3}\left(\mu_t \frac{\partial u_i}{\partial x_i} + \rho k\right)\frac{\partial u_i}{\partial x_i}\right] - C_{\varepsilon_2}\rho\frac{\varepsilon^2}{k} + C_{\varepsilon_3}\rho\varepsilon\frac{\partial u_i}{\partial x_i} - \frac{C_\mu \eta^3\left(1-\frac{\eta}{\eta_0}\right)}{1+\beta\eta^3}\frac{\rho\varepsilon^2}{k} \tag{4.39}$$

σ_ε denotes a turbulent Prandtl number and is assumed constant. The constants C_{ε_1}, C_{ε_2}, C_{ε_3} and C_μ are given in Table 4.3 together with the value of σ_ε. The constants η_0 and β are also listed in Table 4.3, and η is given by eq. (4.40) with S_{ij} defined as in eq. (4.11).

$$\eta = \frac{k}{\varepsilon}\sqrt{2S_{ij}S_{ij}} \tag{4.40}$$

The turbulent viscosity is given by:

$$\mu_t = C_\mu \rho \frac{k^2}{\varepsilon} \tag{4.41}$$

The model constants for the k-ε RNG model are given in Table 4.3.

Model constants								
σ_k	σ_ε	$\sigma_{h,t}$	C_{ε_1}	C_{ε_2}	C_{ε_3}	C_μ	η_0	β
0.719	0.719	0.9	1.42	1.68	-0.387	0.085	4.38	0.012

Table 4.3 Constants in the k-ε RNG turbulence model [59].

Due to the use of wall functions in the applied k-ε RNG turbulence model, the near-wall cell centroids are recommended to be located in the logarithmic region of the boundary layer, so that y^+ values of the near-wall cells are in the range 30 to 100 [59].

The assumed distributions of velocity, temperature and dissipation rate of turbulent kinetic energy across the boundary layer from the wall to the near-wall cell centroid are given below [59]. Hence, the values at the near-wall cell are obtained based on these distributions. The turbulent kinetic energy at the near-wall cell is obtained based on its transport equation, eq. (4.38), but with some modifications, which are mentioned below.

The velocity parallel to the wall u is given by the following profile:

$$u^+ = \begin{cases} \frac{1}{\kappa} ln(Ey^+) \ , & y^+ > y_m^+ \\ y^+ \quad , & y^+ \leq y_m^+ \end{cases} \tag{4.42}$$

where the dimensionless velocity u^+ is defined as:

$$u^+ = \frac{u}{u_\tau} \tag{4.43}$$

The dimensionless wall distance y^+ and the friction velocity u_τ are defined in eq. (4.28) and eq. (4.29) respectively. κ and E are constants (κ is the von Kármán constant) with values of 0.4 and 9.0, respectively.

The switch between linear and logarithmic velocity profile occurs in the model according to eq. (4.42) when $y^+ = y_m^+$, where y_m^+ satisfies:

$$y_m^+ = \frac{1}{\kappa} ln(Ey_m^+) \tag{4.44}$$

With the values of κ and E mentioned above, the switch occurs for y^+ = 11.6.

The temperature T is given by the following profile:

$$T^+ = \begin{cases} \sigma_{wf} \ (u^+ + \varphi) \ , & y^+ > y_T^+ \\ Pr \ y^+ \quad , & y^+ \leq y_T^+ \end{cases} \tag{4.45}$$

The dimensionless temperature T^+ is defined as:

$$T^+ = \frac{c_p \rho (T - T_w) u_\tau}{q_w} \tag{4.46}$$

q_w is the heat flux from the fluid to the wall, T_w is the wall temperature, and c_p denotes the specific heat capacity at constant pressure. In eq. (4.45), σ_{wf} denotes a turbulent Prandtl number, which is set to 0.9. Pr is the molecular Prandtl number defined earlier in eq. (1.2), and φ is a sublayer resistance factor given by:

$$\varphi = 9.24\left[\left(\frac{Pr}{\sigma_{wf}}\right)^{3/4} - 1\right]\left[1 + 0.28\, e^{\left(\frac{-0.007\, Pr}{\sigma_{wf}}\right)}\right] \tag{4.47}$$

The switch in temperature profile indicated by eq. (4.45) occurs when $y^+ = y_T^+$, where y_T^+ satisfies:

$$Pr\; y_T^+ - \sigma_{wf}\left(\frac{1}{\kappa} ln(E y_T^+) + \varphi\right) = 0 \tag{4.48}$$

y_T^+ thus depends on the molecular Prandtl number in the near-wall cells.

The dissipation rate of turbulent kinetic energy ε is given by:

$$\varepsilon^+ = \frac{{C_\mu}^{3/4}}{\kappa} \tag{4.49}$$

where the dimensionless dissipation rate ε^+ is defined in eq. (4.50), and the constant C_μ is given in Table 4.3.

$$\varepsilon^+ = \frac{\varepsilon\, y}{k^{3/2}} \tag{4.50}$$

The turbulent kinetic energy k is obtained from eq. (4.38) in which ε is now based on eq. (4.49), and P in the production term is set equal to $\left(\frac{\partial u}{\partial n}\right)^2$, where n is the coordinate in the direction normal to the wall, and u is the velocity parallel to the wall. The gradient $\frac{\partial u}{\partial n}$ is evaluated according to the velocity profile in eq. (4.42). Additionally, it is assumed that $\frac{\partial k}{\partial n} = 0$.

Calculation of the wall heat flux is based on the relation in eq. (4.46).

4.2 Numerical setup

In this section a description is given of the numerical setup used in the performed modeling of the jet impingement process described in section 3.1.

4.2.1 Geometry and mesh

The jet impingement flow in the configuration depicted in Fig. 3.1 was for simplicity assumed axisymmetric in the numerical modeling. Due to this assumption the model geometry was constructed as a cylinder sector. The dimensions of the geometry were 0.10 m × 0.30 m in vertical and horizontal directions, respectively, while the extent in the azimuthal direction was 5°. The geometry height was based on the value given in Table 3.1 for the distance between the jet inlet and the wall. The horizontal extent of the model geometry was based on that it should be large enough, so that the location of the right boundary, which was a pressure boundary, would not influence the wall heat transfer results. A check of this is presented in section 6.1.4. The azimuthal extent was based on recommendations by the developer of the applied CFD code. The azimuthal angle should not be too low as this could cause difficulties in reaching convergence in the computations. With a jet diameter at the inlet of D = 0.05 m as listed in Table 3.1, the dimensions in vertical and horizontal directions correspond to 2D and 6D, respectively. The mesh was a cylindrical structured mesh with a gradually refinement near the wall in the wall normal direction. In the azimuthal direction, the mesh consisted of only one cell due to the two-dimensionality assumption for the flow. The mesh is illustrated in Fig. 4.1. Further details of the applied mesh, i.e. number of cells and distribution, are given in section 6.1.3, where a mesh independency study is presented.

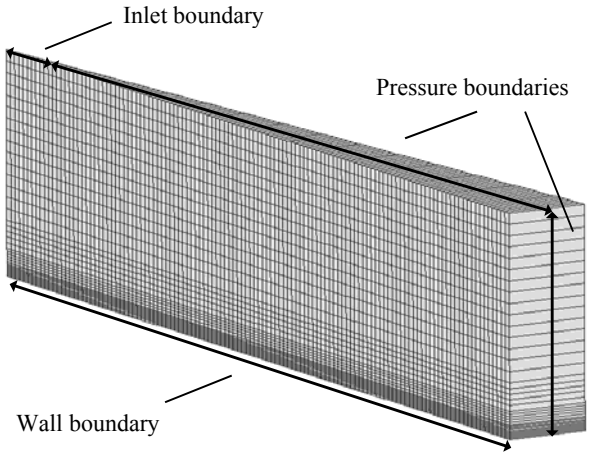

Fig. 4.1 Computational mesh and boundary conditions.

4.2.2 Boundary conditions

An inlet boundary condition was imposed on the upper face of the model geometry from the center and up to a radius of 0.025 m. The conditions at the inlet were based on the values shown in Table 3.1. The temperature of the incoming gas was specified to 2000°C

and the velocity to 10 m/s. The velocity was constant across the inlet and perpendicular to the inlet. The turbulence intensity at the inlet was specified to 5%, and the turbulence length scale was set to 7% of the jet diameter at the inlet, i.e. 0.0035 m. The specified length scale was based on information in [47] about it typically being 7% of the characteristic length for a given flow. Pressure boundary conditions were imposed on the remainder part of the upper face and on the right face with a static pressure of 180 bar and a temperature of the incoming flow of 2000°C, cf. Table 3.1. A zero-gradient condition was specified for the turbulence of the incoming flow. On the lower face of the model geometry, a no-slip wall boundary condition was imposed with a fixed temperature of 400°C. Symmetry boundary conditions were imposed on each side face of the model due to the two-dimensionality assumption of the flow in the configuration. The boundary conditions are indicated in Fig. 4.1, expect for the symmetry boundaries on the side faces. The different values mentioned here were specified as boundary conditions in the reference case. Several of these values were subsequently varied in parameter studies, which are presented in section 6.2.

4.2.3 Turbulence model

The turbulence model applied in the numerical setup was mainly the V2F model as mentioned in section 4.1, but simulations were also performed with the two other turbulence models described in section 4.1.1. These models were a low Re k-ε model and a k-ε RNG model employing wall functions. For further details on the turbulence models, see section 4.1.1.

4.2.4 Thermophysical properties and density

Due to the large temperature difference of 1600K imposed between jet inlet and wall, temperature dependent thermophysical properties and density ρ were applied in the numerical modeling. The properties were thermal conductivity λ, dynamic viscosity μ and specific heat capacity at constant pressure c_p. Polynomial expressions for the temperature dependency were derived based on data for real gas properties of air at a pressure of 180 bar [63]. The expressions did not take into account pressure dependency as it was assumed that pressure variation in the computational domain would be small. Based on the data in [63], it was also noted that the pressure dependency on the thermophysical properties was relatively small compared to the temperature dependency, especially at high temperatures. The simulation results later showed that the pressure variation in the computational domain was in fact only of the order of 1 kPa. The variation of the thermophysical properties and density with temperature is shown in Fig. 4.2 – Fig. 4.5 in the range from 280K to 2500K based on data from [63]. In the figures are also shown values based on the derived polynomial expressions, and it is seen that the polynomials predict the data well. The density of air calculated using the ideal gas law is shown in Fig. 4.5 for comparison to the real gas data. A clear difference is observed between the real gas and ideal gas density with the largest absolute difference being at

low temperatures for the case of 180 bar. The relative difference is approximately 30% and is nearly constant over the temperature range.

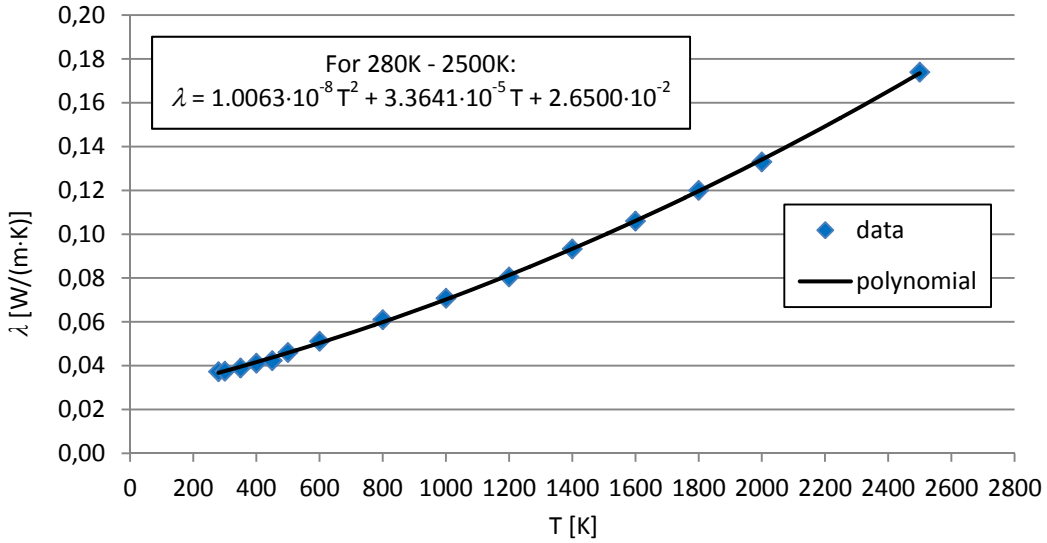

Fig. 4.2 Variation of thermal conductivity of air with temperature at 180 bar – real gas data.

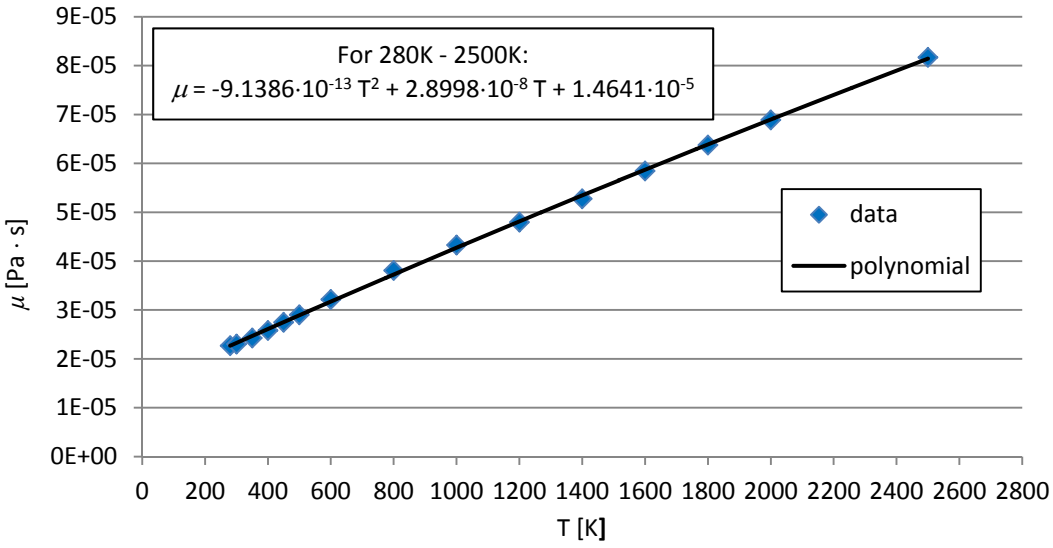

Fig. 4.3 Variation of dynamic viscosity of air with temperature at 180 bar – real gas data.

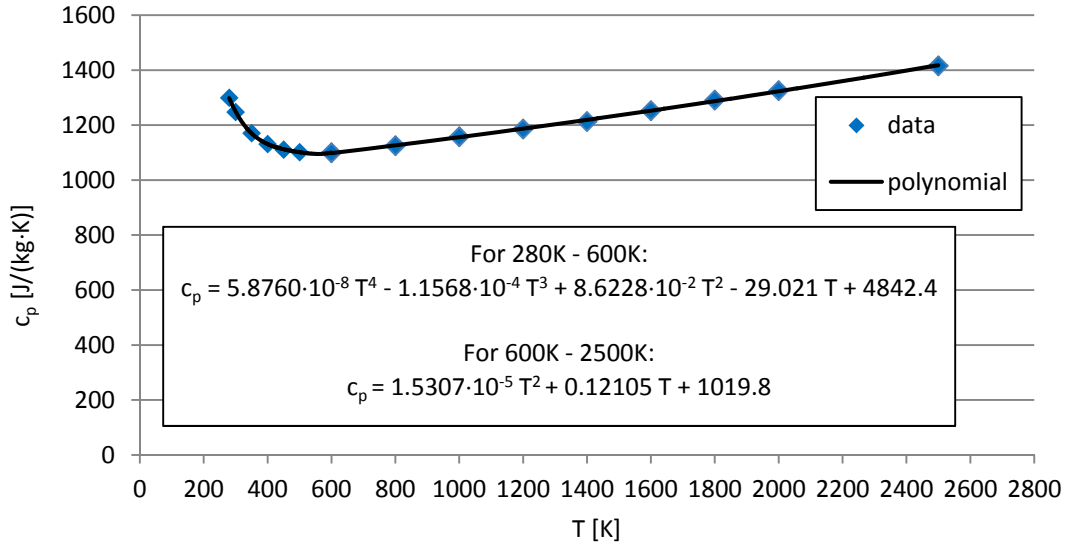

Fig. 4.4 Variation of specific heat capacity at constant pressure of air with temperature at 180 bar – real gas data.

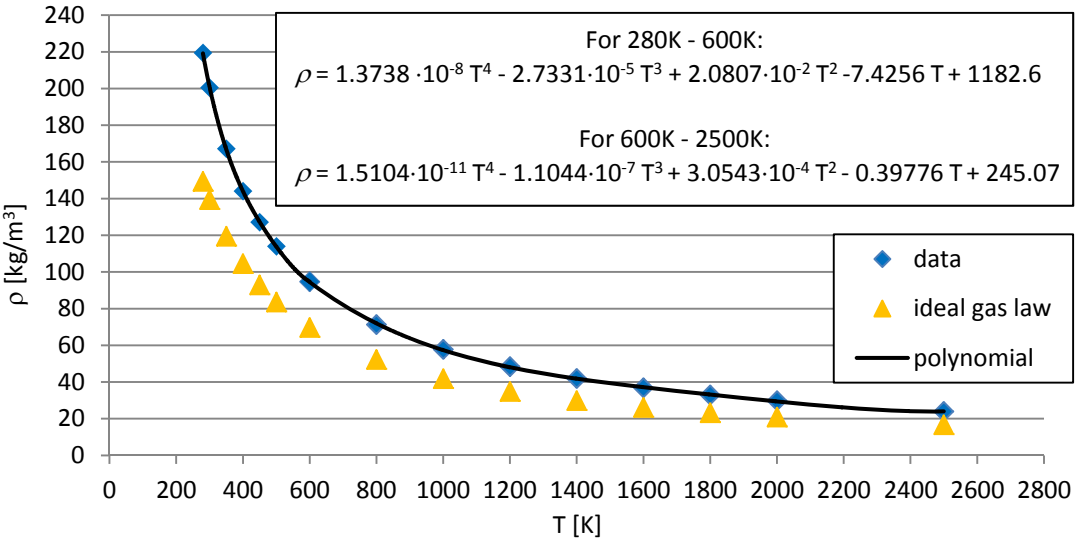

Fig. 4.5 Variation of density of air with temperature at 180 bar – real gas data and predictions by the ideal gas law.

4.2.5 Discretization scheme, solution algorithm and convergence criteria

The second order central difference scheme was used for discretization of the governing continuity, momentum, energy and turbulence equations. The solution algorithm applied was the SIMPLE algorithm described in e.g. [64]. Convergence checks were performed

by observing changes in the wall heat flux with decreasing global residuals[4] during the iteration steps. A computation was considered converged if the wall heat flux distribution along the wall did not change with further decrease in the global residuals. The change in wall heat flux was chosen as the measure of convergence because it was the main result of interest in the calculations. However, changes in the wall shear stress distribution and in the y^+ values of the near-wall cells with decreasing global residuals were also monitored in the check for convergence. It was found that in general the global residuals needed to be in the order of 10^{-7} before convergence was reached. To reduce the global residuals to this order of magnitude typically required 50000 iterations or more and the test of many combinations of relaxation factor[5] values for the different variables. The large number of iterations required to obtain convergence is believed to be due to the application of pressure boundaries on large parts of the domain surface. This may cause a slower convergence rate and increase numerical instability as stated in the documentation of the applied CFD code [65]. Also the presence of very small cells near the wall in order to resolve the wall boundary layer and the application of the central difference scheme for discretization may have contributed to the convergence difficulties.

4.2.6 General comments on the numerical modeling

Radiation heat transfer was not included in the numerical modeling for simplicity. It was also expected that including thermal radiation would not represent the actual in-cylinder radiation contribution to the piston surface heat transfer, because the gas in the model was pure air, i.e. no soot particles or combustion product species were present. As previously mentioned, especially soot particles are important for the heat transfer by thermal radiation in diesel engines. The model results are hence only valid for estimations of the convective heat transfer contribution.

The modeled jet impingement configuration was intended to approximate the situation of impingement of hot combustion products on the piston surface in the considered diesel engines. Hence, it was not intended to approximate a classical jet impingement configuration, where a jet is issuing from a pipe with a fully developed pipe flow profile, and in which there is a pipe wall between the jet at the inlet and the surrounding fluid.

[4] The global residual for a variable is the normalized sum over all cells in the computational domain of the local cell residual, which is the imbalance in the discretized equation for the variable at the local cell.

[5] The solution ϕ for a variable is obtained according to $\phi^k = \alpha\ \phi^{k*} + (1 - \alpha)\ \phi^{k-1}$, where k denotes the iteration number. ϕ^{k*} is the solution at the kth iteration before relaxation modification. α is the relaxation factor, and $0 < \alpha \leq 1$. The solution at the kth iteration ϕ^k is thus determined as a weighted mean of the solution at the previous iteration step and at the current iteration step (before relaxation modification).

5 Validation study

A validation study of the numerical modeling has been performed, where model predictions were compared to experimental data. The validation study is presented in this chapter.

The jet impingement heat transfer study by Baughn and Shimizu [39] was used in the present validation study. They investigated experimentally the heat transfer from a surface with a uniform heat flux to a round turbulent impinging air jet. The heat flux was obtained by electrical heating of a thin gold coating imbedded just below the surface, see Fig. 5.1. To measure the surface temperature, they applied a liquid crystal technique where a coating of liquid crystals on the surface would indicate isotherms with a constant color. The jet was issuing from a long pipe of 72 pipe diameters. The pipe flow was stated to be nearly fully developed at the pipe exit. The air temperature at the pipe exit equaled the ambient air temperature. Baughn and Shimizu investigated the heat transfer for *H/D* ratios of 2, 6, 10 and 14, where *H* is the distance between pipe exit and impingement wall (denoted by Z in Fig. 5.1), and *D* is the pipe diameter. The measurements were performed for a jet Reynolds number of 23750. The jet Reynolds number is defined as:

$$Re = \frac{\rho U_b D}{\mu} \tag{5.1}$$

ρ denotes density, U_b is the bulk velocity of the pipe flow, and μ denotes dynamic viscosity. The experimental measurements reported by Baughn and Shimizu in [39] have previously been used as validation data for numerical modeling of jet impingement heat transfer by other investigators, e.g. Behnia et al. [48], [49] and Craft et al. [66]. Numerical predictions obtained in the present validation study have also been compared to the experimental heat transfer data of Yan et al. [67], who performed measurements for *Re* = 23000, *Re* = 50000 and *Re* = 70000. The experimental heat transfer data of Baughn et al. [40] were also used in the present validation study. They performed measurements for *Re* = 23300. Both the experimental setup used by Yan et al. [67] and that used by Baughn et al. [40] were reported to be basically the same as the setup in the investigation by Baughn and Shimizu [39]. Furthermore, numerical predictions of the flow field near the wall obtained in the present validation study have been compared to experimental flow field measurements performed by Cooper et al. [68]. The experiments carried out by Cooper et al. were performed on a setup designed to approximate the setup used by Baughn and Shimizu. Hence, flow field measurements were provided to accompany the heat transfer measurements of Baughn and Shimizu, so these data together could be used for validation of numerical results. The measurements of Cooper et al. were performed for *Re* = 23000 and *Re* = 70000 at *H/D* ratios of 2, 4, 6 and 10.

The experiments by Baughn and Shimizu [39], Yan et al. [67] and Baughn et al. [40] were performed for jet Reynolds numbers between 23000 and 70000, while the jet Reynolds number for the jet impingement configuration, described in section 3.1, was

166101[6] in the reference case given in Table 3.1. The reason for choosing the experimental data of Baughn and Shimizu, Yan et al. and Baughn et al. for validation purpose was that their data were considered to be well-established for numerical model testing, and that no well-documented data for $Re > 100000$ and $H/D = 2$ were found.

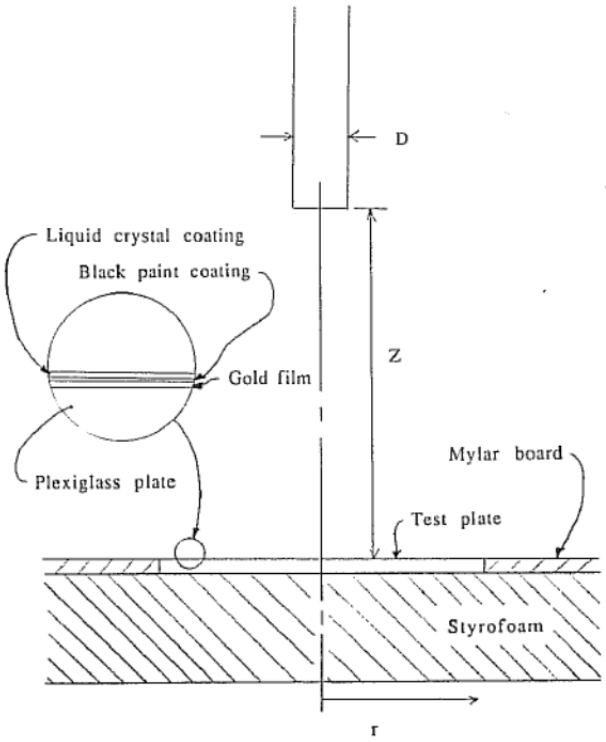

Fig. 5.1 Jet impingement setup in experiment by Baughn and Shimizu [39].

5.1 Numerical setup for validation study

The numerical setup applied in the validation study is described in the following subsections as it differed at some points from that described in section 4.2.

5.1.1 Geometry and mesh

The computational domain in Fig. 4.1 was modified to closely approximate the configuration in the experiment by Baughn and Shimizu in order to avoid differences in the results caused by differences in the experimental and numerical configurations. Hence, the computational domain was extended upwards in order to include a piece of pipe wall. The extended domain started two pipe diameters upstream of the pipe exit, and the pipe wall thickness was $t = 5.6$ mm, i.e. $t/D = 0.112$, corresponding to the t/D ratio in

[6] The evaluation of the jet Reynolds number for the jet impingement configuration described in section 3.1 is discussed in section 6.4.

the experiment by Baughn and Shimizu. In radial direction the domain was extended to 10 pipe diameters. The domain size was based on the domain size used in the numerical jet impingement heat transfer study by Behnia et al. [48]. They obtained jet impingement heat transfer predictions using the V2F turbulence model, which were in good agreement with the experimental measurements of Baughn and Shimizu [39], Baughn et al. [40] and Yan [69]. The applied mesh in the validation study was, similar to that described in section 4.2, a cylindrical structured mesh. The mesh was gradually refined near all wall boundaries and near the centerline axis. It consisted of 20476 cells in total with a high cell density in the stagnation area. The mesh is shown in Fig. 5.2.

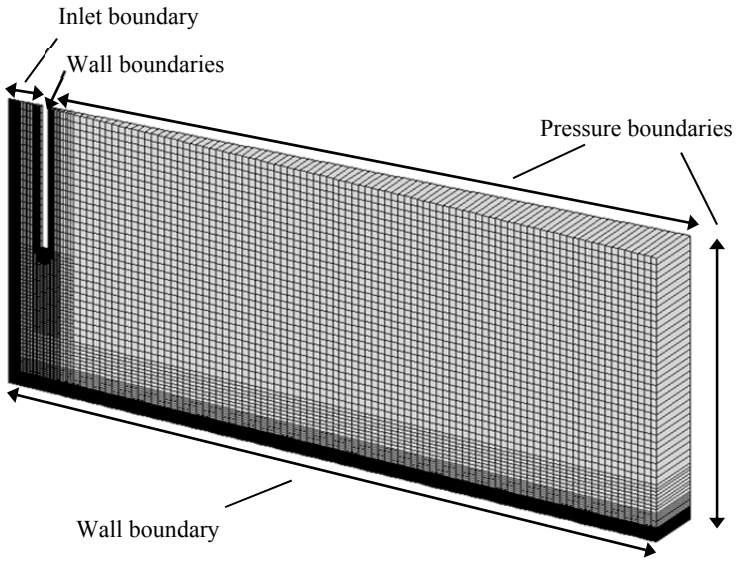

Fig. 5.2 Computational mesh for the validation case corresponding to the jet impingement heat transfer study by Baughn and Shimizu [39].

5.1.2 Boundary conditions

Pressure boundary conditions with a static pressure of 1 bar were imposed on the upper and on the right boundary as indicated in Fig. 5.2. The temperature of the incoming flow at the upper boundary was fixed to 20°C, which equaled the temperature of the incoming jet, and a zero gradient condition was imposed for turbulence. On the lower boundary of the domain, a no-slip wall boundary condition was imposed with a constant uniform heat flux of 500 W/m^2 into the computational domain. The magnitude of the heat flux was chosen in order to obtain a difference of about 10K between the wall temperature in the stagnation region and the jet temperature at the inlet. This was based on that Baughn and Shimizu [39] reported a temperature difference of this magnitude in their experiment. No-slip adiabatic wall boundary conditions were imposed on the inner, outer and lower faces of the pipe wall. On each side of the computational domain, symmetry boundary

conditions were imposed as in the numerical setup described in section 4.2. An inlet boundary condition was imposed at the pipe piece inlet, where the temperature of the incoming flow was set to 20°C. Fully developed pipe flow profiles for velocity and turbulence were imposed at the inlet. These had first been obtained in a separate pipe flow computation, which was performed using the cylindrical mesh shown in Fig. 5.3. The mesh consisted of one row of cells with imposed cyclic boundary conditions at the top and bottom faces. Symmetry boundary conditions were imposed in the azimuthal direction, and a no-slip adiabatic wall boundary condition was imposed at the end face. The mesh with boundary conditions thus represented an infinitely long axisymmetric pipe. The thermophysical properties and density in the pipe flow computation were assumed constant and were evaluated for air at 20°C and 1 bar. At the cyclic boundaries a mass flow rate was imposed, which resulted in a Reynolds number of 23750 as in the experiment of Baughn and Shimizu. The bulk velocity of the pipe flow was 7.25 m/s. The obtained profiles for velocity, turbulent kinetic energy and its dissipation rate together with the turbulence parameters $\overline{v_2}$ and f of the V2F turbulence model (see section 4.1.1.1 for details) were subsequently imposed at the inlet boundary in the jet impingement setup.

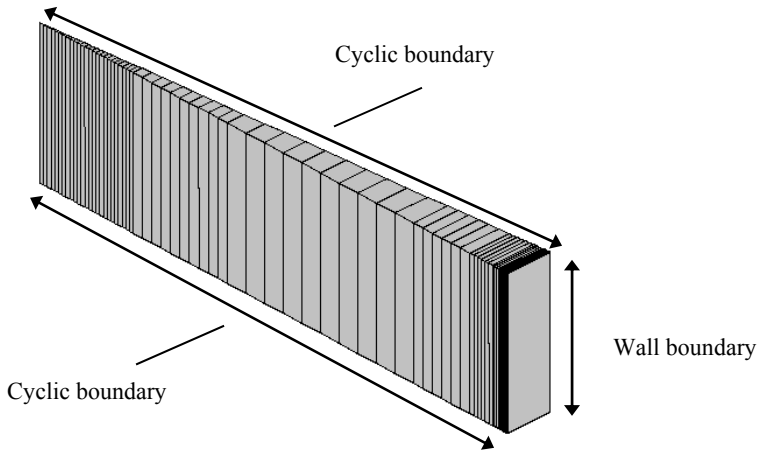

Fig. 5.3 Computational mesh for pipe flow computation.

5.1.3 Turbulence model

The V2F turbulence model was applied as in the numerical setup described in section 4.2. Due to the application of the V2F model, no wall functions were needed. Instead a full resolution of the wall boundary layers was required in order to reach y^+ values of the near-wall cells of about 1.

5.1.4 Thermophysical properties and density

The fluid in the computational domain was air, and the density was assumed to obey the ideal gas law but without pressure dependency. The pressure variations in the domain were small, in the order of 40 Pa. The thermophysical properties, i.e. thermal conductivity λ, dynamic viscosity μ and specific heat capacity at constant pressure c_p, were assumed constant in the computational domain due to the small temperature and pressure variations in the domain. The properties were evaluated at 20°C and 1 bar using data in [63].

5.1.5 Discretization scheme, solution algorithm and convergence criteria

The central difference scheme was used for discretization of the governing continuity, momentum, energy and turbulence equations, and the SIMPLE solution algorithm [64] was applied. The change in wall temperature distribution along the impingement wall with decreasing global residuals[7] was monitored to decide if convergence in the computations had been reached. Changes in the wall shear stress distribution along the impingement wall and in the y^+ values of the near-wall cells were also monitored. The global residuals needed to be in the order of 10^{-6} before convergence in the computations was reached.

5.2 Results

In this section, the results obtained in the validation study are presented. The heat transfer parameter of interest is the resulting Nusselt number along the wall. The Nusselt number is compared in magnitude and distribution to experimentally obtained results. Near-wall velocity profiles obtained in the numerical computations are also compared to experimentally obtained profiles to provide a better basis for the validation of the numerical modeling.

5.2.1 Flow and scalar fields

Before comparisons of numerical and experimental results are presented, results of the computations are first visualized to provide a general picture of the obtained flow field. The presented results are for the case of Re = 23750. The flow pattern in the computational domain is visualized by streamlines in Fig. 5.4.

[7] See footnote in section 4.2.5 for explanation.

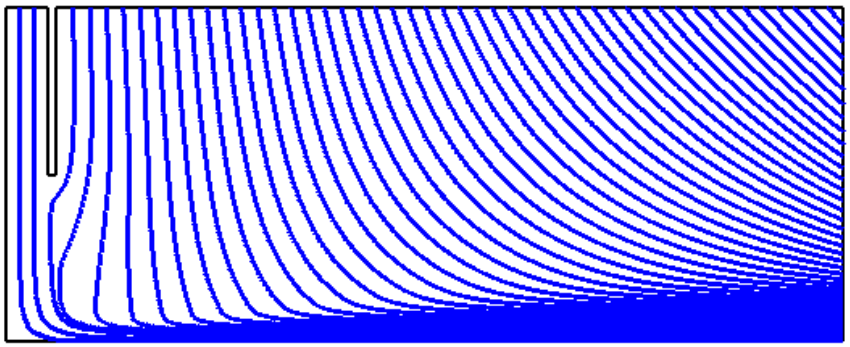

Fig. 5.4 Streamlines in the computational domain corresponding to the experimental configuration in the study of Baughn and Shimizu [39].

The jet flow issues from the pipe exit, approaches the wall in the stagnation area, while it is decelerated due to the presence of the wall. The jet is deflected away from the stagnation point in the outward direction, where it first accelerates and then turns into a decelerating wall jet, due to wall friction and momentum exchange with the surrounding air. The surrounding air enters the domain at the upper boundary due to the motion produced by the jet flow and is directed into an outward going direction and exits at the right boundary together with the jet flow.

The velocity magnitude distribution in the computational domain is depicted in Fig. 5.5. The maximum velocity of the pipe flow is 8.55 m/s at the center axis. The velocity decreases towards the pipe wall to meet the no-slip boundary condition at the wall. After exiting the pipe, the jet flow velocity decreases at the outer border due to momentum exchange with the surrounding air, and the jet is broadened. The deceleration of the jet flow near the stagnation point is indicated by the decrease in velocity, when the jet is approaching the wall. The subsequent acceleration of the jet flow in the outward direction along the wall is also observed as well as the later deceleration of the flow. At the end of the acceleration region, it may seem as if the flow close to the wall does not meet the no-slip wall boundary condition as the velocity close to the wall is high. A close-up of this region confirmed however that the no-slip condition at the wall is satisfied. The thickness of the velocity boundary layer along the wall is seen to increase with increasing distance from the stagnation point. The velocity of the surrounding air is relatively low compared to the jet flow.

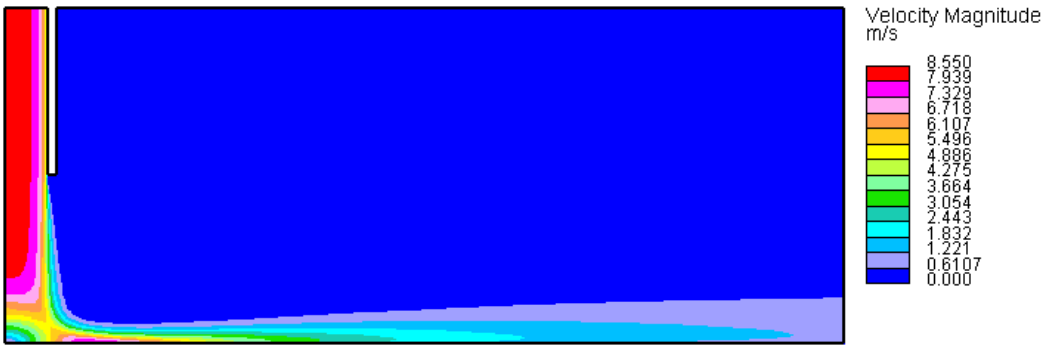

Fig. 5.5 Velocity magnitude in the computational domain corresponding to the experimental configuration in the study of Baughn and Shimizu [39].

Different observed features of the flow in the computational domain are depicted in Fig. 5.6 – Fig. 5.8. The length of the velocity vectors is proportional to the velocity magnitude, but the vector distributions are based on presentation grids.

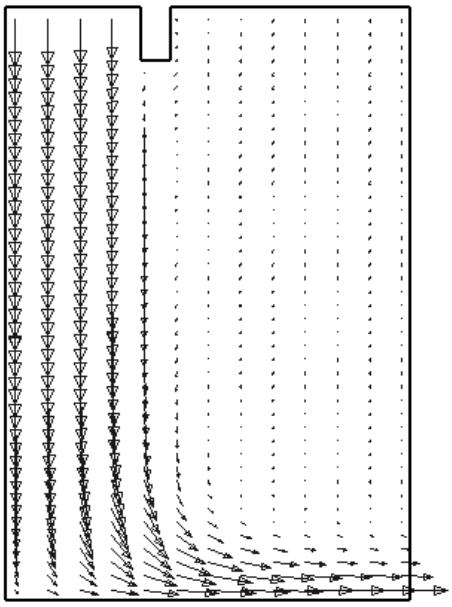

Fig. 5.6 Flow in the stagnation region. The vector distribution is based on a presentation grid.

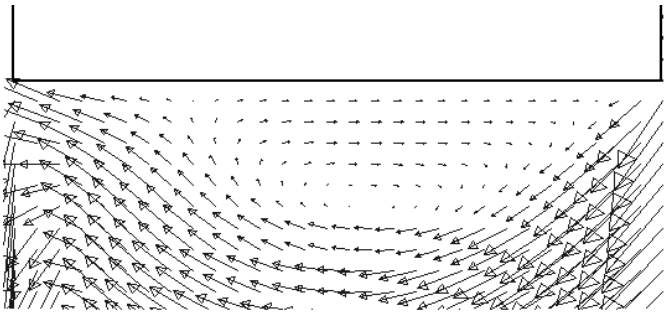

Fig. 5.7 Recirculating flow under the pipe wall. The vector distribution is based on a presentation grid.

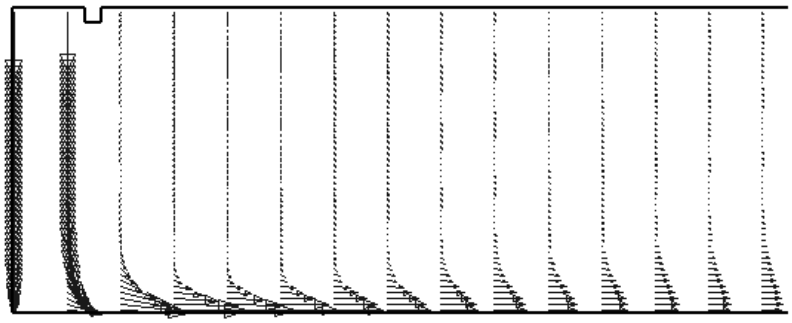

Fig. 5.8 Wall jet development. The vector distribution is based on a presentation grid.

The flow in the stagnation region is shown in Fig. 5.6. The flow deceleration normal to the wall and the acceleration parallel to the wall are changing the flow direction from vertical to horizontal. Fig. 5.7 shows a strong zoom on the region below the pipe wall, where a recirculation zone is observed. The recirculation zone was also observed by Behnia et al. [48] in their numerical computations. The formation of a wall jet along the wall is indicated in Fig. 5.8, where a portion of the lower part of the domain is shown. The increase in thickness of the velocity boundary layer with increasing distance from the stagnation point is seen together with the development of the pear shaped velocity distribution in the boundary layer.

A visualization of the mixing of air issuing from the pipe with the surrounding air is presented in Fig. 5.9. The figure depicts the mass fraction of pipe air across the domain (in kg/kg). The mass diffusivity was $D_m = 3 \cdot 10^{-5}$ m^2/s resulting in a Schmidt number of $Sc = \mu/(\rho D_m) = 0.51$ in most of the computational domain. Close to the wall, the Schmidt number increased slightly (up to $Sc = 0.58$) due to a higher gas temperature, and thereby a lower gas density, in the near-wall region. The turbulent Schmidt number was $Sc_t = 0.9$.

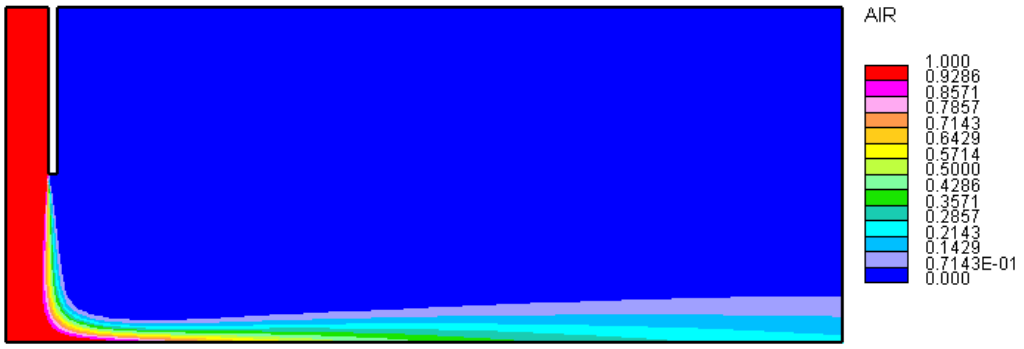

Fig. 5.9 Mass fraction of pipe air across the computational domain corresponding to the experimental configuration in the study of Baughn and Shimizu [39].

The formation of a mixing layer downstream of the pipe exit is observed, where surrounding air is entrained into the jet. However, the surrounding air does not reach a full penetration into the jet as a consequence of the short distance between the pipe exit and the wall when compared to the initial jet diameter. The relative distance is $H/D = 2$. Along the wall, the surrounding air is entrained into the jet flow as well.

The obtained temperature field is shown in Fig. 5.10. The temperature in most of the domain is close to the jet temperature at the inlet, which is 20°C. The maximum temperature is 60.15°C and occurs near the wall next to the right boundary. The thermal boundary layer along the impingement wall is thin in the stagnation region, where it is almost not visible in Fig. 5.10. The thickness δ_t of the thermal boundary layer can be defined [25] as the distance from the wall for which:

$$\frac{T_w - T}{T_w - T_\infty} = 0.99 \tag{5.2}$$

T is the local fluid temperature, T_w is the local wall temperature, and T_∞ is the free stream temperature. Using this definition of δ_t, the thickness of the thermal boundary layer in the stagnation point is found to be $\delta_t = 1.6$ mm. The thickness of the thermal boundary layer at the right end of the domain is $\delta_t = 3.5$ cm.

Fig. 5.10 Temperature field in the computational domain corresponding to the experimental configuration in the study of Baughn and Shimizu [39].

5.2.2 Velocity profiles

Velocity profiles normal to the wall obtained in the numerical computations at different radial positions along the wall are compared to the corresponding velocity profiles obtained in the experiments by Cooper et al. [68]. The normalized velocity profiles are presented in Fig. 5.11. U denotes the local velocity magnitude, and the normalizing factor U_b is the pipe flow bulk velocity of 7.25 m/s. The distance from the wall z and the radial position r are non-dimensionalized by the pipe diameter D. The symbols in the figure denote the experimental data of Cooper et al. [68].

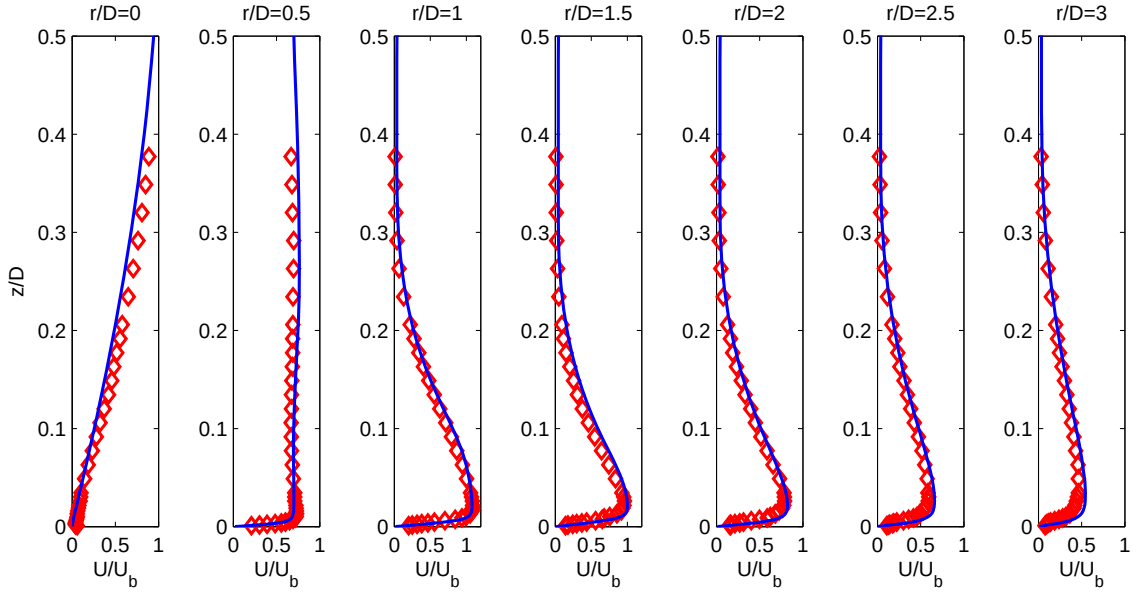

Fig. 5.11 Obtained velocity profiles at different radial positions along the wall for Re = 23750 based on velocity magnitude. Symbols denote experimental data of Cooper et al. [68] for Re = 23000.

The obtained velocity profiles in the numerical computations are in good agreement with the experimental data, so the evolution of the velocity profile is well predicted by the model. However, a slight deviation from the data is observed at $r/D = 0$ and to some extend also at $r/D = 0.5$, when moving away from the wall. Near the wall, for r/D > 1, an overprediction of the velocity magnitude is observed, which slightly increases with increasing radial distance from the stagnation point. The observed discrepancies may be attributed to the numerical modeling. A reason may also be that the profiles extracted from the simulation are not exactly at the noted radial locations but within 3% of the stated values. The average and maximum difference between the non-dimensional experimental and numerical velocity magnitude U/U_b are 0.06 and 0.20, respectively, indicating a mean and a maximum error in the numerically predicted local velocity magnitude of 6% and 20%, respectively, of the pipe flow bulk velocity U_b.

A simulation was additionally performed for a jet Reynolds number of 70000. The numerical setup was basically the same as that used in the case of $Re = 23750$ and described in section 5.1. The mesh was however slightly more refined at the pipe wall in order to resolve the wall boundary layer sufficiently for the application of the turbulence model. The total number of cells was therefore 20544. The higher jet Reynolds number was obtained by increasing the bulk velocity U_b in the pipe flow calculation to 21.37 m/s. The velocity profiles at positions along the wall are presented in Fig. 5.12. Experimental data of Copper et al. [68] for $Re = 70000$ are included in the figure for comparison. As in Fig. 5.11, the radial positions for the numerical results presented in Fig. 5.12 are not exactly corresponding to the indicated positions but are within 3% of those.

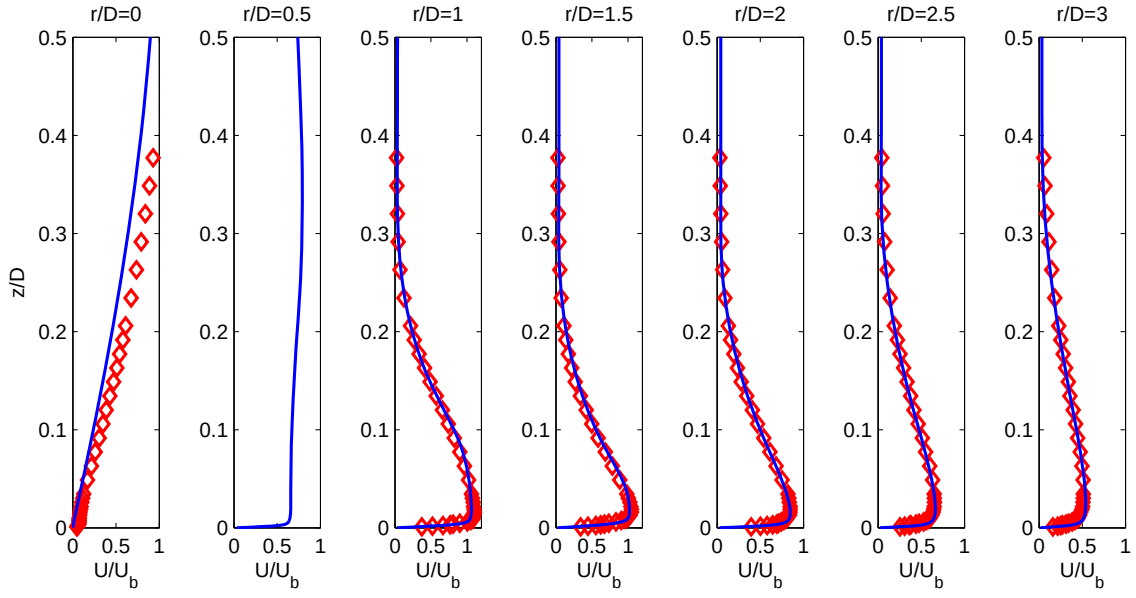

Fig. 5.12 Obtained velocity profiles at different radial positions along the wall for $Re = 70000$ based on velocity magnitude. Symbols denote experimental data of Cooper et al. [68] for $Re = 70000$.

In general the numerical results predict well the velocity profiles along the wall for Re = 70000 as in the case of Re = 23750. However, a discrepancy between the numerical and experimental data is observed at r/D = 0, when moving away from the wall, and it is slightly more pronounced than for the case of Re = 23750. At the rest of the radial positions, the velocity profiles are predicted very well. The average and maximum difference between the non-dimensional experimental and numerical velocity magnitude U/U_b are 0.04 and 0.17, respectively, for the case of Re = 70000, which indicates a mean and a maximum error in the numerically predicted local velocity magnitude of 4% and 17%, respectively, of the pipe flow bulk velocity U_b. No experimental measurements were available for a non-dimensional radial position of r/D = 0.5, and therefore only numerical results are shown at that position.

5.2.3 Nusselt number distributions

The obtained numerical prediction of the Nusselt number distribution along the impingement wall is presented in this section and compared to the experimental data of Baughn and Shimizu [39], Yan et al. [67] and Baughn et al. [40]. The Nusselt number Nu is defined as:

$$Nu = \frac{hD}{\lambda} \tag{5.3}$$

λ is the thermal conductivity, h is the heat transfer coefficient, and D is the pipe diameter. The thermal conductivity was kept constant in the numerical computations as mentioned in section 5.1.4. It was evaluated at the jet temperature at the pipe exit, i.e. 20°C, and a pressure of 1 bar. The heat transfer coefficient h is defined via Newton's law of cooling, which was mentioned in section 2.1.1. With q_w denoting the heat flux to the wall and T_j and T_w denoting the jet temperature at the pipe exit and the wall temperature, respectively, h is given by:

$$q_w = h\left(T_j - T_w\right) \tag{5.4}$$

The Nusselt number is usually interpreted as the dimensionless heat transfer coefficient, or as the dimensionless temperature gradient at the wall.

The obtained distribution of the Nusselt number along the wall for Re = 23750 is presented in Fig. 5.13. The Nusselt number distribution predicted using a refined grid is also shown in the figure in order to observe if grid independency has been obtained in the computation. The refined grid is similar to that shown in Fig. 5.2 but with twice as many cells in horizontal and vertical directions, thus resulting in a total of 81904 cells. The Nusselt number distributions obtained with the reference and refined grid, respectively, are seen to be almost coinciding. The maximum relative difference between the distributions is 2% at r/D = 9.6. Hence, the distribution obtained with the reference grid is considered to be grid independent. The values of the dimensionless wall distance y^+ of

the near-wall cells were additionally checked. The dimensionless wall distance has previously been defined in eq. (4.28). The maximum resulting y^+ value of the near-wall cells in the case of the reference grid was 0.69, while it was 0.35 in the case of the refined grid. The applied V2F turbulence model required a maximum y^+ value of 1 [59], so the resolution of the wall boundary layers were considered to be sufficient.

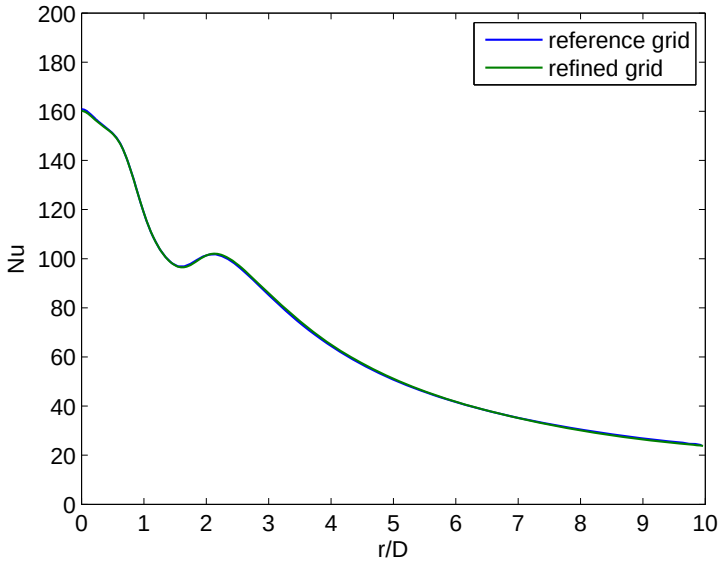

Fig. 5.13 Nusselt number distribution obtained with different grids for Re = 23750.

Regarding the predicted distribution of the Nusselt number, it is observed that the Nusselt number is highest in the stagnation point with a value of 161. The Nusselt number generally decreases with increasing radial distance from the stagnation point to reach a value of 24 at r/D = 10. A local secondary peak is observed at a radial distance of r/D = 2.15. The appearance of a secondary peak in the Nusselt number distribution has been reported in previous experimental works for a configuration of H/D = 2 as in the present study, e.g. [39], [70], [38]. In these works the location of the secondary peak ranged from r/D = 2.0 to r/D = 2.3 possibly due to different jet Reynolds numbers, which varied between 23750 and 375000. The secondary peak has been suggested to be caused by a transition from a laminar to a turbulent boundary layer flow [54], [71]. Other researchers have suggested that it is caused by an augmentation of turbulent kinetic energy due to high shear in the region of streamline convergence [48], [49].

The obtained Nusselt number distribution is compared to the experimental data of Baughn and Shimizu [39], Baughn et al. [40] and Yan et al. [67] in Fig. 5.14. Numerical results of Behnia et al. [48], obtained using the V2F turbulence model, are also included in the figure for comparison.

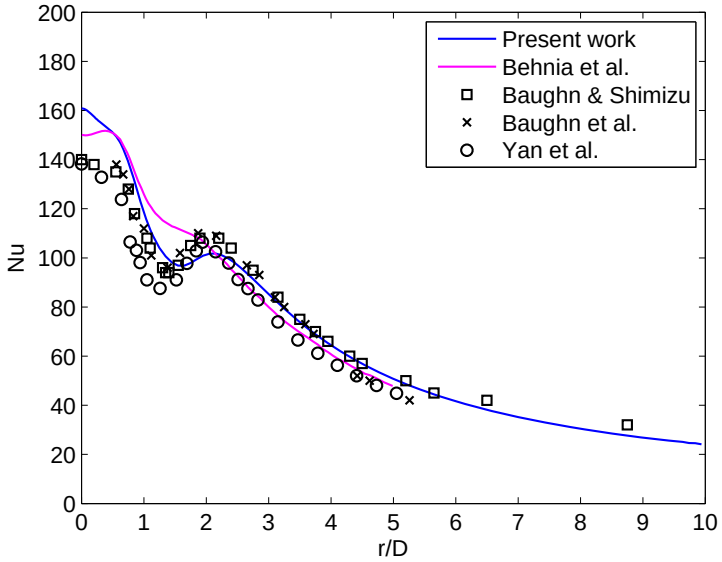

Fig. 5.14 Comparison of numerical and experimental Nusselt number distributions. Numerical results obtained in the present work for Re = 23750 vs. experimental data of Baughn and Shimizu [39] for Re = 23750, Baughn et al. [40] for Re = 23300 and Yan et al. [67] for Re = 23000. The numerical results of Behnia et al. [48] for Re = 23000 are also included in the figure.

The Nusselt number distribution obtained in the present work is in good agreement with the experimental data along most of the wall, especially in the wall jet region. In the stagnation region, however, and around the secondary peak observed at r/D = 2.15, some disagreement is noted between the numerical results obtained in the present work and the experimental results. Most pronounced is the disagreement in the stagnation region. The predicted Nusselt number in the stagnation point is Nu_0 = 161, whereas that obtained in the experiments is Nu_0 = 140, thus resulting in a deviation of 15%. A reason for the disagreement may be differences between the turbulence at the pipe exit in the experiments and numerical computation. Previously it has been observed experimentally by den Ouden and Hoogendoorn [72] and Hoogendoorn [73] that the turbulence intensity TI at the pipe exit has a significant influence on the wall heat transfer in the stagnation region. Baughn and Shimizu [39] reported that the turbulence intensity at the center of the jet at the pipe exit was 4.1% for a case of Re = 21000. Baughn et al. [40] also reported the turbulence intensity at the center of the jet at the pipe exit to be 4.1% in their experiments at Re = 23300. Yan et al. [67] did not provide information about the turbulence intensity. The turbulence intensity at the pipe exit in the numerical computation in the present work was calculated for comparison. The intensity, defined in eq. (3.1), was calculated according to eq. (5.5), where k denotes turbulent kinetic energy.

$$TI = \frac{\sqrt{\frac{2}{3}k}}{\sqrt{U_i U_i}} \tag{5.5}$$

The turbulence intensity at the center of the jet at the pipe exit was found to be $TI = 4.1\%$ and is hence in excellent agreement with the experimental findings. The difference between experimental results and the numerical results of the present work may thus simply be caused by insufficient ability of the numerical model to predict the true Nusselt number distribution in the stagnation region. It is noticed that the computation performed by Behnia et al. [48] using the V2F model also overpredicts the Nusselt number in the stagnation region, although the overprediction is less than that of the computation in the present work. The secondary peak in the Nusselt number is however seen to be better predicted by the computation in the present work than by that of Behnia et al. The difference in the two sets of numerical results is probably due to the fact that Behnia et al. used a version of the V2F model in which the model equations and model constants are slightly different from those in the version implemented in the STAR-CD code applied in the present work.

Numerical Nusselt number predictions for $Re = 70000$ are presented in Fig. 5.15. Results obtained with the reference grid, which in this case consisted of 20544 cells as mentioned in section 5.2.2, are presented together with results obtained using a refined grid. The refined grid consisted of twice as many cells in both horizontal and vertical direction as the reference grid, thus resulting in a total of 82176 cells. The maximum resulting y^+ value of the near-wall cells was 0.91 in the case of the reference grid, and 0.46 in the case of the refined grid. Hence, the wall boundary layers were sufficiently refined for the application of the used turbulence model.

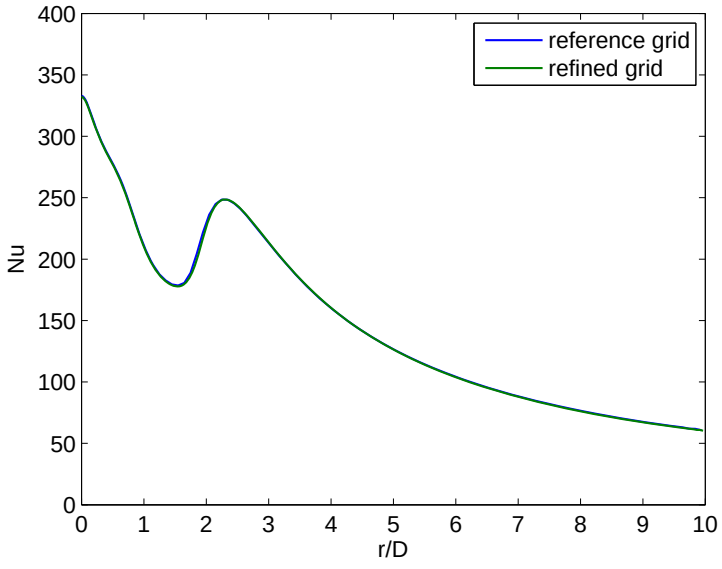

Fig. 5.15 Nusselt number distribution obtained with different grids for $Re = 70000$.

The Nusselt number distribution obtained with the reference grid is seen in Fig. 5.15 to be very close to that obtained with the refined grid. The maximum deviation is 2% at $r/D = 1.8$. The Nusselt number distribution obtained with the reference grid is therefore considered to be grid independent. The trend in the Nusselt number distributions

presented in Fig. 5.15 is similar to that observed for a jet Reynolds number of 23750. The peak Nusselt number is found at the stagnation point, while a secondary peak is observed at non-dimensional radius of $r/D = 2.3$. The secondary peak is however more pronounced in the case of $Re = 70000$ than for $Re = 23750$.

The Nusselt number distribution for $Re = 70000$ is compared to the experimental data of Yan et al. [67] in Fig. 5.16. Numerical results of Behnia et al. [48] are also included in the figure.

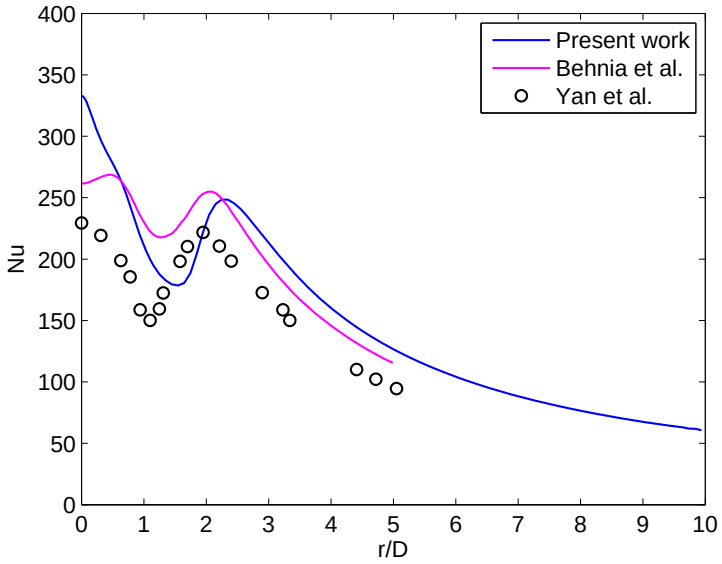

Fig. 5.16 Comparison of numerical and experimental Nusselt number distributions. Numerical results obtained in the present work for $Re = 70000$ vs. experimental data of Yan et al. [67] for $Re = 70000$. The numerical results of Behnia et al. [48] for $Re = 70000$ are also included in the figure.

Some difference is observed in Fig. 5.16 between the numerical results obtained in the present work and the experimental results of Yan et al. [67]. The Nusselt number distribution along the wall displays however a similar trend in the two cases. The distributions have a peak in the stagnation point and exhibit a secondary peak, as in the case of $Re = 23750$, after which the Nusselt number decreases monotonically. The locations of the secondary peak are however not coinciding as well as in the case of $Re = 23750$. A larger relative difference also exists between the Nusselt numbers obtained in the present work and those obtained experimentally than in the case of $Re = 23750$. The disagreement between the results is largest in the stagnation region, while a slightly better agreement is observed in the wall jet region. The disagreement was clearly also largest in the stagnation region for $Re = 23750$. The maximum relative difference between the Nusselt numbers obtained in the present work and those obtained by Yan et al. [67] is in the stagnation point, where it is 45%. A reason for the disagreement between the results may be a difference in the turbulence at the pipe exit as mentioned previously, but this was not checked as Yan et al. [67] did not provide information about this. However, the disagreement is most likely caused by inability of

the applied numerical model to predict the actual Nusselt number distribution accurately as also suggested in the case of $Re = 23750$. In the stagnation region, the numerical results of Behnia et al. [48] are observed to be in better agreement with the experimental data than the results of the present work with respect to the Nusselt number magnitude. However, the results of Behnia et al. exhibit a decrease in the Nusselt number when approaching the stagnation point, which is not found in the experimental data or in the results of the present work. The trend in the experimental Nusselt number distribution around the secondary peak is also better predicted by the results of the present work, although the location of the secondary peak is slightly better predicted by Behnia et al.. In the wall jet region, the results of Behnia et al. are in better agreement with the data of Yan et al. than the results of the present work. As in the case of $Re = 23750$, the reason for the difference between the numerical results in Fig. 5.16 is probably due to the application of two different versions of the V2F turbulence model.

In the comparisons of numerical and experimental results in Fig. 5.14 and Fig. 5.16 the predicted Nusselt number distribution along the wall was examined for two different jet Reynolds numbers. The variation of the predicted stagnation point Nusselt number, Nu_0, with jet Reynolds number is now investigated. The stagnation point Nusselt number and the jet Reynolds number have previously been reported to correlate according to eq. (5.6), see e.g. [71], [74], [44], [75].

$$Nu_0 \propto Re^{\gamma} \tag{5.6}$$

For a purely laminar stagnation point flow, Sibulkin [76] obtained a value of $\gamma = 0.5$ in a theoretical analysis. The variation of stagnation point Nusselt number with jet Reynolds number obtained in the performed numerical computations is presented in a log-log plot in Fig. 5.17. In addition to the numerical results for jet Reynolds numbers of 23750 and 70000, the stagnation point Nusselt number obtained for $Re = 50000$ is also included. The numerical result in the case of $Re = 50000$ has been checked for grid independency as well, which was obtained. Experimental data by Yan et al. [67] for jet Reynolds numbers of 23000, 50000 and 70000 are presented in the figure for comparison.

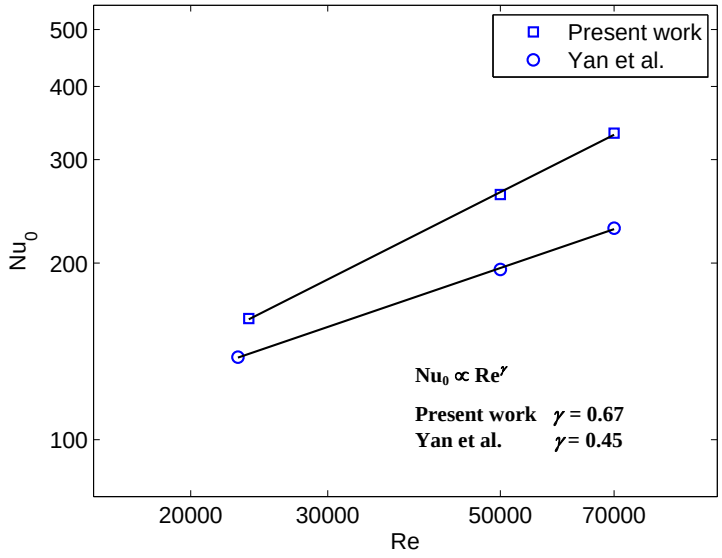

Fig. 5.17 Stagnation point Nusselt number vs. jet Reynolds number. Numerical results obtained in the present work vs. experimental data of Yan et al. [67].

Straight lines have been fitted to the data points in the log-log plot in Fig. 5.17. It is observed that the points fall closely onto the straight lines. The stagnation point Nusselt number and the jet Reynolds number are therefore well correlated by the relationship in eq. (5.6), in both the case of numerical data and experimental data. However, the value of the exponent γ differs in the two cases. For the numerical results, γ was found to be 0.67, whereas for the experimental results, γ was 0.45. Thus the applied numerical model seems to overpredict the variation in stagnation point Nusselt number with jet Reynolds number compared to the experimental results of Yan et al. [67]. This was also seen by the larger relative difference between the numerical and experimental results in Fig. 5.16 than in Fig. 5.14.

A major influential factor in the numerical prediction of jet impingement Nusselt numbers, especially in the stagnation region, is the turbulence modeling. In previous numerical studies the turbulence model has been shown to significantly influence the Nusselt number predictions, see e.g. [48], [50]. Hence, the disagreement between numerical and experimental results in Fig. 5.14 and Fig. 5.16 may primarily be attributed to the turbulence modeling. The V2F model applied in the present work has however been recommended in the literature as the preferred RANS type turbulence model for prediction of wall heat transfer in jet impingement configurations as mentioned in section 4.1. Therefore it was of interest to observe Nusselt number predictions obtained with other and commonly used RANS type eddy viscosity turbulence models and compare with the results based on the V2F model. Numerical computations for $Re = 23750$ and $Re = 70000$ were thus additionally performed with a low Re k-ε model [57] and a k-ε RNG model [58] employing wall functions. The model details are given in section 4.1.1.2 and in section 4.1.1.3. Like the V2F turbulence model, the low Re k-ε model requires a fine resolution of wall boundary layers, so the same grids were used as

in the case of the V2F model. Coarser grids were used with the k-ε RNG model due to the application of wall functions, which removed the need for finely resolved wall boundary layers. The Nusselt number distributions obtained for *Re* = 23750 are shown in Fig. 5.18 together with the previously presented experimental data. Results obtained for *Re* = 70000 are presented in Fig. 5.19 with the corresponding experimental data.

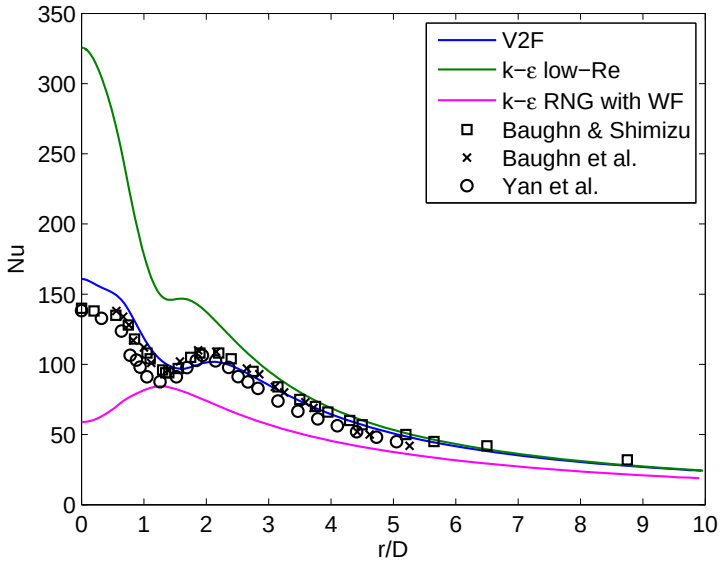

Fig. 5.18 Nusselt number distributions obtained with different turbulence models for *Re* = 23750. Experimental data of Baughn and Shimizu [39] for *Re* = 23750, Baughn et al. for *Re* = 23300 [40] and Yan et al. for *Re* = 23000 [67] are also shown.

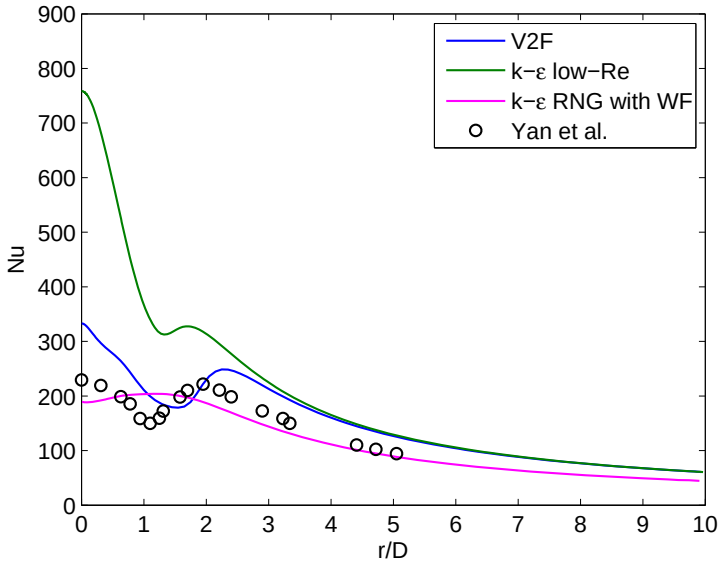

Fig. 5.19 Nusselt number distributions obtained with different turbulence models for *Re* = 70000. Experimental data of Yan et al. [67] for *Re* = 70000 are also shown.

The Nusselt number distributions obtained with the different turbulence models vary significantly for both Re = 23750 and Re = 70000. The trends in the experimental distributions are best predicted with the V2F model. The distributions obtained with the low Re k-ε model also show a peak in the stagnation point, and they exhibit a secondary peak around r/D = 1.65. However, a significant overprediction in the stagnation region is observed. The distributions obtained with the k-ε RNG model exhibit a wrong tendency in the stagnation region, where a local minimum appears in the stagnation point instead of a maximum as observed in the experiments. The erroneous behavior in the stagnation region supports the questioning of the validity of using wall functions in impinging flow regions mentioned by Behnia et al. [49]. In the far wall jet region all three turbulence models seem to capture the physics reasonably well, as the Nusselt number predictions in that region converge and seem to be in agreement with the experimental results. The results presented in Fig. 5.18 and Fig. 5.19 indicate the difficulty of handling impinging jet flows for turbulence models.

5.3 Summary

The performed comparison of numerical results obtained in the validation study and experimental results showed a good agreement between the predicted near-wall velocity field and the experimental measurements, especially in the wall jet region. This was the case for both Re = 23750 and Re = 70000. In the stagnation region some difference between the results was observed, which increased with the jet Reynolds number. The performed comparison also showed that the Nusselt number distribution was well predicted by the numerical model for Re = 23750 in both trend and magnitude. However, in the stagnation region some overprediction was observed. The maximum relative difference between numerical and experimental results was 15% and occurred in the stagnation point. For Re = 70000, the relative difference between the results increased, and in the stagnation point it was 45%. The predicted trend in the Nusselt number distribution agreed however with that in the experimental measurements, but the location of the secondary peak was shifted. The predicted variation in the stagnation point Nusselt number with jet Reynolds number was in good accordance with the expected relationship in eq. (5.6), but the variation was overpredicted compared to the experimental results.

The numerical model thus seems to predict the trends in velocity and wall heat transfer results correctly, but some overprediction in the heat transfer results apparently occurs. These observations are taken into account when analyzing and discussing the main results of the present work in the following chapters. The disagreement between numerical and experimental results is believed to be caused mainly by the turbulence modeling. The applied turbulence model is however considered to be the preferred RANS type model for the investigated flow case, and the application of other RANS type turbulence models also indicated significantly poorer predictions. More advanced turbulence modeling approaches were not tested in the present work due to time constraints. Another reason for the disagreement between the numerical and experimental results could be uncertainties in the experimental measurements. The uncertainty in the Nusselt number

values was however reported to be about 2.4%, 3% and 6%, in the studies of Baughn and Shimizu [39], Baughn et al. [40] and Yan et al. [67], respectively. The uncertainty in the Reynolds number was reported to be about 2.3%, 2% and 2% in [39], [40] and [67], respectively. Hence, measurement uncertainty is not able to explain the disagreement between the numerical and the experimental results.

6 Jet impingement heat transfer results

In this chapter results are presented from the performed simulations of the jet impingement process in the configuration described in section 3.1. The obtained wall heat flux distribution along the wall for the reference case, i.e. the case corresponding to the conditions in Table 3.1, is considered first. Subsequently, distributions are presented from a parameter variation study, where some of the parameters in Table 3.1 were varied in order to observe the influence of the parameter values on the resulting wall heat transfer. Results from the different investigated cases are then presented in dimensionless form in terms of the Nusselt number, the jet Reynolds number, and other dimensionless parameters in order to generalize the findings of the jet impingement heat transfer investigations.

6.1 Reference case

Obtained results for the investigated reference case are presented in this section. Before showing and discussing the obtained heat transfer results, the flow and temperature fields in the computational domain are however first visualized together with the mass fraction of the jet gas across the domain.

6.1.1 Flow and scalar fields

The flow pattern in the computational domain is indicated by streamlines in Fig. 6.1 and by velocity vectors in Fig. 6.2. Note that the vector distribution in Fig. 6.2 is based on a presentation grid. Thus, the actual cell distribution in the grid used in the computation cannot be inferred from this figure.

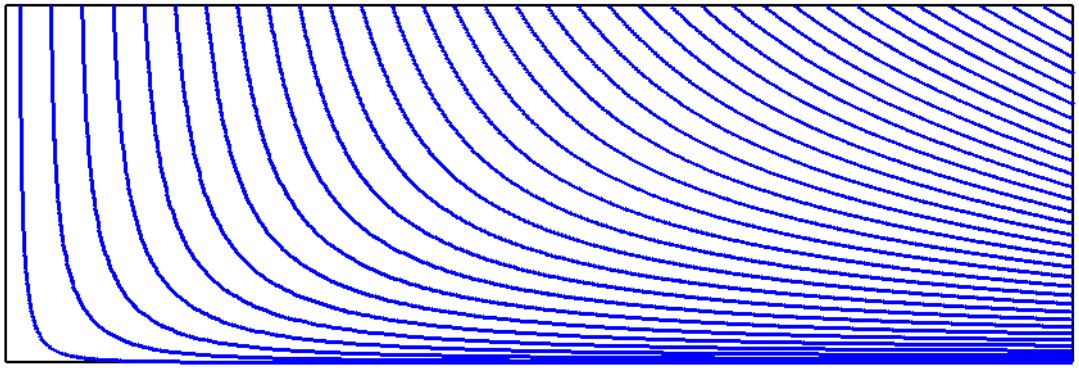

Fig. 6.1 Streamlines in the computational domain.

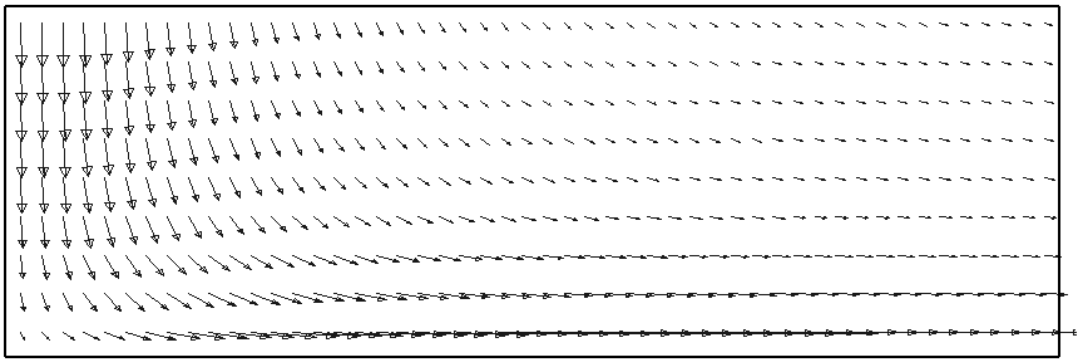

Fig. 6.2 Velocity field represented by velocity vectors on a presentation grid.

The jet flow enters the domain vertically and approaches the wall. Due to the presence of the wall, the jet flow is decelerated and gets deflected into an outward going direction parallel to the wall. It then first accelerates and later decelerates before leaving the domain at the right boundary. Ambient gas enters the domain along the upper pressure boundary due to the motion of the jet flow and is also deflected into an outward going direction and leaves the domain at the right boundary. The overall flow pattern in the domain is thus similar to that observed in validation case, where the jet issued from a pipe, see section 5.2.1. However, as there is no pipe wall present in the reference case, there is no recirculation zone next to the jet where it enters the domain. Along the wall, the jet flow turns into a decelerating wall jet due to wall friction and momentum exchange with the ambient gas as in the validation case. The formation of the wall jet is indicated in Fig. 6.3, which shows velocity vectors in the computational domain with focus on the wall jet region. The vector distribution in Fig. 6.3 is based on a presentation grid. Based on the velocity field in Fig. 6.3, it may seem as if the velocity does not meet the no-slip condition at the wall. However, a close-up of the region next to the wall confirmed that the no-slip condition at the wall is satisfied.

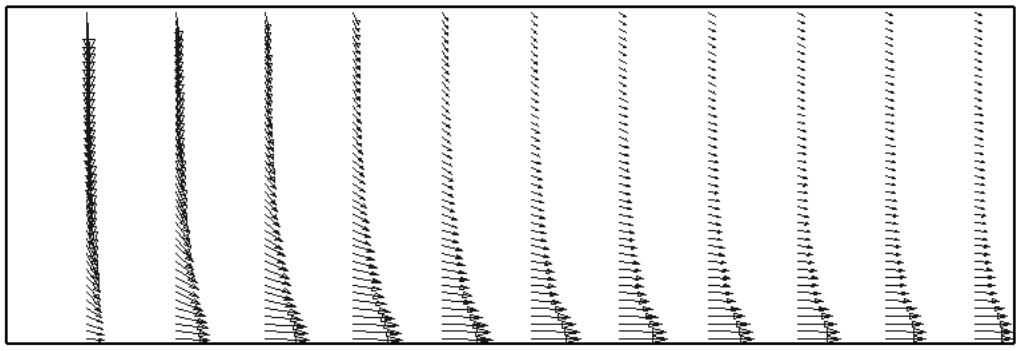

Fig. 6.3 Wall jet development. The presented velocity field is based on a presentation grid.

The velocity magnitude distribution in the computational domain is presented in Fig. 6.4. The deceleration of the jet flow when approaching the wall is clearly visible as well as the subsequent acceleration after the deflection of the jet flow into the outward going direction. The later deceleration along the wall is also visible.

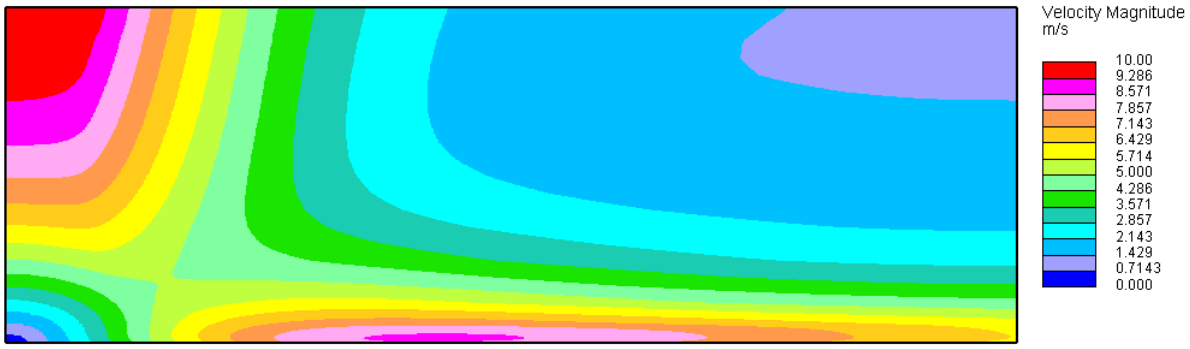

Fig. 6.4 Velocity magnitude in the computational domain.

The distribution of the jet gas across the computational domain is depicted in Fig. 6.5. The figure shows the mass fraction of the jet gas (in kg/kg). The mass diffusivity was $D_m = 3 \cdot 10^{-5}$ m^2/s, which resulted in a Schmidt number of $Sc = 0.10$. Close to the wall, the Schmidt number decreased down to about $Sc = 0.01$ due to a higher gas density and a lower viscosity in the near-wall region caused by a lower gas temperature. The turbulent Schmidt number was $Sc_t = 0.9$.

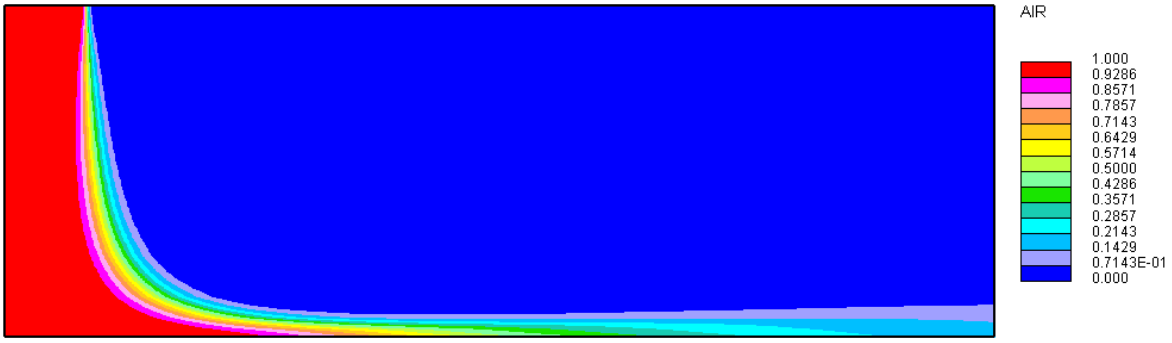

Fig. 6.5 Mass fraction of jet gas across the computational domain.

It is observed in Fig. 6.5 that the ambient gas does not penetrate through the jet into the stagnation region due to the short distance between the jet inlet and the wall relative to the jet diameter. A high degree of mixing of ambient gas and jet gas is however seen in the wall jet region.

The temperature field in the computational domain is presented in Fig. 6.6. It is noticed that the thermal boundary layer is very thin and almost not visible in Fig. 6.6. A close-up of the temperature field in the stagnation region is presented in Fig. 6.7, where the

stagnation point is located in the lower left corner. Using the definition of the thermal boundary layer thickness given in section 5.2.1, the thickness in the stagnation region is found be δ_t = 3.1 mm. Thus, the gas temperature exhibits a change of almost 1600K over a distance of 3.1 mm in the stagnation region.

Fig. 6.6 Temperature field in the computational domain.

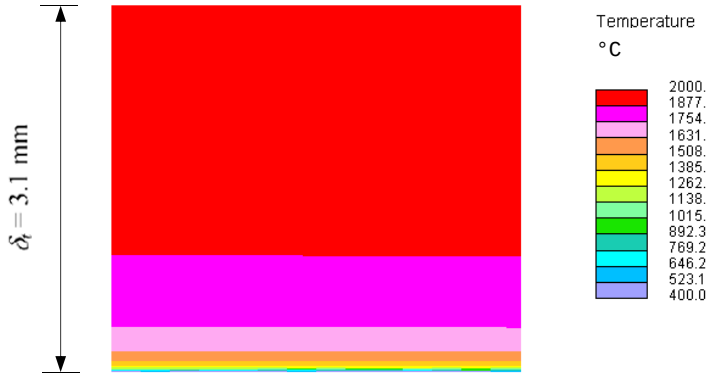

Fig. 6.7 Close-up of the temperature field in the stagnation region.

6.1.2 Heat flux distribution

The heat flux distribution along the wall obtained for the investigated reference case is presented in Fig. 6.8.

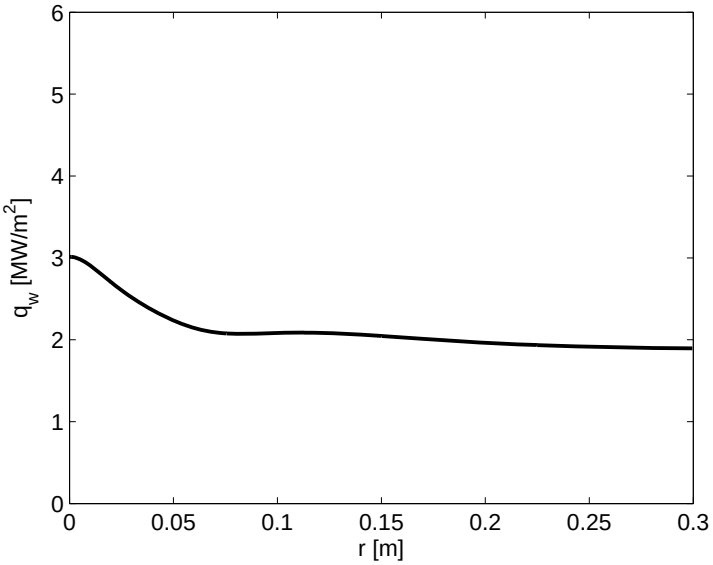

Fig. 6.8 Wall heat flux distribution for the reference case.

The predicted wall heat flux distribution reaches a peak value of 3.01 MW/m^2 in the stagnation point. The heat flux decreases along the wall with increasing radial distance until r = 0.08 m, where a relatively weak local minimum is reached. A secondary peak in the wall heat flux is observed at r = 0.11 m after which the heat flux decreases monotonically. The location of the secondary peak corresponds to a dimensionless radial distance of r/D = 2.2. Hence, the observed secondary peak occurs close to the location reported for the secondary peak in previous jet impingement heat transfer studies, e.g. [39], [70], [38]. In these studies the location of the secondary peak varied between r/D = 2.0 and r/D = 2.3 as mentioned in section 5.2.3.

6.1.3 Grid independency

The heat flux distribution presented in Fig. 6.8 was checked for grid independency by performing computations on three consecutively refined grids with 600×38 cells, 1200×90 cells and 2400×180 cells in the horizontal and vertical directions, respectively. No grid refinement was performed in the azimuthal direction due to the two-dimensionality assumption of the flow field invoked in the simulations. The resulting heat flux distributions are presented in Fig. 6.9. The distribution in Fig. 6.8 was obtained with the reference grid consisting of 1200×90 cells.

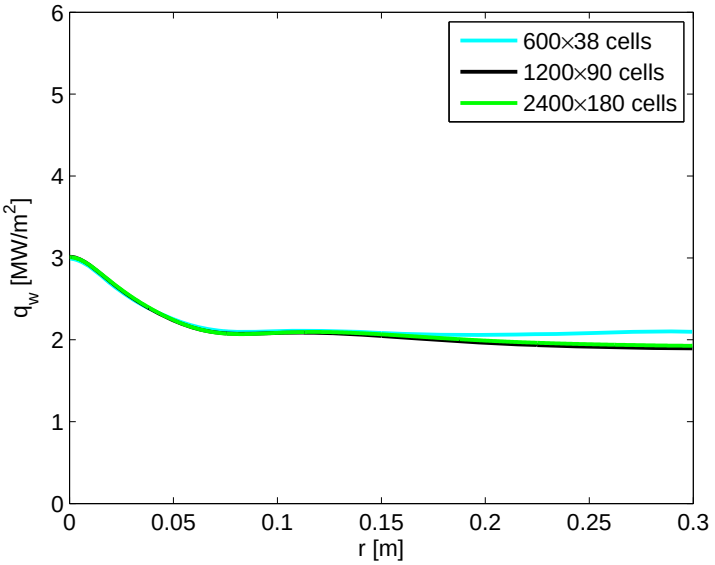

Fig. 6.9 Wall heat flux distributions obtained with three consecutively refined grids.

The maximum relative difference between the heat flux distributions obtained with the coarsest grid (600×38 cells) and the finest grid (2400×180 cells) is 9.1%, while the maximum relative difference is 1.7% between the distributions obtained with the medium refined grid (1200×90 cells) and the finest grid. The largest relative differences between the distributions are observed in the outer wall jet region. For a radial distance of $r < 0.1$ m, all three curves nearly coincide with a relative difference between the distributions of less than 1.4%. Based on these results, the grid consisting of 1200×90 cells was considered to provide sufficient resolution of the computational domain. The highest value of the dimensionless wall distance y^+ of the near-wall cells was observed to 0.12 using this grid. The grid thus provided sufficient resolution of the wall boundary layer for the applied turbulence model, which required $y^+ < 1$ [59]. In all investigations reported in subsequent sections, this grid was used unless otherwise stated.

6.1.4 Influence of domain size

The influence on the wall heat flux distribution of the location of the vertical pressure boundary in the numerical setup (see Fig. 4.1) was investigated by varying the horizontal extent of the computational domain. Three cases were investigated in which the radial extent of the computational domain was 0.20 m, 0.30 m and 0.50 m, respectively. The cell density in all three grids was the same. Hence, the grid resolution in the case of a radial extent of 0.20 m, 0.30 m and 0.50 m was 800×90, 1200×90 and 2000×90, respectively. The wall heat flux distributions obtained with the different grids are presented in Fig. 6.10.

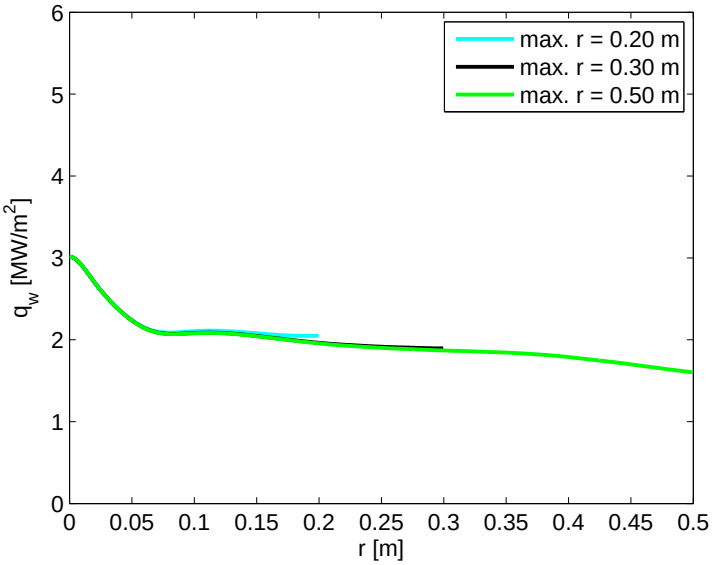

Fig. 6.10 Wall heat flux distributions obtained with grids of different radial extent.

Extending the domain in radial direction did not influence the wall heat flux distribution significantly. For the cases of a radial domain extent of 0.20 m and 0.50 m, the maximum relative difference between the obtained distributions is 4.9%. For the cases of a radial domain extent of 0.30 m and 0.50 m, it is 1.4%. In the stagnation region all three heat flux distributions nearly coincide. Based on this, the domain with a radial extent of 0.30 m was considered to be sufficient for the present work. It has previously been reported [48] that for jet impingement configurations where a jet issued from a pipe, the location of the vertical pressure boundary had no noticeable influence on the flow field and wall heat transfer results once the location was larger than $r/D = 8 + H/D$ with H being the distance between the pipe exit and the impingement wall and D the pipe diameter. This corresponds to $r/D = 10$ or $r = 0.50$ m in the present case, if the ratio between the jet inlet to wall distance and the jet diameter at the inlet is used as the H/D ratio. The result of the present horizontal domain extension study thus agrees with that reported in [48]. The influence of moving the upper pressure boundary further away from the wall was not investigated. The reason was that the upper pressure boundary needed to be in the same height as the jet inlet boundary, because there was no wall between the incoming jet and the ambient gas in the considered jet impingement configuration. An increase in the distance between the wall and the upper pressure boundary would probably to some degree influence the wall heat transfer results.

6.2 Parameter variations

Computations were performed where some of the configuration parameters listed in Table 3.1 were varied in order to observe the resulting influence on the wall heat flux. It was relevant to study the effect of parameter variations on the heat transfer results because the reference values listed in Table 3.1 were subject to uncertainty in terms of

representing the actual conditions during combustion in large marine diesel engines. The parameters which were varied were the ambient gas temperature, the pressure, the jet velocity at inlet, the wall temperature and the jet turbulence intensity at inlet.

6.2.1 Variation of ambient gas temperature

The influence of the ambient gas temperature on the wall heat flux was investigated. In the reference case, the temperature of the ambient gas was 2000°C and thus equaled the jet temperature at the inlet, cf. Table 3.1. However, the temperature of the gas in the considered engines outside the zones where combustion products are present is likely to be lower than 2000°C as mentioned in section 3.1. For the engine, on which the values in Table 3.1 are based, the temperature is expected to be between 600°C and 2000°C. The temperature of 600°C is the estimated lower value for the compression temperature in the engine, i.e. the gas temperature at the end of the compression when the piston is at TDC and before combustion. Calculations were therefore performed where the temperature of the incoming gas at the upper pressure boundary in the numerical setup, T_a, was varied between 600°C and 2000°C. The values of all other configuration parameters were the same as in the reference case. The resulting heat flux distributions along the wall are presented in Fig. 6.11.

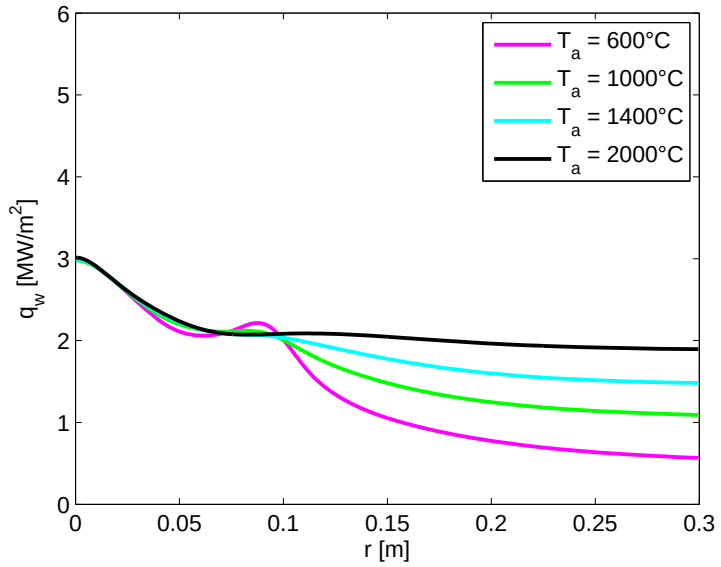

Fig. 6.11 Wall heat flux distributions for different ambient gas inflow temperatures.

For radial distances of $r > 0.10$ m, the wall heat flux clearly decreases with decreasing ambient gas inflow temperature. The influence is due to mixing of colder gas into the wall jet, which decreases the temperature of the gas next to the wall and thereby the wall heat flux. For the case of an ambient gas inflow temperature of 600°C, the wall heat flux varies from 2.99 MW/m^2 at the stagnation point to 0.57 MW/m^2 at $r = 0.30$ m. This is in contrast to the case where the ambient gas inflow temperature equaled the jet inlet

temperature, i.e. 2000°C. In this case the heat flux decreases to 2.07 MW/m^2 at $r = 0.08$ m and only decreases a little further at larger radial positions. In the stagnation region however, the wall heat flux is almost unaffected by the change in ambient gas inflow temperature. This is due to insignificant entrainment of colder ambient gas into the warm jet caused by the relative short distance between jet inlet and wall. Thus, the peak heat flux occurs in the stagnation point for all the cases investigated and is practically uninfluenced by the change in ambient gas inflow temperature. The temperature field in the case of an ambient gas inflow temperature of 600°C is shown in Fig. 6.12. It is observed that the gas temperature in the stagnation region is about the same temperature as the jet temperature at the inlet although the ambient gas has a significantly lower temperature than the incoming gas at the jet inlet. This is due to the short distance between jet inlet and wall, which prevents entrainment of colder ambient gas into the stagnation region as noted above.

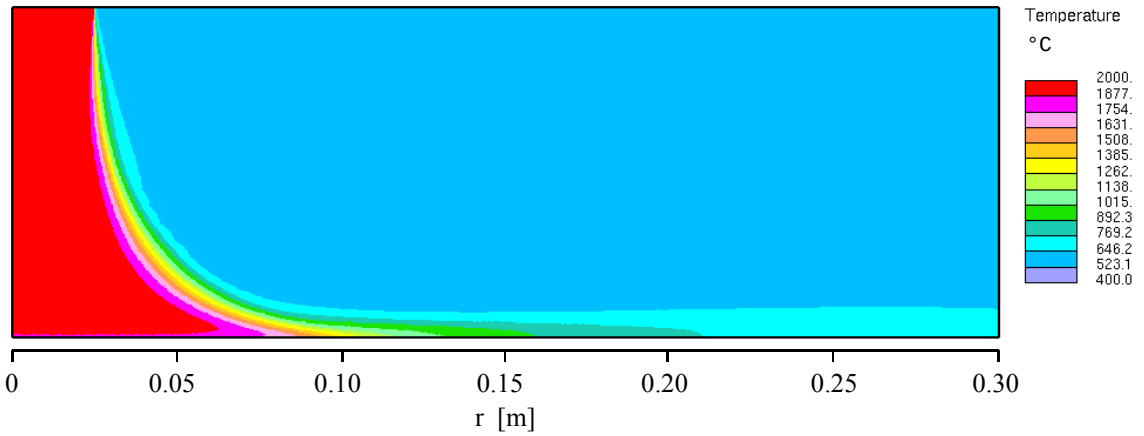

Fig. 6.12 Temperature field in the case of an ambient gas inflow temperature of 600°C.

It became more difficult to reach convergence in the computations when the ambient gas inflow temperature decreased, i.e. the number of iterations needed before convergence was obtained increased. This is assumed to be caused by the increased computational effort needed to calculate the heat exchange between the hot and the cold gas. The ambient gas inflow temperature was therefore kept equal to the jet inlet temperature in the investigations of the influence of the other configuration parameters on the wall heat flux.

6.2.2 Variation of pressure

In the reference case, the domain pressure was 180 bar, which is the estimated level of the maximum pressure during combustion in the engine on which the values in Table 3.1 are based. However, the pressure in the engine at the time of impingement of combustion products on the piston surface might be lower than 180 bar depending on when in the combustion phase the gasses reach the piston surface. In order to investigate the influence

of the cylinder pressure on the wall heat flux, three different pressure levels were considered in the computations: 180 bar, 150 bar and 120 bar. Imposing these three pressure levels in the computation resulted in the heat flux distributions presented in Fig. 6.13. In the calculations with a pressure of 150 bar and 120 bar, polynomial expressions were applied for the temperature dependency of the thermophysical properties, c_p, λ and μ, and the density ρ, which were derived for the corresponding pressures, based on data in [63]. The main influence of the change in pressure was on the density since the thermophysical properties, c_p, λ and μ, varied less than 4% when changing the pressure from 180 bar to 120 bar. The density, however, decreased about 33%.

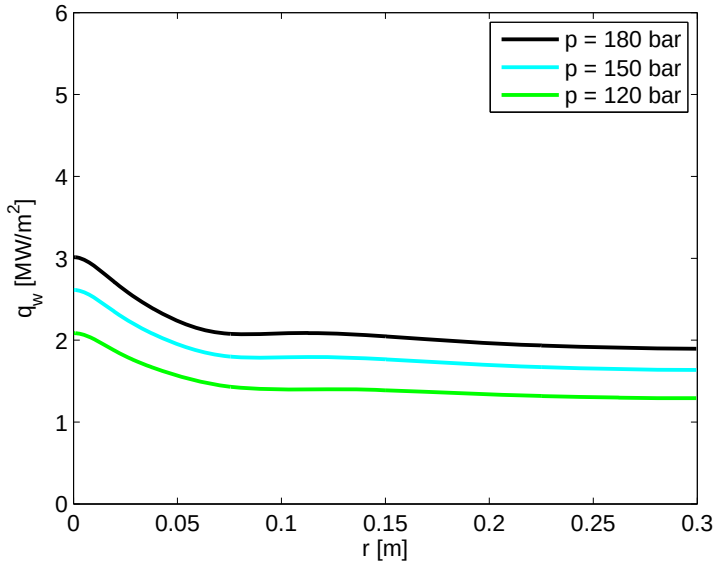

Fig. 6.13 Wall heat flux distributions obtained at different pressure levels.

In the case of a pressure of 180 bar, the heat flux along the wall varies between 3.01 MW/m^2 and 1.90 MW/m^2, while it varies between 2.09 MW/m^2 and 1.29 MW/m^2 in the case of 120 bar. The decrease in pressure decreases the wall heat flux nearly uniformly for all radial distances. The average decrease in heat flux is 14% when lowering the pressure from 180 bar to 150 bar, i.e. a decrease in pressure of 17%. Lowering the pressure further from 150 bar to 120 bar, a change of 20 %, decreases the heat flux 21% in average. Changing the pressure from 180 bar to 120 bar, i.e. 33%, results in a heat flux decrease of 32% in average. Thus, the average relative decrease in wall heat flux is approximately equal to the relative decrease in pressure.

6.2.3 Variation of jet velocity at inlet

The jet velocity at the inlet was specified to 10 m/s in the reference case, cf. section 3.1. This is the estimated velocity magnitude of the impinging combustion products at a distance of 0.10 m from the piston surface. However, velocities in the considered engines during combustion are difficult to estimate, and the value of 10 m/s is a rough

approximation. Therefore, in order to investigate the influence of velocity on the wall heat flux, the jet velocity at the inlet was varied between 10 m/s and 40 m/s in the numerical setup while keeping the other configuration parameters unchanged. The resulting heat flux distributions are presented in Fig. 6.14.

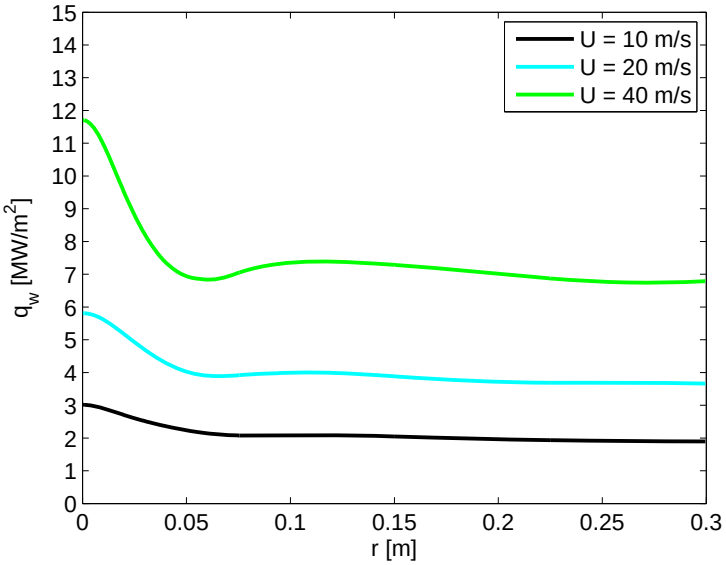

Fig. 6.14 Wall heat flux distributions for different jet velocities at the inlet.

The jet velocity is observed to have a significant influence on the wall heat flux, mainly on the heat flux magnitude but also on the distribution. In the case of a velocity of 40 m/s, the peak heat flux reaches 11.7 MW/m^2, while the peak heat fluxes are 5.81 MW/m^2 and 3.01 MW/m^2 in the cases of 20 m/s and 10 m/s, respectively. In all cases, the peak heat flux occurs in the stagnation point. The average relative increase in the heat flux values is between 83% and 90% of the relative increase in the jet velocity.

6.2.4 Variation of wall temperature

The temperature of the wall in the jet impingement reference configuration was 400°C, which was based on cycle mean temperature measurements in the piston crown of the large marine diesel engine on which the values in Table 3.1 are based. The measurements were obtained approximately 5 millimeters below the piston surface, as mentioned in section 3.1, and indicated a temperature level of 400°C. As the measurements were not performed at the piston surface, and as they only provided cycle mean values, the actual piston surface temperature at the time of impingement of combustion products may be higher than 400°C. A variation of the wall temperature in the numerical computations was therefore performed in order to investigate the influence of the wall temperature on the resulting wall heat flux. The wall temperature was varied between 400°C and 1000°C, and the corresponding wall heat flux distributions are shown in Fig. 6.15.

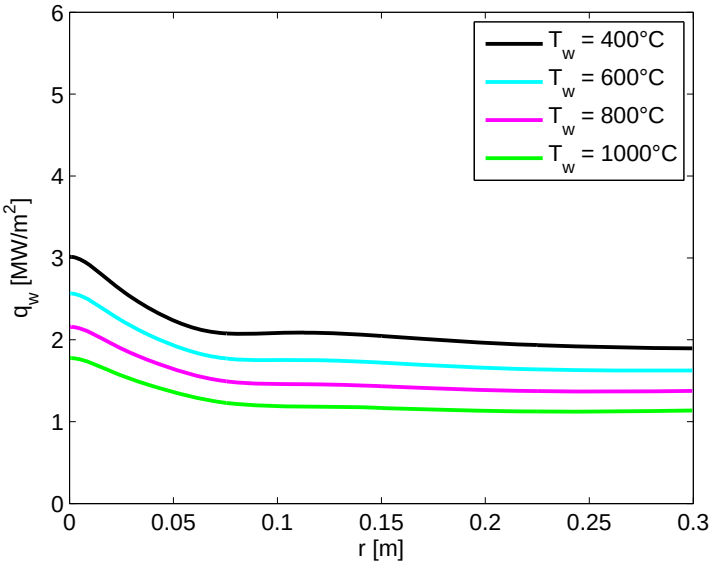

Fig. 6.15 Wall heat flux distribution for different wall temperatures.

An increase in the wall temperature resulted in a nearly uniform decrease in the wall heat flux for all radial positions as observed in Fig. 6.15 . In the case of a wall temperature of 1000°C, the heat flux is between 1.78 MW/m^2 and 1.14 MW/m^2, while it is between 3.01 MW/m^2 and 1.90 MW/m^2 in the case of a temperature of 400°C. In average, the wall heat flux decreases about 0.29 MW/m^2 for every increase of 200K in the wall temperature.

6.2.5 Variation of jet turbulence intensity at inlet

In the reference case, the jet turbulence intensity at the inlet *TI* was 5%. However, this value was based on jet impingement studies where the jet issued from a pipe. The turbulence intensity in the impinging jet of combustion products in the considered engines during combustion was not known, but the intensity may be higher than 5% as mentioned in section 3.1. A variation of the jet turbulence intensity at the inlet was therefore performed to investigate the influence of turbulence on the wall heat transfer. The intensity was varied from 1.5% to 10%, and the resulting wall heat flux distributions are presented in Fig. 6.16.

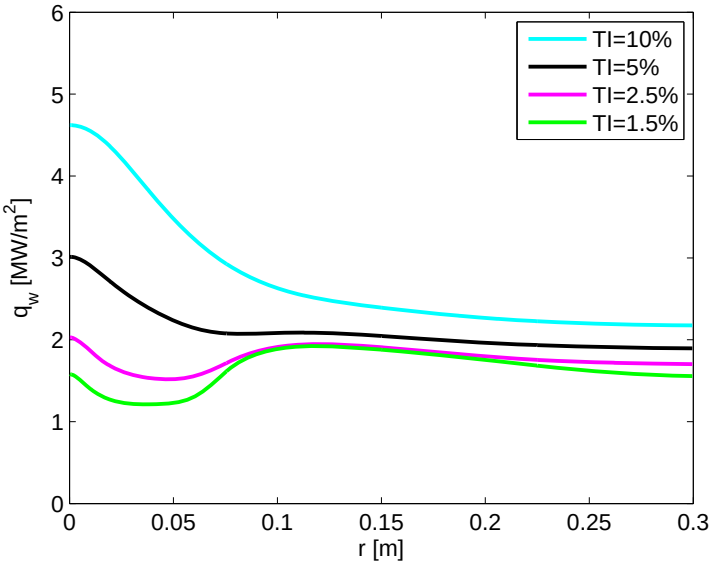

Fig. 6.16 Wall heat flux distributions for different jet turbulence intensities at the inlet.

It is observed that the jet turbulence intensity at the inlet has a significant influence on the wall heat flux. The maximum heat flux is 1.92 MW/m^2 in the case of TI = 1.5%, while it reaches a value of 4.62 MW/m^2 in the case of TI = 10%. A secondary peak in the heat flux distribution is clearly observed at r = 0.12 m for low turbulence intensities, i.e. for TI = 1.5% and TI = 2.5%. For TI = 5%, a secondary peak is also observed although it is weak. The location of the secondary peak is at r = 0.11 m as mentioned in section 6.1. For TI = 10%, the wall heat flux decreases monotonically from the stagnation point without the occurrence of a secondary peak. In the case of TI = 1.5%, the maximum heat flux occurs at the secondary peak, whereas for the other cases it is located at the stagnation point. The locations of the secondary peaks observed in the wall heat flux distributions correspond to dimensionless radial distances of r/D = 2.2 and r/D = 2.4. The locations are thus in accordance with the location of the secondary peak reported in previous experimental works on jet impingement heat transfer, [39], [70], [38], in which the location is reported to be between r/D = 2.0 and r/D = 2.3 as noted in section 6.1 and section 5.2.3.

6.3 Modification of the numerical modeling

The influence on the wall heat flux of changing the values of physical parameters in the jet impingement configuration was investigated in the parameter variation study presented above. The effect on the wall heat flux of modifying the numerical setup with respect to the turbulence modeling was also investigated. The results are presented below.

6.3.1 Influence of turbulence model

During the validation study of the numerical modeling it was observed that the turbulence model had a significant influence on the predicted wall heat transfer, especially in the stagnation region. It was therefore of interest to observe the variation in the predicted wall heat flux in the investigated jet impingement configuration when applying different turbulence models. Besides the performed calculations applying the V2F model, calculations were performed with the two other turbulence models used in the validation study and described in [59]: a low-Re k-ε model [57] and a k-ε RNG model [58] employing wall functions. The first model required a resolved wall boundary layer, while the last model was less computational demanding due to the application of wall functions. The low-Re k-ε model was applied on the same grid as that used for the V2F turbulence model (1200×90 cells). The k-ε RNG model with wall functions was applied on a much coarser grid consisting of 120×35 cells in the horizontal and vertical direction, respectively, without a full resolution of the wall boundary layer. Therefore, in the case of the k-ε RNG model, y^+ values of the near-wall cells were between 38 and 77. The computation times showed that the calculations using the k-ε RNG model obtained convergence two orders of magnitude faster than the calculations using the other models. The obtained heat transfer results are presented in Fig. 6.17.

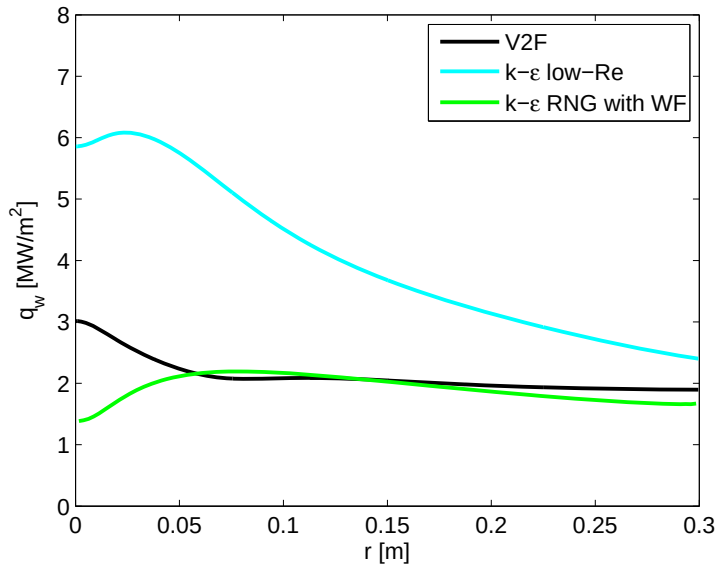

Fig. 6.17 Wall heat flux distributions obtained using different turbulence models.

The application of the different turbulence models is seen to result in a large variation of the predicted wall heat flux, both in magnitude and trend. This was also observed in the validation study. The predictions obtained using the V2F model are first decaying until $r = 0.08$ m, whereafter a local maximum is seen at $r = 0.11$ m as noted previously. The global maximum is at the stagnation point. For the two other models, the heat flux predictions show a minimum at the stagnation point, while the global maximum is at $r = 0.02$ m and $r = 0.08$ m, respectively, in contrast to the V2F predictions. The

magnitude of the wall heat flux differs also markedly between the different model predictions, especially in the stagnation region. Most pronounced were the low-Re k-ε model predictions, which in the stagnation point resulted in a heat flux of 5.86 MW/m^2. This is 95% higher than the V2F model prediction of 3.01 MW/m^2 in the stagnation point. Also the stagnation point heat flux predicted by the k-ε RNG model, 1.39 MW/m^2, deviated significantly from the V2F model result by -54%. The predicted heat flux levels obtained by using the V2F model and the k-ε RNG model however agree in the wall jet region. The results in Fig. 6.17 emphasize the problem of handling jet impingement flows for the turbulence models, especially in the stagnation region, which was also noticed in the validation study. As previously mentioned, no experimental wall heat transfer data were found for the conditions in the jet impingement reference case, so a comparison of the numerical results to experimental measurements was not possible. However, except for the tendency in the stagnation region heat flux results predicted by the low-Re k-ε model, the tendencies in the different heat flux distributions in Fig. 6.17 are in general similar to those observed in Fig. 5.18 and Fig. 5.19. Therefore, of the three turbulence models examined, the V2F model is considered to provide the most accurate predictions for the investigated jet impingement case.

6.4 Presentation of results in dimensionless form

The obtained jet impingement heat transfer results will be presented in dimensionless form in this section. Presentation of results in dimensionless form is valuable because it allows a generalization of the results, so they can be used in situations with different dimensional parameter values as long as the dimensionless parameter values are equal in the different situations. The dimensionless parameter describing the heat transfer to the wall is the Nusselt number *Nu*. For the investigated jet impingement configuration, the local Nusselt number is assumed to be given by eq. (6.1), which is based on the analysis presented in Appendix A:

$$Nu = f(\frac{r}{D}, \frac{H}{D}, Re, Pr, Tu, \Delta T_{aj}{}^{*}, f_{\mu^*}, f_{c_p{}^*}, f_{\lambda^*}, f_{\rho^*}) \tag{6.1}$$

The Reynolds number *Re* and the Nusselt number *Nu* in eq. (6.1) are defined as:

$$Re = \frac{\rho U D}{\mu} \tag{6.2}$$

$$Nu = \frac{hD}{\lambda} \tag{6.3}$$

where the characteristic length is the jet diameter at the inlet *D*, indicated in Fig. 3.1, and the characteristic velocity is the velocity of the jet at the inlet *U*. The heat transfer coefficient *h* is given by eq. (5.4), which is repeated here for simplicity:

$$q_w = h(T_j - T_w) \tag{6.4}$$

The Prandtl number *Pr* is defined in eq. (1.2), which is also repeated for simplicity:

$$Pr = \frac{c_p \mu}{\lambda} \tag{6.5}$$

The parameter *Tu* represents the influence on the Nusselt number of the jet turbulence at the inlet. $\Delta T_{aj}{}^*$ represents the influence on the Nusselt number of the difference between the ambient gas inflow temperature T_a and the jet temperature at the inlet T_j. $\Delta T_{aj}{}^*$ is defined as:

$$\Delta T_{aj}{}^* = \frac{T_j - T_a}{T_j - T_w} \tag{6.6}$$

In eq. (6.1), $f_{\mu^*}, f_{c_p{}^*}, f_{\lambda^*}$ and f_{ρ^*} represent the functions relating the thermophysical properties μ, c_p and λ and the density ρ to the temperature and the pressure, i.e. state relations, all in dimensionless form. The inclusion of these relations in eq. (6.1) is a consequence of the varying thermophysical properties and density in the jet impingement configuration. If the thermophysical properties and density are not constant then not only the dimensionless parameters but also the dimensionless state relations in different heat transfer cases need to be equal in order to obtain equal Nusselt numbers, as demonstrated in Appendix A and noted by White [77] and by Eckert and Drake [78]. In cases with varying properties and density, Nusselt number expressions obtained in cases with constant (or nearly constant) properties and density are however often used by simply multiplying the expression for the Nusselt number by a correction factor [79], [25]. For problems involving gasses, the correction factor *CF* is typically of the form:

$$CF_T = \left(\frac{T_\infty}{T_s}\right)^\beta \tag{6.7}$$

or

$$CF_{Pr} = \left(\frac{Pr_\infty}{Pr_s}\right)^\beta \tag{6.8}$$

where ∞ denotes free stream conditions, *s* denotes surface conditions, and β is an empirically or sometimes analytically determined exponent. At the same time, the thermophysical properties and density appearing in the dimensionless parameters in the expression for the Nusselt number are evaluated at the free stream temperature, and likewise for the conductivity in the Nusselt number. Another approach, also applied in cases with varying properties and density, is simply to evaluate the thermophysical properties and density in the constant-property-and-density expression for the Nusselt number at the film temperature T_f, and likewise for the conductivity in the Nusselt number. The film temperature T_f is defined as [25]:

$$T_f = \frac{T_\infty + T_s}{2} \tag{6.9}$$

However, in cases where the thermophysical properties and density vary substantially, these correction approaches may not be adequate [79], and a Nusselt number expression valid for both constant and varying property and density cases may not be possible to obtain [78].

Due to the turbulence model applied in the present numerical work, the jet turbulence at the inlet was described by a turbulence intensity *TI* and a turbulence length scale *L*. Therefore, for the present work, the parameter *Tu* in eq. (6.1) is split into two parameters, a turbulence intensity *TI* and a dimensionless turbulence length scale *TL* = *L*/*D*, and eq. (6.1) is reformulated to:

$$Nu = f(\frac{r}{D}, \frac{H}{D}, Re, Pr, TI, TL, {\Delta T_{aj}}^*, f_{\mu^*}, f_{{c_p}^*}, f_{\lambda^*}, f_{\rho^*}) \tag{6.10}$$

With respect to the dimensionless state relations $f_{\mu^*}, f_{{c_p}^*}, f_{\lambda^*}$ and f_{ρ^*}, it is assumed that the influence on the Nusselt number of differences in these between the different investigated jet impingement cases is small and can be neglected. Thereby eq. (6.10) reduces to:

$$Nu = f(\frac{r}{D}, \frac{H}{D}, Re, Pr, TI, TL, {\Delta T_{aj}}^*) \tag{6.11}$$

The thermophysical properties c_p, λ and μ and the density ρ varied significantly in the investigated jet impingement configuration due to the large temperature difference between the inlet and the wall. In the reference case, the temperature difference was 1600K and caused c_p to vary by 24%, μ by 124% and λ by 187%, while the density varied by 236%. The values of *Nu*, *Re* and *Pr* will therefore depend on which temperature in the configuration is used for the evaluation of the thermophysical properties and density in the dimensionless parameters. Hence, it is important to consider at which temperature the properties and density should be evaluated. As the characteristic length and velocity used in the Reynolds number are the jet diameter at the inlet *D* and the jet velocity at the inlet *U*, it seems natural to choose the jet temperature at the inlet T_j for the evaluation of the thermophysical properties and density in *Re* and *Pr*. The Reynolds number will then also characterize the jet flow entering the computational domain at the inlet. Thus, the jet temperature at the inlet T_j is used for the evaluation of the properties and the density in *Re* and *Pr*, which are then given by eq. (6.12) and eq. (6.13), respectively, where index *j* denotes evaluation at T_j.

$$Re_j = \frac{\rho_j U D}{\mu_j} \tag{6.12}$$

$$Pr_j = \frac{c_{p,j}\mu_j}{\lambda_j} \tag{6.13}$$

The Reynolds number in eq. (6.12) can be considered as a jet Reynolds number and will be termed so below. For simplicity, it will still be denoted by *Re*, i.e. without index *j*. The Prandtl number will also simply be denoted by *Pr*. The thermal conductivity in the Nusselt number is evaluated at the same temperature as the thermophysical properties and the density in *Re* and *Pr*, i.e. at the jet temperature at the inlet T_j. A different temperature might be used, but then the ratio between the conductivities evaluated at this other temperature and at T_j should also be included as a dimensionless parameter on the right hand side of eq. (6.11) according to the analysis in Appendix A. The Nusselt number is therefore calculated as:

$$Nu_j = \frac{hD}{\lambda_j} \tag{6.14}$$

As with the Reynolds and Prandtl numbers, the Nusselt number will simply be denoted by *Nu* below without index *j*.

The choice of the jet temperature at the inlet as the reference temperature for the evaluation of the thermal conductivity in the Nusselt number is appropriate according to findings in the work of Shi et al. [80], [81]. They performed numerical studies, using a CFD code, on jet impingement heat transfer at both small and large differences between the jet temperature and the wall temperature. They investigated the influence of applying different reference temperatures for the evaluation of the conductivity in the Nusselt number on the spreading between Nusselt number distributions obtained for different temperature differences between jet and wall. The applied reference temperatures were the jet temperature, the wall temperature and the film temperature, calculated as the arithmetic mean of the jet and wall temperatures. For round jets, they investigated cases with Reynolds numbers of 5000 and 15000 and $H/D = 3$. The temperature differences were 10K, 50K, 100K and 200K. For slot jets, cases with Reynolds numbers of 1500, 3000, 6000 and 12000 were studied with $H/W = 2.6$, 6 and 12 in each case (W is the slot jet width). The temperature differences were 12K and 272K. Shi et al. [81] concluded that the most suitable temperature for the evaluation of the thermal conductivity in *Nu* was the jet temperature for slot jets, as this gave the least spread in *Nu* distributions along the wall for different jet-wall temperature differences. For round jets, Shi et al. [80] found that both the jet temperature and the film temperature would be suitable, but they recommended using the film temperature as that is already commonly applied. In their studies, Shi et al. [80], [81] did not explicitly state which temperature they used for the evaluation of the viscosity and density in the Reynolds number. However, the Reynolds number is referred to as the jet Reynolds number, so they probably based the Reynolds number on the jet diameter and velocity at the inlet and evaluated the viscosity and density in the Reynolds number at the jet temperature at the inlet. Unfortunately, Shi et al. [80], [81] did not present any theoretical considerations on which reference temperature would be most appropriate for the evaluation of the thermal conductivity in

the Nusselt number. Apparently, they based their recommendations purely on the obtained numerical results, where the Nusselt numbers calculated with the use of different reference temperatures were simply compared to each other.

The performed variations of the different dimensional configuration parameters influenced directly the values of the dimensionless parameters on the right hand side of eq. (6.11). The variations of the jet velocity at the inlet U and the pressure p influenced Re, while the variations of the ambient gas inflow temperature T_a influenced $\Delta T_{aj}{}^*$. The variations of the wall temperature T_w would also influence $\Delta T_{aj}{}^*$ according to eq. (6.6) but only in cases where $T_j \neq T_a$ as $\Delta T_{aj}{}^*$ otherwise would be zero. The variations of the wall temperature were however all performed for $T_a = T_j$. The jet turbulence intensity at the inlet TI was varied directly, whereas the ratio H/D and the dimensionless turbulence length scale TL were not varied in the investigations. The performed parameter variations did not influence Pr, which was the same in all the investigated cases. An overview of the resulting variations of the dimensionless parameters on the right hand side of eq. (6.11) for the performed computations is presented in Table 6.1.

Dimensionless parameter	Range
H/D	2
Re	$1.10 \cdot 10^5 – 6.64 \cdot 10^5$
Pr	0.67
TI	0.015 – 0.100
TL	0.07
$\Delta T_{aj}{}^*$	0 – 0.875

Table 6.1 Values of dimensionless parameters in the performed jet impingement heat transfer computations.

The jet impingement reference case with the conditions listed in Table 3.1 corresponds to $Re = 1.66 \cdot 10^5$, $TI = 0.05$, $\Delta T_{aj}{}^* = 0$ and values for H/D, Pr and TL as listed in Table 6.1. These values for the dimensionless parameters will be referred to as the reference values. Each performed variation of a dimensional parameter did only influence one of the dimensionless parameters Re, TI or $\Delta T_{aj}{}^*$ at a time, while the rest of the dimensionless parameters kept their reference values. In the case of the variation of the wall temperature, all the dimensionless parameters kept their reference values, i.e. the variation of wall temperature did not influence the values of the dimensionless parameters, as indicated above Table 6.1. The obtained heat transfer results presented in section 6.2.1 - 6.2.5 are presented in dimensionless form in the sections below.

6.4.1 Influence of Reynolds number

The influence of the jet Reynolds number on the wall heat transfer is presented in this section. The results are based on the previously presented dimensional heat transfer results obtained by varying the pressure p and the jet velocity at the inlet U, which resulted in jet Reynolds numbers of $1.10 \cdot 10^5$, $1.42 \cdot 10^5$, $1.66 \cdot 10^5$, $3.32 \cdot 10^5$ and $6.64 \cdot 10^5$. The Nusselt number variation with Reynolds number is shown in Fig. 6.18. The remaining dimensionless parameters are equal to their reference values.

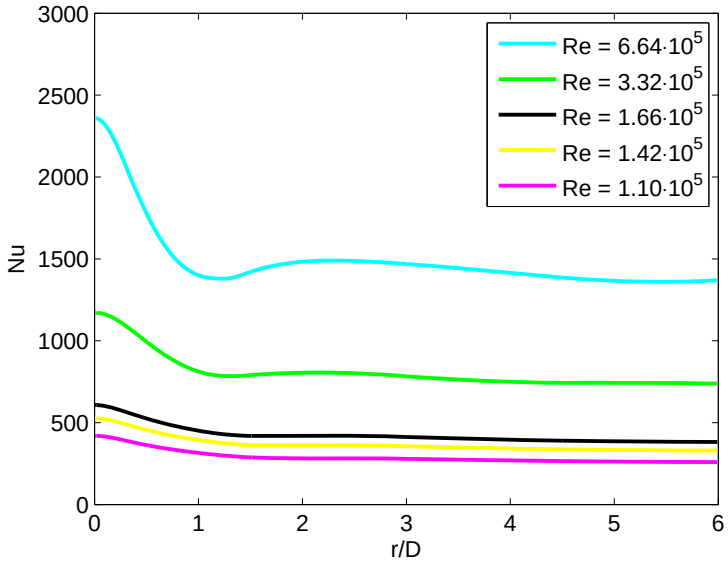

Fig. 6.18 Influence of jet Reynolds number on Nusselt number distribution.

The Nusselt number increases with increasing Reynolds number as expected, and the maximum Nusselt number is located in the stagnation point in all the cases. It is also observed that the secondary peak becomes more pronounced with increasing Reynolds number, and that it is located between $r/D = 2.2$ and $r/D = 2.4$ for the cases investigated. The relative increase in the Nusselt number in the stagnation region is found to be approximately the same as the relative increase in the wall jet region for all the cases presented in Fig. 6.18. The ratio between the Nusselt number at the stagnation point and at $r/D = 6$ is therefore approximately constant for all the cases. In the case of $Re = 1.10 \cdot 10^5$ for instance, the stagnation point Nusselt number is $Nu_0 = 419$, while $Nu = 260$ at $r/D = 6$, i.e. $Nu_0/Nu_{r/D=6} = 1.61$, and in the case of $Re = 6.64 \cdot 10^5$, $Nu_0 = 2360$, while $Nu_{r/D=6} = 1370$, i.e. a ratio of 1.72. This trend is directly visible in Fig. 6.19, where the Nusselt number distribution for each Reynolds number has been normalized by the corresponding Nusselt number at $r/D = 6$, i.e. $Nu_{r/D=6}$.

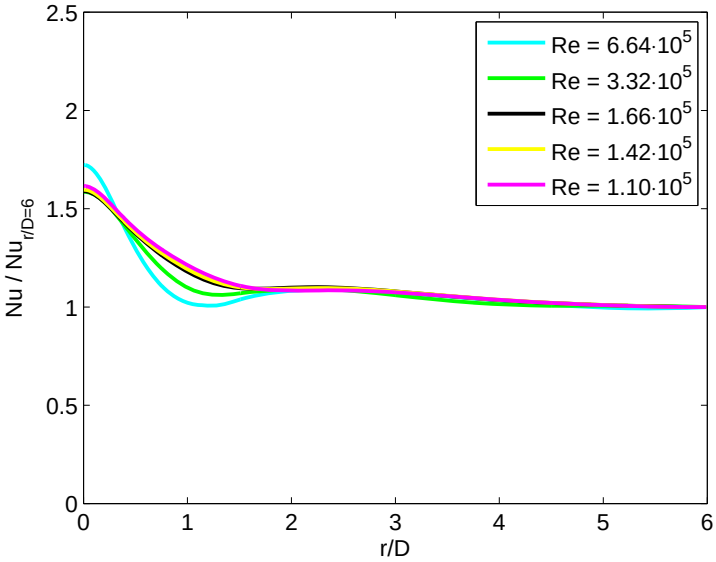

Fig. 6.19 Normalized Nusselt number distribution for different jet Reynolds numbers.

The dominating effect of an increase in the Reynolds number is thus an increase in the Nusselt number level and to a lesser extent a change in the relative Nusselt number distribution along the wall.

6.4.2 Influence of jet turbulence intensity at inlet

The influence of the turbulence intensity at the inlet on the Nusselt number is presented in Fig. 6.20. The results are based on the dimensional heat transfer results presented in section 6.2.5, which were obtained by varying the jet turbulence intensity at the inlet. The values for the turbulence intensity were 1.5%, 2.5%, 5% and 10%. In fact, Fig. 6.20 is similar to Fig. 6.16 as the Nusselt number is here simply a scaling of the dimensional heat flux presented in Fig. 6.16. However, the Nusselt number distributions for the different jet turbulence intensities are still shown here in order to present the Nusselt number magnitude for the different intensities. The remaining dimensionless parameters are equal to their reference values.

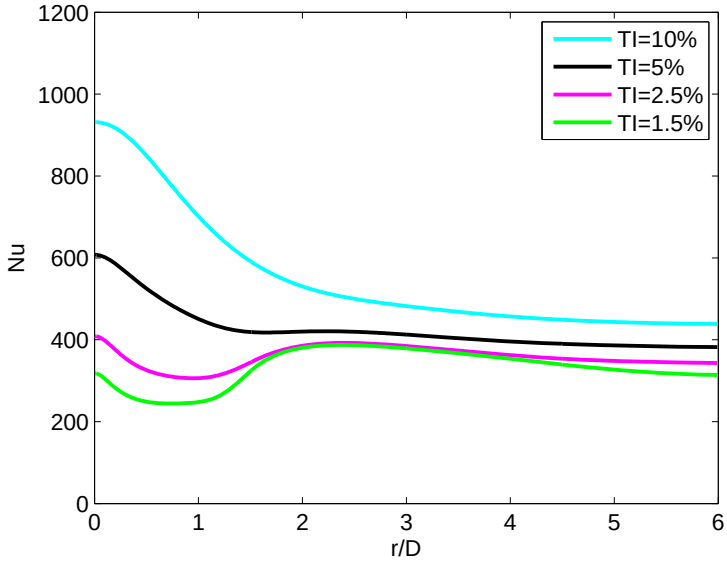

Fig. 6.20 Influence of jet turbulence intensity at the inlet on Nusselt number distribution.

As previously observed in Fig. 6.16, the turbulence intensity has a significant influence on the wall heat transfer and hence on the Nusselt number. In the case of TI = 1.5%, the Nusselt number is in the magnitude of 300, while the Nusselt number reaches values in the magnitude of 900 in the stagnation region in the case of TI = 10%. Detailed comments about the observed trends in the Nusselt number distributions in Fig. 6.20 are not included here as those given below Fig. 6.16 are also valid for the trends seen in Fig. 6.20.

6.4.3 Influence of difference between jet and ambient gas inflow temperatures

The influence of the difference between the jet temperature at the inlet and the ambient gas inflow temperature on the wall heat transfer is presented below in dimensionless form. The results are based on the heat transfer results obtained for different ambient gas inflow temperatures and presented in section 6.2.1. Like the values in Fig. 6.20, the Nusselt number values in Fig. 6.21 are merely a scaling of the heat flux values in Fig. 6.11, and therefore Fig. 6.21 and Fig. 6.11 are similar. Fig. 6.21 is still included to show the resulting Nusselt number levels for different values of the dimensionless temperature difference $\Delta T_{aj}{}^{*}$. The values of $\Delta T_{aj}{}^{*}$ are 0, 0.375, 0.625 and 0.875. The remaining dimensionless parameters are equal to their reference values.

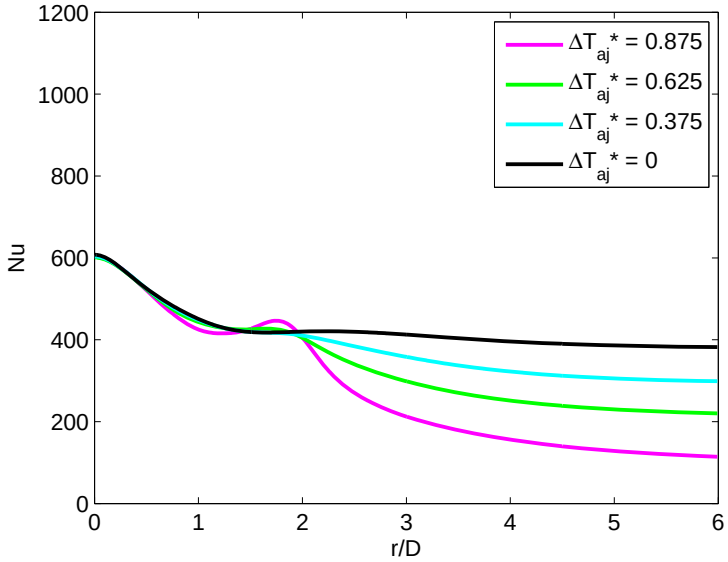

Fig. 6.21 Influence of the dimensionless temperature difference $\Delta T_{aj}{}^{*}$ on the Nusselt number distribution.

The variations of the dimensionless temperature difference $\Delta T_{aj}{}^{*}$ are observed to influence the Nusselt number distribution in the wall jet region, whereas the Nusselt number distribution in the stagnation region is almost unaffected by the variations. The Nusselt number varied between 114 and 382 at $r/D = 6$ depending on $\Delta T_{aj}{}^{*}$, while the stagnation point Nusselt number Nu_0 only varied between 601 and 608. As noted in the comments to Fig. 6.11, this trend is due to the relative short distance between jet inlet and wall in the jet impingement configuration. The short distance prevented a high entrainment of ambient gas into the jet flow before the wall was reached. Further comments to the observed trends in the Nusselt number distributions in Fig. 6.21 are not included here as those given in relation to the trends observed in Fig. 6.11 are also valid for the trends in Fig. 6.21.

6.4.4 Variation of wall temperature

Due to the choice of the jet temperature at the inlet T_j as the reference temperature for the evaluation of the thermophysical properties and density in the dimensionless parameters, Re and Pr do not change in the investigated cases with different wall temperatures. The dimensionless temperature difference $\Delta T_{aj}{}^{*}$ is also unchanged, although T_w appears in the expression for $\Delta T_{aj}{}^{*}$, eq. (6.6). This is because $T_j = T_a$ in the cases with wall temperature variations. The remaining dimensionless parameters on the right hand side of eq. (6.11) are also not influenced by the variations in the wall temperature. The fact that none of the dimensionless parameters on the right hand side of eq. (6.11) change in the cases with different wall temperatures suggests that the Nusselt number distribution should be the same in each of the cases. Therefore, it is of interest to observe the Nusselt number distributions corresponding to these cases. The distributions are presented in Fig. 6.22.

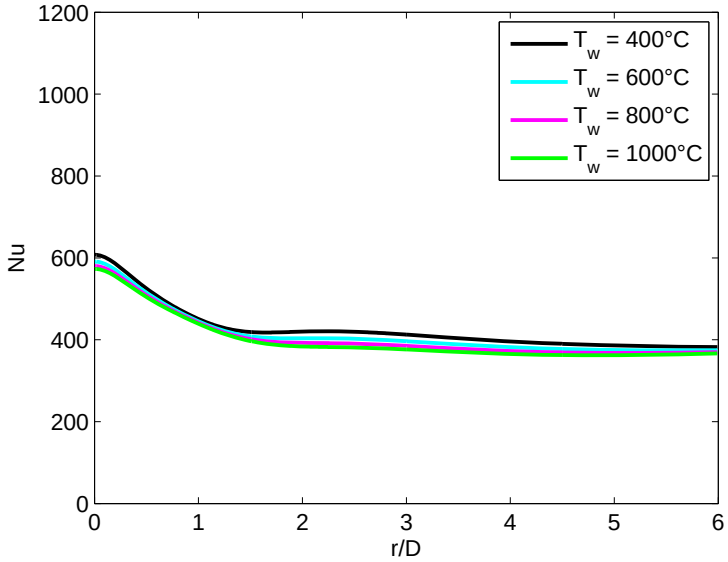

Fig. 6.22 Nusselt number distributions obtained in cases with different wall temperatures.

The Nusselt number distributions in Fig. 6.22 are observed to approximately coincide. In the stagnation region the distributions coincide well, whereas some difference between the distributions is observed around the location of the secondary peak at $r/D = 2.2$. The largest difference between the Nusselt numbers at a fixed radial position is 10.1% (at $r/D = 2.4$). That the Nusselt number distributions approximately coincide when the dimensionless parameters on the right hand side of eq. (6.11) are kept constant indicates that the choice of T_j for evaluating the thermal conductivity in the Nusselt number is appropriate, when T_j is applied for the evaluation of the thermophysical properties and density in the parameters on the right hand side of eq. (6.11).

6.4.5 Stagnation point heat transfer

For the variations of the jet Reynolds number and the turbulence intensity presented in Fig. 6.18 and Fig. 6.20, it is observed that the maximum Nusselt number is located at the stagnation point in all the cases, expect for the case of $TI = 1.5\%$, where it is at $r/D = 2.4$. It was therefore of interest to investigate the variation of the stagnation point Nusselt number Nu_0 with the variations of the jet Reynolds number and the turbulence intensity in more detail. For all the cases presented in Fig. 6.18, the turbulence intensity is 5%, and for the cases in Fig. 6.20, the jet Reynolds number is $1.66 \cdot 10^5$. In order to further investigate the variation of Nu_0 with variations of Re and TI, additional computations were for performed for other combinations of Re and TI. Thus, calculations were performed for turbulence intensities of 1.5%, 2.5% and 10% in the case of a jet Reynolds numbers of $1.10 \cdot 10^5$. The same variation in turbulence intensity was additionally performed for jet Reynolds numbers of $3.32 \cdot 10^5$ and $6.64 \cdot 10^5$. The resulting Nusselt number distributions are shown in Fig. 6.23 in semi-log plots together with the case of $Re = 1.66 \cdot 10^5$ presented previously.

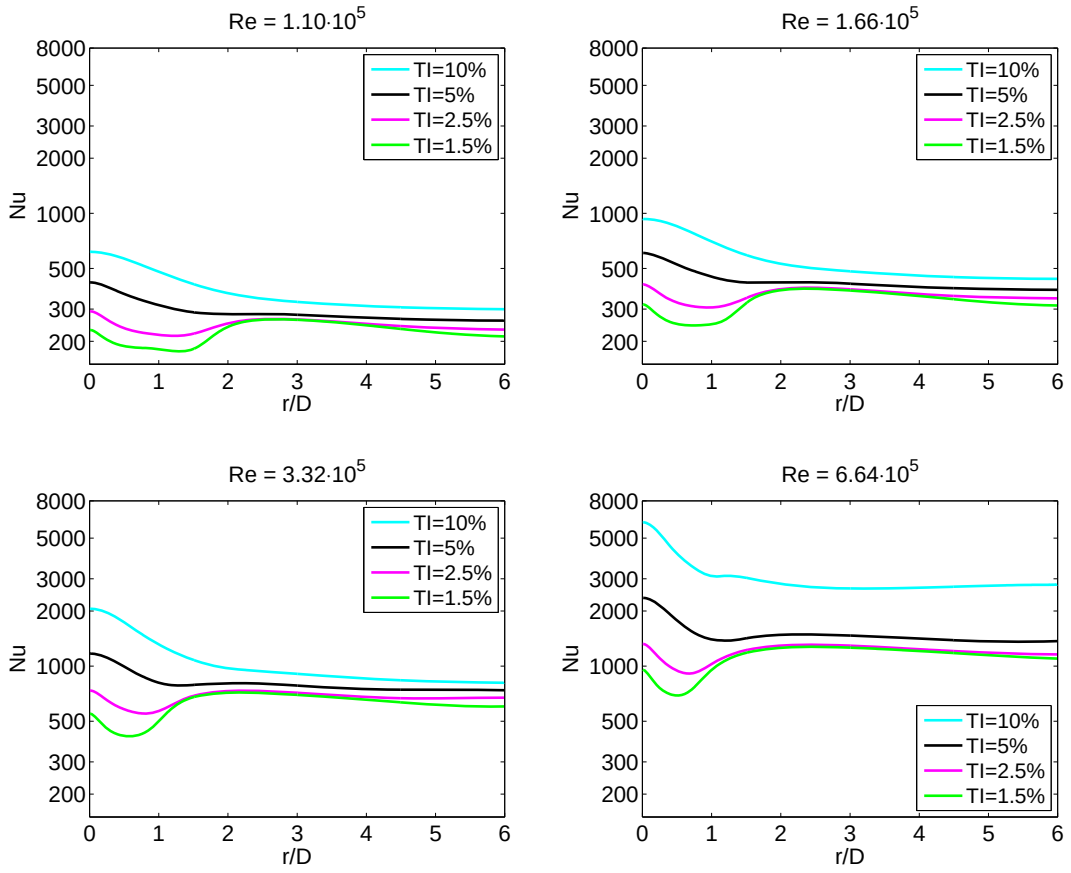

Fig. 6.23 Nusselt number distributions for different jet turbulence intensities at the inlet and different jet Reynolds numbers. The distributions are shown in semi-log plots.

As observed previously, the turbulence intensity has a significant influence on the Nusselt number. The influence is most pronounced in the stagnation region, where the Nusselt number level is highly sensitive to the turbulence intensity, but also the level in the wall jet region is affected to some degree. In all the four cases with a different jet Reynolds number, a secondary peak in the Nusselt number is observed at low turbulence intensities, whereas it disappears at higher intensities. However, in the case of $Re = 6.64 \cdot 10^5$ and $TI = 10\%$, a secondary peak in the Nusselt number distribution is still present, but the location is already at $r/D = 1.2$ in contrast to the other cases with a secondary peak. It is also observed that for this case, the Nusselt number distribution for large r/D is increasing slightly with increasing r/D, which is questionable. Due to time limitations, the cause for these changes was however not identified, and therefore the results for the case of $Re = 6.64 \cdot 10^5$ and $TI = 10\%$ are not included in the continued analysis of results below.

The Nusselt number distributions presented in Fig. 6.23 for the same turbulence intensity have been collected into one figure in Fig. 6.24 in order to compare the trend in the

distribution at different jet Reynolds numbers. The Nusselt number distributions in Fig. 6.24 have in each case been normalized with the Nusselt number at $r/D = 6$.

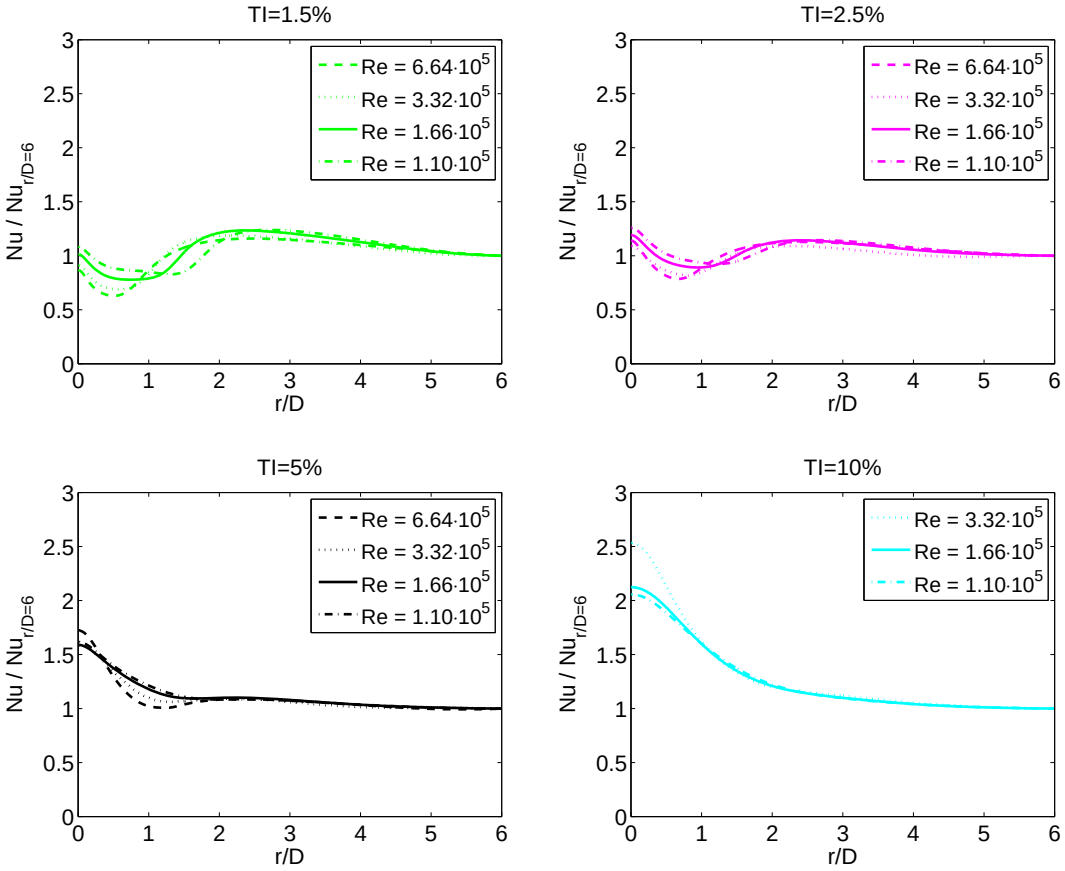

Fig. 6.24 Normalized Nusselt number distributions for different jet Reynolds numbers and different jet turbulence intensities at the inlet.

The trend in the Nusselt number distributions for a fixed turbulence intensity is overall the same although the jet Reynolds number level is changed. In the case of $TI = 10\%$, a significant increase in the stagnation point Nusselt number, relative to $Nu_{r/D=6}$, is observed with increasing Re.

The variation of the stagnation point Nusselt number Nu_0 with the jet Reynolds number is presented in Fig. 6.25, where Nu_0 is plotted against the jet Reynolds number for different turbulence intensities in a log-log plot.

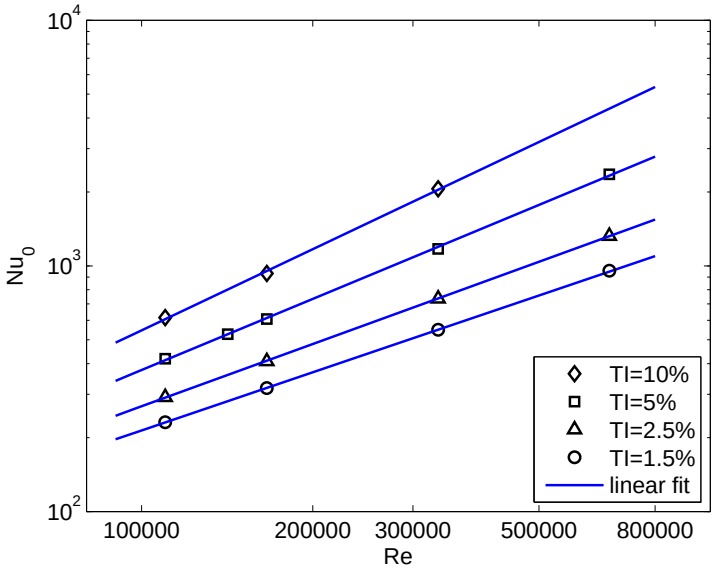

Fig. 6.25 Stagnation point Nusselt number versus jet Reynolds number.

In each case of the different turbulence intensities, the stagnation point Nusselt number is observed to fall closely onto a straight line in the log-log plot when varying the jet Reynolds number. The relationship between the stagnation point Nusselt number and the jet Reynolds number, in the case of a constant jet turbulence intensity at the inlet, can therefore be approximated by a correlation of the form:

$$Nu_0 = C\, Re^{\gamma} \tag{6.15}$$

where γ and C are constants. However, for different values of the turbulence intensity at the inlet, γ and C vary. Hence, γ and C should be functions of TI. In the case of TI = 1.5%, 2.5%, 5% and 10%, the exponent γ is found to be 0.79, 0.84, 0.96 and 1.10, respectively. The form of the correlation between Nu_0 and Re in eq. (6.15) is similar to the form previously found in both experimental and numerical works on jet impingement heat transfer, e.g. [48], [71], [74]. However, the exponent value, ranging from 0.79 to 1.10, is higher than the values previously reported, which are typically about 0.5. This may be due to the high jet Reynolds number range investigated in this work as the jet Reynolds numbers reported in the previous works are considerably lower (from 4000 to 70000). A higher jet Reynolds number may result in the development of a higher turbulence level when approaching the stagnation point and therefore increased heat transfer. For a purely laminar jet flow, the exponent value has been reported to be 0.5 [74], [73]. Differences between the jet turbulence intensity at the inlet in the present work and in the cited works would also influence the stagnation point heat transfer. However, statements about the turbulence intensity were not found in the cited works. Another reason for the difference between the values of the exponent γ obtained in the present work and in the previous works may be an overprediction of the wall heat transfer by the applied numerical modeling. In section 5.2.3, regarding the validation of the numerical modeling, it was found that when comparing numerical results obtained in the validation

study with experimental data, the numerically obtained γ value was 49% higher than the value obtained experimentally, which was, at least to some degree, probably due to an overprediction by the numerical modeling.

The variation of the stagnation point Nusselt number with the jet turbulence intensity at the inlet was also studied. The stagnation point Nusselt number is therefore plotted against the turbulence intensity in Fig. 6.26 for the different jet Reynolds numbers in Fig. 6.23.

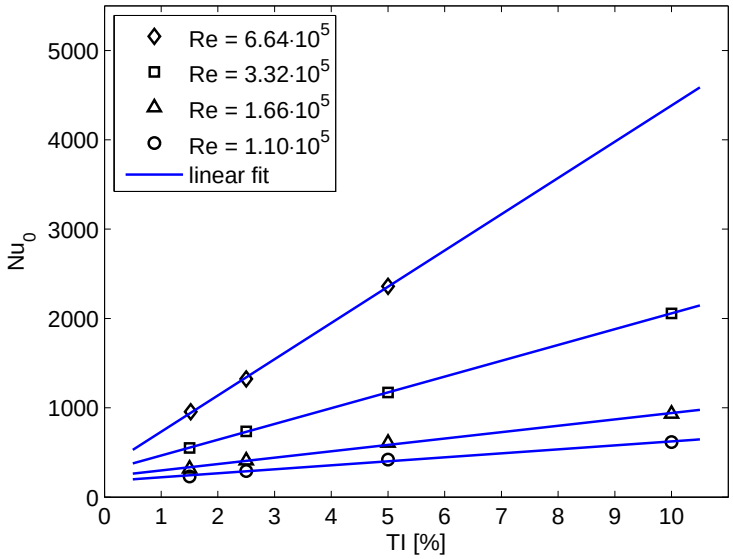

Fig. 6.26 Stagnation point Nusselt number versus jet turbulence intensity at the inlet.

For a fixed jet Reynolds number, a linear relationship is observed between the stagnation point Nusselt number and the turbulence intensity. Hence, the relationship can be expressed as:

$$Nu_0 = a\,TI + b \tag{6.16}$$

where a and b are constants. However, a and b vary for different jet Reynolds numbers, and a and b should therefore be functions of the jet Reynolds number.

6.4.5.1 Stagnation point heat transfer correlation

Based on the above findings for the variation of the stagnation point Nusselt number with the jet Reynolds number and the turbulence intensity, a correlation between Nu_0, Re and TI can be formulated. The correlation should exhibit the trends depicted in Fig. 6.25 and Fig. 6.26, i.e. Nu_0 should vary according to eq. (6.15) for constant TI and according to eq. (6.16) for constant Re. At the same time, the parameters γ and C should vary with TI, and the parameters a and b should vary with Re. However, it seems not possible to fulfill

these requirements simultaneously in one expression as Nu_0 should vary linearly with TI for constant Re, while the exponent γ in eq. (6.15), at the same time, also should vary with TI. If the requirement that γ should vary with TI is neglected, then an expression fulfilling the remainder of the requirements is:

$$Nu_0 = (c_1 TI + c_2) Re^{\gamma} \tag{6.17}$$

where c_1, c_2 and γ are constants. When fitting the expression in eq. (6.17) to the data in Fig. 6.25 and Fig. 6.26, it was found to be advantageous to modify the expression to that presented in eq. (6.18) in order to compensate for not taking the variation of γ with TI into account.

$$Nu_0 = (c_1 TI + c_2) Re^{\gamma} + (c_3 TI + c_4) \tag{6.18}$$

In eq. (6.18), the parameters c_1, c_2, c_3, c_4 and γ are constants. The expression in eq. (6.18) was fitted to the data in Fig. 6.25 and Fig. 6.26 in order to determine the constants. A least-squares method was applied to minimize the relative error between the stagnation point Nusselt numbers obtained from the simulations and those predicted by the correlation. The best fit was obtained for $\gamma = 0.96$, $c_1 = 0.103$, $c_2 = 7.41 \cdot 10^{-4}$, $c_3 = -2626$ and $c_4 = 124$. Thus, the suggested stagnation point Nusselt number correlation is:

$$Nu_0 = (0.103\, TI + 7.41 \cdot 10^{-4}) Re^{0.96} - (2626\, TI - 124) \tag{6.19}$$

The correlation is valid for jet Reynolds numbers from $1.10 \cdot 10^5$ to $6.64 \cdot 10^5$ and turbulence intensities from 1.5% to 10%, given as $TI = 0.015$ to $TI = 0.10$ in eq. (6.19). Within these limits, the maximum deviation between the stagnation point Nusselt numbers obtained from the simulations and the corresponding Nusselt numbers predicted by the correlation is 7%. Stagnation point Nusselt numbers obtained using the correlation are presented in Fig. 6.27.

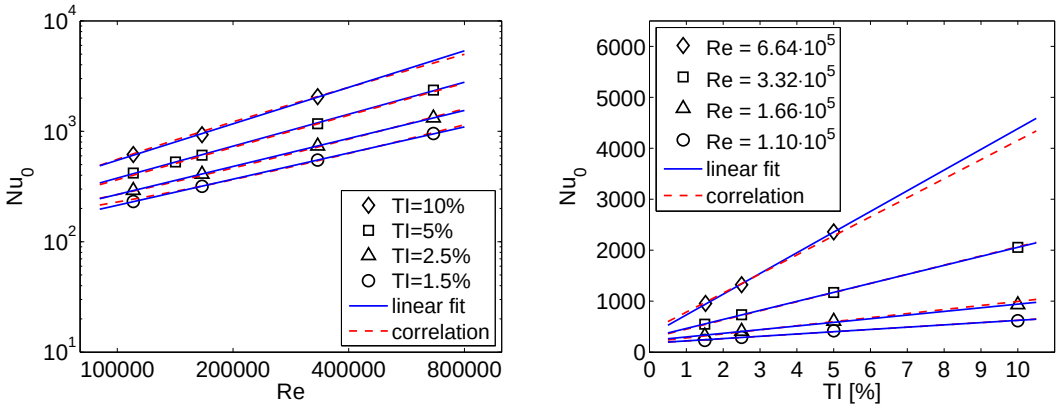

Fig. 6.27 Stagnation point Nusselt number versus jet Reynolds number and jet turbulence intensity at the inlet with correlation predictions presented.

6.4.5.2 Evaluation of proposed correlation

In a previous work by den Ouden and Hoogendoorn [72], experimental data on jet impingement heat transfer between a flat plate and a jet issuing from a round nozzle are stated to be correlated by an expression of the form:

$$Nu_0 = (k_1 + k_2(TI\ Re^{0.5}) + k_3(TI\ Re^{0.5})^2)Re^{0.5} \tag{6.20}$$

where k_1, k_2 and k_3 are constants. The turbulence intensity TI was measured at the nozzle exit, and the characteristic length in the Nusselt and Reynolds number is the nozzle diameter, while the characteristic velocity is the velocity at the nozzle exit. No information is provided in [72] about which temperature was applied for the evaluation of the thermophysical properties and density in Nu_0 and Re, so it is assumed that the properties and density could be regarded as constant between the nozzle exit and the impingement wall. The expression in eq. (6.20) is stated to originally have been developed for stagnation point heat transfer on cylinders, but den Ouden and Hoogendoorn applied it to jet impingement stagnation point heat transfer on a flat plate. They stated that for $H/D < 4$, their data can be correlated by the expression. However, no details are given in [72] about the validity range of the correlation and how good it approximates the experimental data. The values for k_1, k_2 and k_3 given by den Ouden and Hoogendoorn based on fit of the correlation to their data are $k_1 = 0.497$, $k_2 = 3.48 \cdot 10^{-2}$ and $k_3 = -3.99 \cdot 10^{-4}$. Their data are in the jet Reyonlds number range from $0.38 \cdot 10^5$ to $2.64 \cdot 10^5$, and the jet turbulence intensity at the nozzle exit varied apparently from 2.25% to 7.25%, but sufficient information about this is missing in [72]. The linear trend observed in Fig. 6.26 between Nu_0 and TI for a fixed jet Reynolds number can to some degree be validated by considering eq. (6.20) rewritten as:

$$Nu_0 = a\ TI + b \tag{6.21}$$

where

$$a = k_2 Re + k_3\ Re^{1.5}\ TI \tag{6.22}$$

$$b = k_1\ Re^{0.5} \tag{6.23}$$

The absolute value of the second term on the right hand side of eq. (6.22) is relatively small compared to the first term when applying the values for k_2 and k_3 proposed by den Ouden and Hoogendoorn and the TI and Re range of their data. For $Re = 0.38 \cdot 10^5$, the absolute value of the second term varies between 5% and 17% of the value of the first term over the TI range of the data, while for $Re = 2.64 \cdot 10^5$, the absolute value of the second term is between 13% and 43% of the value of the first term. Thereby the coefficient a in eq. (6.21) can be considered as relatively constant for a fixed Re, and thus the linear relationship between Nu_0 and TI for a fixed jet Reynolds number observed in the present work is to some degree supported by the correlation of den Ouden and Hoogendoorn. This is illustrated in Fig. 6.28. The figure shows Nu_0 predictions which

have been obtained by using the correlation in eq. (6.20) for various *TI* and *Re* within the range of the data by den Ouden and Hoogendoorn. The applied values for the constants k_1, k_2 and k_3 were as given in [72], i.e. $k_1 = 0.497$, $k_2 = 3.48 \cdot 10^{-2}$ and $k_3 = -3.99 \cdot 10^{-4}$. The experimental data of den Ouden and Hoogendoorn could not be used directly in the check for linearity between Nu_0 and *TI*, because information about *TI* for most of the reported measurements was not available in [72]. The relationship between Nu_0 and *TI* in Fig. 6.28 is seen to be approximately linear. The observed linear trend in Fig. 6.26 seems therefore reasonable when comparing with the trend exhibited by the correlation of den Ouden and Hoogendoorn.

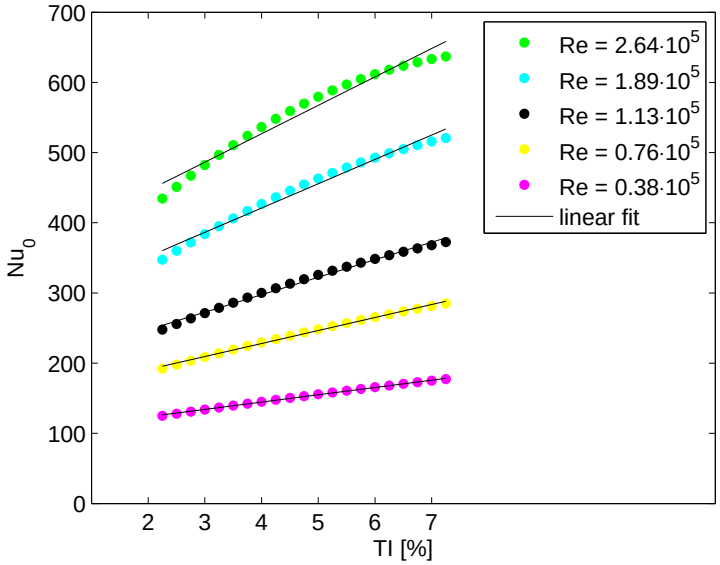

Fig. 6.28 Stagnation point Nusselt numbers predicted with the correlation of den Ouden and Hoogendoorn [72], eq. (6.20), for different turbulence intensities and jet Reynolds numbers.

It is also of interest to evaluate the actual predictions by the proposed correlation in eq. (6.19). A comparison of correlation predictions against experimental data is therefore performed. However, it has only been possible to find a few experimental data within the validity range of the correlation, i.e. a jet Reynolds number between $1.10 \cdot 10^5$ and $6.64 \cdot 10^5$ and a jet turbulence intensity between 1.5% and 10% for the case of $H/D = 2$ as only quite limited experimental data exist in this jet Reynolds number range. Experimental data by den Ouden and Hoogendoorn [72] are used although the data available in [72] are not sufficiently detailed to provide a satisfactory basis for a validation of the proposed correlation. As indicated earlier, information about the turbulence intensity at the nozzle exit for most of their measurements are missing. However, more suitable data have not been found. For a case of $H/D = 2$, den Ouden and Hoogendoorn reported Nu_0 values for three jet Reynolds numbers in the range mentioned above, these are $1.13 \cdot 10^5$, $1.89 \cdot 10^5$ and $2.64 \cdot 10^5$. However, the only information in [72] about the jet turbulence intensity at the nozzle exit is for a case with a jet Reynolds number of $0.76 \cdot 10^5$. For this case, the turbulence intensity is stated to be $TI = 3.5\%$ for an undisturbed jet, i.e. without grids inserted into the nozzle for enhancing the turbulence.

Three different turbulence intensities around TI = 3.5% were therefore assumed when applying the correlation in eq. (6.19) at each of the three above-mentioned jet Reynolds numbers. The results are presented in Table 6.2 together with the average relative difference between the experimentally determined and the predicted stagnation point Nusselt number, $Nu_{0,exp}$ and $Nu_{0,corr}$, in each case of the assumed turbulence intensities.

Stagnation point Nusselt numbers obtained with correlation and in experiments				
	$Nu_{0,exp}$	$Nu_{0,corr}$ (TI = 2.0%)	$Nu_{0,corr}$ (TI = 3.5%)	$Nu_{0,corr}$ (TI = 5.0%)
$Re = 1.13 \cdot 10^5$	260	270	340	411
$Re = 1.89 \cdot 10^5$	330	397	537	678
$Re = 2.64 \cdot 10^5$	380	520	728	937
Avg. relative diff.		20%	62%	103%

Table 6.2 Stagnation point Nusselt numbers predicted with the correlation proposed in the present work, eq. (6.19), versus experimental data of den Ouden and Hoogendoorn [72].

The results in Table 6.2 will be discussed below Fig. 6.29. The correlation in eq. (6.20), with the constants k_1 = 0.497, $k_2 = 3.48 \cdot 10^{-2}$ and $k_3 = -3.99 \cdot 10^{-4}$ as given by den Ouden and Hoogendoorn in [72], has also been applied for the jet Reynolds numbers in Table 6.2 in order to compare predictions by this correlation with the experimental data of den Ouden and Hoogendoorn as well. For each of the jet Reynolds numbers, the turbulence intensity was varied between the same three intensities as in Table 6.2. The results are presented in Table 6.3 and will be discussed below Fig. 6.29. Based on experimental work with jet impingement heat transfer between a flat plate and a jet issuing from a round nozzle, Hofmann et al. [70] recently suggested a correlation for the local Nusselt number Nu along the plate in terms of Re, r/D and the Prandtl number Pr, but with no explicit description of the influence of the turbulence intensity at the nozzle exit. The suggested correlation is:

$$Nu = 0.055(Re^3 + 10Re^2)^{0.25} Pr^{0.42} \mathrm{e}^{-0.025(r/D)^2} \qquad (6.24)$$

The characteristic length in the Nusselt and Reynolds number is the nozzle diameter. It is not stated explicitly in [70], which velocity the Reynolds number is based on, but it is assumed to be based on the velocity at the nozzle exit. As in the case of the article by den Ouden and Hoogendoorn [72], no information is available in [70] about which temperature was used for the evaluation of the thermophysical properties and density in the dimensionless numbers. It is therefore assumed that the properties and density could be regarded as constant between the nozzle exit and the impingement wall in the experiments by Hofmann et al.. The correlation of Hofmann et al. is stated to be valid for jet Reynolds numbers between $1.40 \cdot 10^4$ and $2.30 \cdot 10^5$, H/D ratios from 0.5 and up to 10, and r/D ratios up to 8. No validity range is given for Pr. The correlation in eq. (6.24) is

thus also valid in the stagnation point and has been applied for the jet Reynolds numbers in Table 6.2 for comparison of its predictions with the experimental data of den Ouden and Hoogendoorn and the predictions obtained with the other correlations in eq. (6.19) and eq. (6.20). As the Prandtl number in the experiments of den Ouden and Hoogendoorn is stated in [72] to have been 0.71, this value was applied for Pr in eq. (6.24). The resulting Nu_0 predictions are presented in Table 6.3.

Stagnation point Nusselt numbers obtained with correlations and in experiments					
	$Nu_{0,exp}$	$Nu_{0,corr,Ouden}$ (TI = 2.0%)	$Nu_{0,corr,Ouden}$ (TI = 3.5%)	$Nu_{0,corr,Ouden}$ (TI = 5.0%)	$Nu_{0,corr,Hofmann}$
$Re = 1.13 \cdot 10^5$	260	240	286	326	294
$Re = 1.89 \cdot 10^5$	330	334	406	463	432
$Re = 2.64 \cdot 10^5$	380	417	511	579	555
Avg. relative diff.		6%	23%	39%	30%

Table 6.3 Stagnation point Nusselt numbers predicted with the correlation of den Ouden and Hoogendoorn [72], eq. (6.20), and with the correlation of Hofmann et al. [70], eq. (6.24), versus experimental data of den Ouden and Hoogendoorn [72].

The data in Table 6.2 and Table 6.3 are illustrated in Fig. 6.29 below. For the predictions obtained with the correlation of the present work and those obtained with the correlation of den Ouden and Hoogendoorn, three stagnation point Nusselt numbers are shown for each jet Reynolds number and correspond to the different turbulence intensities given in Table 6.2 and Table 6.3.

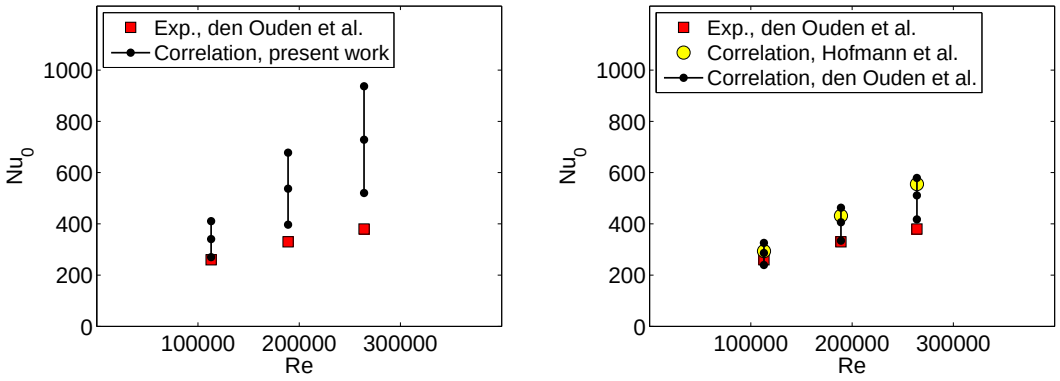

Fig. 6.29 Left: Stagnation point Nusselt numbers obtained with the correlation proposed in the present work, eq. (6.19), versus experimental data of den Ouden and Hoogendoorn [72]. Right: Stagnation point Nusselt numbers obtained with the correlation of den Ouden and Hoogendoorn [72], eq. (6.20), and with the correlation of Hofmann et al. [70], eq. (6.24), versus experimental data of den Ouden and Hoogendoorn [72].

The results in Table 6.2 indicate a rather significant difference between the stagnation point Nusselt number predictions obtained with the proposed correlation in the present work, eq. (6.19), and the experimental data of den Ouden and Hoogendoorn. If it is assumed that the turbulence intensity in the experiments was 3.5%, then the correlation overpredicts the stagnation point Nusselt numbers by 62% in average. In comparison, the predictions obtained with the correlation of den Ouden and Hoogendoorn, eq. (6.20), deviate from the experimental data by 23% in average for TI = 3.5%. The correlation by Hofmann et al., eq. (6.24), gives Nu_0 predictions which deviate from the experimental data by 30% in average. The better agreement between the predictions obtained with the correlation of den Ouden and Hoogendoorn and the experimental data may be due to that this correlation is directly fitted to the data. However, also the predictions obtained with the correlation of Hofmann et al. are in better agreement with the experimental data, although this correlation is not based on these data. A reason for these observations may be that both the experimental data of den Ouden and Hoogendoorn and the data on which the correlation of Hofmann et al. are based are obtained in configurations with considerably lower temperature differences than in the investigated numerical configuration. Thus, the variation of the thermophysical properties and the density across the flow domain was significantly different in these configurations, and the proposed correlation in eq. (6.19), based on data from the numerical configuration, may therefore be inappropriate for the prediction of stagnation point Nusselt numbers in the configuration of den Ouden and Hoogendoorn. The overprediction exhibited by the proposed correlation, when compared to the experimental data, is however believed to be caused mainly by the numerical modeling applied in the present work, because an overprediction in the stagnation point heat transfer was observed previously in the validation study of the numerical modeling in section 5.2.3. The observed overprediction was 15% in a case with a jet Reynolds number of 23750 and 45% when the jet Reynolds number was increased to 70000.

In conclusion, the proposed correlation in eq. (6.19), based on the numerical heat transfer results of the present work, seems to overpredict the stagnation point Nusselt number when comparing with experimental data on jet impingement heat transfer obtained at a moderate temperature difference between jet and wall. However, the experimental data basis used in the comparison is rather limited and not sufficiently detailed to perform a satisfactory validation of the proposed correlation. Hence, the apparent overprediction exhibited by the correlation is probably due to overpredictions in the numerical heat transfer results on which the correlation is based, but it may also, at least in part, be due to an inappropriate experimental data basis used in the validation of the correlation. More suitable data are however difficult to find as only relatively few studies seem to have been performed on jet impingement heat transfer at high jet Reynolds numbers, i.e. above 10^5, and none have been found with a temperature difference between the jet and the wall in the same magnitude as the temperature difference applied in the present work. The data which are existing for high jet Reynolds number cases unfortunately lack enough information about the configuration conditions to be suitable for use in validation studies of numerical results.

7 Summary and discussion of results

The obtained heat transfer results in the present work are summarized below, and an estimation of the peak piston surface heat flux level in large marine diesel engines based on the obtained results is discussed.

7.1 Jet impingement heat transfer results

The numerical investigation of jet impingement heat transfer was performed in a configuration with a H/D ratio of 2, and where the jet impinged normally onto the wall. The jet Reynolds number was between $1.10 \cdot 10^5$ and $6.64 \cdot 10^5$, and the turbulence intensity of the jet at the inlet was varied between 1.5% and 10% at different jet Reynolds numbers. The influence of the ambient gas inflow temperature on the wall heat transfer was also studied. The resulting local Nusselt numbers along the wall were calculated for dimensionless radial distances r/D between 0 and 6. The Nusselt numbers were observed to vary between 114 and 2360, depending on Re, TI, ΔT_{aj}^* and r/D. In most cases, the highest Nusselt number was found in the stagnation point, while a secondary peak in the Nusselt number distribution was observed at about $r/D = 2.4$, which is consistent with previous findings in the literature. However, for a relative high jet turbulence intensity at the inlet of 10%, no secondary peak was observed, and for a relative low jet turbulence intensity at the inlet of 1.5%, the maximum Nusselt number was found at the secondary peak in the Nusselt number distribution. The turbulence intensity at the jet inlet was seen to have a significant influence on the resulting Nusselt number level in the stagnation region, whereas in the wall jet region, the influence was less pronounced. The difference between ambient gas inflow temperature and the jet temperature at the inlet, on the other hand, influenced almost only the Nusselt number distribution for $r/D > 2$ due to the short distance between jet inlet and wall, which prevented a significant entrainment of ambient gas into the jet in the stagnation region.

As the highest Nusselt number appeared in the stagnation point in most of the studied cases, special attention was paid to the stagnation point Nusselt number in order to try to describe the variation of this parameter with the jet Reynolds number and the turbulence intensity at the jet inlet. The variation of Nu_0 with Re was found to be of the form previously reported in the literature, i.e. $Nu_0 \propto Re^{\gamma}$. However, the exponent γ is higher than typically observed in previous experimental and numerical works. This is primarily believed to be due to an overprediction of the wall heat transfer by the applied numerical modeling. It might however also to some extent be attributed to differences between the conditions in the present jet impingement configuration and the conditions in the studies used for comparison. The jet Reynolds numbers in the present work are for instance considerably higher than in the studies used for comparison. The stagnation point Nusselt number was seen to vary linearly with the turbulence intensity at the jet inlet. This was found to be supported to some extent by a previous experimental study, but no detailed investigation of the variation of Nu_0 with TI at high jet Reynolds numbers has been found in the literature. The stagnation point Nusselt number in the present work was observed

to vary between 231 and 2360, depending on *TI* and *Re*. Based on the variation of Nu_0 with *Re* and *TI*, a correlation between these three parameters was suggested for jet Reynolds numbers between $1.10 \cdot 10^5$ and $6.64 \cdot 10^5$ and jet turbulence intensities at the inlet between 1.5% and 10%. A comparison of Nu_0 predictions by the suggested correlation with experimental Nu_0 data at jet Reynolds numbers between $1.13 \cdot 10^5$ and $2.64 \cdot 10^5$ indicated an overprediction by the correlation of about 62%. This is considered to be a significant overprediction, and it is believed to be due to too high wall heat transfer predictions by the applied numerical modeling as mentioned above. Only few experimental data were however used in the comparison, and information about the conditions in the experiment, in which they were obtained, is limited. More suitable data for a validation of the suggested correlation were however not found, and a satisfactory validation of the correlation was therefore not possible. The degree of overprediction which the proposed correlation may cause was thus difficult to determine accurately, but an overprediction in the magnitude of 50% to 100% is considered to be probable. The trend in the resulting Nusselt number distributions along the impingement wall obtained from the computations and the observed form of the variation of Nu_0 with *Re* and *TI* seemed however reliable. Hence, although the obtained Nusselt numbers may be overpredicted, the observed trends in the variation of *Nu* with *Re* and *TI* are considered correct.

7.2 Estimation of peak heat flux level on piston surface

The dimensional wall heat transfer results obtained in the present study, and on which the above mentioned dimensionless results are based, are summarized below. They form the basis for an estimation of the peak piston surface heat flux level in large marine diesel engines.

For the reference case with a jet temperature at the inlet of 2000°C, a wall temperature of 400°C, a jet velocity at the inlet of 10 m/s, a jet turbulence intensity at the inlet of 5%, a jet diameter at the inlet of 0.05 m, a distance between jet inlet and wall of 0.10 m, and a pressure of 180 bar, the peak wall heat flux was found to be 3.0 MW/m^2. These reference conditions were based on estimations of the conditions during combustion in large marine diesel engines. Parameter variations around the reference conditions were performed as the estimations were considered to be relatively uncertain. Thus the wall temperature was increased in steps up to 1000°C at which the peak wall heat flux decreased to about 1.8 MW/m^2. Similarly, decreasing the pressure to 120 bar, reduced the peak heat flux to 2.1 MW/m^2. An increase in the jet velocity at the inlet up to 40 m/s, increased the peak heat flux to 11.7 MW/m^2. Increasing and decreasing the jet turbulence intensity at the inlet to 10% and 1.5%, resulted in peak heat flux levels of 4.6 MW/m^2 and 1.9 MW/m^2, respectively. Based on these results, a peak heat flux interval from about 2 MW/m^2 to 12 MW/m^2 can be established for the studied cases. A simultaneous change in different conditions from their reference values can however result in peak heat fluxes outside this range. Taking into account a probable overprediction of the numerical heat flux results in the magnitude of 50% to 100%, an expected peak heat flux interval for the conditions

studied may instead be from about 1 MW/m^2 to 8 MW/m^2 with the reference case resulting in a peak heat flux level of about 1.8 MW/m^2.

In the studied jet impingement configuration, the angle of inclination for the jet impingement was 90°, i.e. the jet impinged normally onto the wall. The combustion products in the actual impingement process in the engine are however likely to impinge on the piston surface at an inclination angle less than 90° due to the direction of the fuel injection. A swirling motion in the engine combustion chamber, during fuel injection and combustion, is also likely to reduce the effective angle of inclination for the impingement of combustion products on the piston surface. However, no cross flow representing a swirling motion in the engine was present in the computations. A reduction of the inclination angle for the impingement process may probably reduce the resulting peak heat flux. Another difference between the in-cylinder heat transfer process in the engine and the process studied in the numerical investigation in the present work is that heat transfer by thermal radiation was not included in the numerical investigation. The contribution from thermal radiation to the in-cylinder surface heat flux is however considered to be important in diesel engines due to radiating soot particles as mentioned in chapter 2. Hence, based on the these considerations, the jet impingement heat transfer results obtained in the present work can be viewed as providing an upper estimate of the expected peak convective heat flux level on the piston surface in the considered large marine diesel engines. The peak convective heat flux level is thus expected to be from about 1 MW/m^2 and up to 8 MW/m^2 and likely in the lower part of this interval.

As the contribution from thermal radiation to the piston surface heat flux was not investigated in the performed numerical study and due to the fact that it is considered to be important in diesel engines, an estimation of the magnitude of the thermal radiation contribution is performed in the following. An estimate may be obtained by making some simplifying assumptions about the in-cylinder conditions during combustion. It is assumed that the piston surface is flat and that combustion products cover most of the area in a cross sectional plane through the engine cylinder above the piston surface. Further assumptions are a uniform piston surface temperature and emissivity and that the cloud of combustion products can be approximated by a body with an effective uniform temperature and emissivity on the surface facing the piston and which is assumed approximately parallel to the piston surface. The distance between the piston surface and the body surface is assumed short enough that radiation exchange between each surface and the cylinder wall can be neglected. The effective thermal radiation from the combustion products to the piston surface can then be estimated by eq. (2.3) by assuming that the heat transfer case is a case of exchange of thermal radiation between two parallel infinite surfaces with uniform temperatures and radiation properties. The view factor between the surfaces is then unity and the surface areas are equal. Denoting the surface of the combustion product body by index 1 and the piston surface by index 2 gives $A_1 = A_2$ and $F_{12} = 1$. An expression for the rate of heat transfer by thermal radiation from the combustion products to the piston surface, $\dot{Q}_{1\rightarrow 2}$, is then obtained by applying eq. (2.3):

$$\dot{Q}_{1\to2} = \frac{\sigma(T_1^4 - T_2^4)}{\frac{1-\varepsilon_1}{\varepsilon_1 A_1} + \frac{1}{A_1 F_{12}} + \frac{1-\varepsilon_2}{\varepsilon_2 A_2}} = \frac{\sigma A_1 (T_1^4 - T_2^4)}{\frac{1}{\varepsilon_1} + \frac{1}{\varepsilon_2} - 1} \tag{7.1}$$

Assuming that the emissivities are unity, $\varepsilon_1 = \varepsilon_2 = 1$, gives:

$$\dot{Q}_{1\to2} = \sigma A_1 (T_1^4 - T_2^4) \tag{7.2}$$

As the areas A_1 and A_2 are assumed equal, the contribution to the piston surface heat flux from thermal radiation is therefore estimated by:

$$q_2 = \frac{\dot{Q}_{1\to2}}{A_2} = \sigma(T_1^4 - T_2^4) \tag{7.3}$$

Applying an effective temperature for the combustion products of 2000°C and a piston surface temperature of 400°C results in an estimation of the contribution to the piston surface heat flux from thermal radiation of approximately 1.5 MW/m^2. This value is however a coarse estimate. The real value is likely to be lower as the combustion products probably do not cover a full cross sectional plane through the engine cylinder and will also be exchanging thermal radiation with other combustion chamber surfaces than the piston. Furthermore, the emissivities are probably also less than one.

7.3 Evaluation of estimated peak heat flux level on piston surface

The estimated peak convective and thermal radiation heat flux levels on the piston surface in large marine diesel engines mentioned in section 7.2 are in the following compared to values reported in the literature for piston surface heat flux levels in diesel engines.

Based on results found in the literature and mentioned in chapter 2, a peak piston surface heat flux in the magnitude of 1 – 10 MW/m^2 may be expected in large marine diesel engines, and the contribution by thermal radiation may be significant, possibly up to about 50%. On basis of the performed numerical investigation in the present work, the peak convective piston surface heat flux is estimated to be in the interval from about 1 MW/m^2 and up to 8 MW/m^2 and likely in the lower part of this interval. A coarse estimate of the contribution from thermal radiation mentioned in section 7.2 is about 1.5 MW/m^2, but the actual value is likely to be lower, so the calculated value can serve to indicate an upper estimate of the contribution from thermal radiation to the piston surface heat flux. The expected peak piston surface heat flux based on the present work is hence in the interval from about 1 MW/m^2 to 9.5 MW/m^2 and probably in the lower part of the interval. If the thermal radiation heat flux is as high as the estimated 1.5 MW/m^2, the contribution from thermal radiation would vary between 16% and 60% of the peak heat flux, depending on the convective heat flux level. However, as the thermal radiation heat flux is expected to be somewhat lower than 1.5 MW/m^2, the relative contribution from

thermal radiation is likely to be in the lower part of this interval. The obtained estimation of the peak piston surface heat flux and the estimated distribution between contributions from convection and thermal radiation seem thus to be in accordance with the expectations based on results reported in the literature. The obtained intervals for the expected peak heat flux level and the expected distribution between convective and radiation contributions are however relatively large, and likewise are the corresponding intervals based on results from the literature. More accurate estimations, i.e. more narrow intervals, require however better knowledge of the in-cylinder conditions during combustion in large marine diesel engines. This may be gained both by experimental measurements and by further numerical investigations and probably best by a combination of both. Therefore, continued research efforts in these fields are encouraged, which would also help to complement the sparse literature in the area of in-cylinder heat transfer in large marine diesel engines.

8 Conclusions

In-cylinder heat transfer in large two-stroke uniflow scavenged marine diesel engines has been investigated in the present work. The focus was on the heat transfer to the piston surface during the combustion phase of the engine cycle with an objective to obtain information about the peak heat flux level experienced on the piston surface. The investigation was performed numerically using a CFD software package.

The heat flux level experienced in the event of impingement of hot combustion products on the piston surface during combustion was estimated by investigating the heat transfer between jet and wall in a jet impingement configuration. In the configuration, a hot round gas jet impinged normally onto a flat wall at conditions approximating in-cylinder conditions during combustion in large marine diesel engines. The ratio between the jet inlet to wall distance and the jet diameter at the inlet was 2. The conditions applied in the configuration resulted in jet Reynolds numbers in the range from $1.10 \cdot 10^5$ to $6.64 \cdot 10^5$ with the Reynolds number based on jet inlet conditions.

In most of the investigated cases, the maximum Nusselt number was observed in the stagnation point, and hence a closer investigation of the stagnation point heat transfer was performed. The stagnation point Nusselt number varied between 231 and 2360, depending on the jet Reynolds number and the turbulence intensity at the jet inlet, which was between 1.5% and 10%. The variation of the stagnation point Nusselt number with the jet Reynolds number was observed to be of the form previously reported for lower jet Reynolds numbers, i.e. $Nu_0 \propto Re^{\gamma}$. The variation of the stagnation point Nusselt number with the turbulence intensity at the jet inlet was found to be linear. Based on these findings, a correlation between the stagnation point Nusselt number, the jet Reynolds number and the turbulence intensity at the jet inlet was suggested, which is valid for high jet Reynolds numbers.

The suggested correlation seemed however to overpredict the stagnation point Nusselt number when comparing predictions by the correlation with experimental data. This is believed to be caused mainly by an overprediction of the wall heat transfer in the performed numerical computations. The experimental data used in the comparison were however few and not sufficiently detailed to provide a satisfactory basis for a validation of the correlation. More suitable data for a validation were not found as the number of jet impingement heat transfer studies focusing on high jet Reynolds number cases ($> Re = 10^5$) is very limited. Therefore, the performance of detailed experimental jet impingement heat transfer investigations at high jet Reynolds numbers is encouraged.

Based on the performed jet impingement heat transfer investigation, information was obtained about the potential piston surface heat flux level in the event of impingement of hot combustion products on the piston during combustion. The performed investigation indicated a peak convective heat flux level in the interval from about 1 MW/m^2 and up to 8 MW/m^2 with the actual value most likely being in the lower part of this interval. Heat transfer by thermal radiation was not included in the jet impingement heat transfer

investigation. However, a coarse estimate indicated a possible maximum contribution from thermal radiation to the piston surface heat flux in the magnitude of 1.5 MW/m^2. The peak surface heat flux level is hence estimated to be from about 1 MW/m^2 and up to about 9.5 MW/m^2 with the actual value most likely being in the lower part of this interval. With these estimates, the contribution from thermal radiation to the peak surface heat flux may be up to 60%.

The obtained estimate for the peak piston surface heat flux level and the distribution between contributions from convection and thermal radiation correspond to that previously reported in the literature for automotive size diesel engines. Comparison of the obtained results to other studies of piston surface heat transfer in large marine diesel engines was difficult as no studies were found on this subject for this class of engines. However, in an experimental study of the in-cylinder heat transfer in a large marine diesel engine, a peak surface heat flux level of about 1.2 MW/m^2 was reported for a position in the cylinder cover. The heat transfer contribution from thermal radiation was estimated to be about 0.9 MW/m^2. These levels seem to support the estimated heat flux levels based on the present work.

The estimated interval for the peak piston surface heat flux level is relatively large. A more accurate estimate was however difficult to achieve as the actual conditions in the combustion chamber of the considered engines during combustion are complex and not well-known. A better estimate of the peak heat flux level may be obtained with improved information of the in-cylinder conditions during combustion. Hence, further research in this area is encouraged, both experimentally and numerically.

9 Further work

Several further investigations in relation to the performed work would be interesting. These investigations are mentioned and discussed below.

9.1 Numerical work

With respect to the performed numerical jet impingement heat transfer investigations, it would be of interest to perform some further parameter variations. In the performed investigations, the jet velocity was constant across the inlet. This velocity profile was imposed for simplicity. However, the actual velocity profile of the impinging combustion products in the engine during combustion is presumably non-constant. Therefore, a study would be relevant of the influence of the jet velocity profile at the inlet on the wall heat transfer in the jet impingement computations. The effect of the turbulence length scale at the jet inlet on the wall heat transfer should also be examined, as this turbulence parameter was the same in all the investigated cases. The ratio between the jet inlet to wall distance and the jet diameter at the inlet in the jet impingement configuration, i.e. the H/D ratio, may also be varied. For unchanged conditions at the jet inlet, this is expected to influence both the Nusselt number magnitude and the distribution with radial distance from the stagnation point. However, if the H/D ratio is altered, the jet inlet conditions should be modified accordingly, as they should then correspond to conditions either further away or closer to the piston surface, depending on an increase or decrease in the H/D ratio.

It would also be interesting to study the effect of jet inclination angle and cross flow on the wall heat transfer as the actual impingement process on the piston surface is likely to occur at an inclination angle less than 90° due to the direction of fuel injection and the presence of swirl in the engine. This is expected to reduce the surface heat transfer, and the degree of reduction with inclination angle and cross flow strength would be relevant to determine. A change of the jet inclination angle and the inclusion of a cross flow would however require modifications of the applied jet impingement configuration. Inclusion of combustion reactions in the numerical modeling would also be of interest in order to observe the influence on the wall heat transfer of the presence of a reacting jet. Localized points of heat release near the wall may result in an increased wall heat transfer. Inclusion of heat transfer by thermal radiation may be relevant as well, especially if soot formation is included and correct soot radiating properties can be accounted for. In all the performed investigations in the present work, the wall temperature was imposed and thus predetermined. The actual piston surface temperature is however not known, so the performance of conjugate heat transfer calculations would also be interesting, where wall material is included in the modeling, so both the gas-wall interface heat transfer and the wall temperature are calculated. The effect on the piston surface heat transfer of applying different piston crown materials and surface coatings could then also be tested. However, a thermal boundary condition on the underside of the wall would still be required.

A further modification of the applied jet impingement configuration would be to increase the distance between the wall and the inlet, so the distance corresponds to the distance between fuel injector and piston surface along the direction of fuel spray injection when the piston is at TDC (see Fig. 3.3). The inlet diameter should then equal the nozzle hole diameter in the fuel injector. Liquid droplets may then be injected instead of gas in order to model fuel injection, and wall boundaries may be applied instead of the pressure boundaries. Evaporation, ignition and combustion should then also be modeled, and the modeling in this case would thus be more complex than that performed in the present work. This would increase the factors influencing the heat transfer results as discussed in section 1.5. However, the impingement process in such a configuration may approximate better the actual impingement process in the engine, and heat transfer results obtained in a configuration like this would be interesting to compare with results from the present study.

A different numerical approach to obtain information about the piston surface heat transfer is to perform engine cycle CFD simulations. This approach involves several submodels as discussed in section 1.5, which substantially increases the complexity of the modeling and thereby the amount of factors influencing the heat transfer results. Therefore the jet impingement approach was applied in the present work, i.e. in order to keep the modeling as simple as possible and thus limit the amount of influencing factors. However, the advantage of performing engine cycle simulations is that fewer in-cylinder conditions need to be estimated or guessed than when performing jet impingement heat transfer simulations similar to those in the present work. The interval suggested in section 7.2 for the peak convective heat flux level on the piston surface is relatively large because it was difficult to estimate representative conditions for the actual impingement process in the engine. Thus, to perform engine cycle CFD simulations is considered to be relevant as well, although the risk of erroneous predictions may increase with the increased complexity of the modeling, since the quality of the predictions will depend on the quality of the many submodels involved.

9.2 Experimental work

In relation to the performed jet impingement heat transfer investigations in the present work, only few and not very detailed experimental studies of jet impingement heat transfer at high jet Reynolds numbers ($>10^5$) were found in the literature. No studies were found, where a high jet Reynolds number case was combined with a high temperature difference (>1000°C) between jet inlet and wall. It would be relevant to perform such studies, so detailed experimental heat transfer data at these conditions could be obtained. This would be useful in relation to studies in the same area as the present work, and it would also complement the literature on jet impingement heat transfer. It is also encouraged to report details about the turbulence level and the velocity distribution at the nozzle or pipe exit in experimental jet impingement heat transfer investigations to a greater extent. Such data are important in order to be able to impose correct boundary

conditions in CFD simulations when the numerical results should be compared to experimental results. In the performed study, it was often observed that such data were missing in experimental works in the literature on jet impingement heat transfer.

It would also be of interest to perform flame impingement heat transfer measurements in a configuration where a fuel injector is injecting a fuel spray into a high temperature and high pressure environment, which approximates the conditions in the combustion chamber of a large two-stroke marine diesel engine just before the start of the fuel injection. Such experiments could be realized in a rapid compression machine like in the flame impingement heat transfer studies mentioned in section 2.5. Alternatively, a combustion chamber without moving parts could be applied, where the high temperature and high pressure environment is instead achieved by combusting a fuel-air mixture in the chamber prior to the fuel injection. The influence on the piston surface heat transfer of in-cylinder swirl, piston crown material, coatings, etc. may also be investigated in such setups.

Direct instantaneous piston surface heat transfer measurements in large two-stroke marine diesel engines are naturally most desirable, but probably also most complicated and expensive to perform due to the different reasons mentioned in section 1.5. However, such measurements would directly give highly valuable information about the surface heat transfer without the need for approximating the actual in-cylinder conditions during combustion in numerical or experimental setups. Therefore, work with such measurements is encouraged, which could also complement the very limited literature on in-cylinder heat transfer measurements in large two-stroke marine diesel engines.

9.3 Summary

Several further investigations, both numerical and experimental, would be of relevance in relation to the present work as indicated above. Of the suggested numerical studies, the performance of engine cycle CFD simulations for further heat transfer investigations is considered to be most relevant, although the numerical modeling would be complex. The reason is that this approach avoids the difficulties with estimating conditions representative for the actual impingement process in the engine. However, based on the experience obtained in the present study, accurate piston surface heat transfer predictions in the event of impingement of hot combustion products still seem to be challenging for today's CFD software. Hence, the accuracy of piston surface heat transfer results from engine cycle CFD simulations may be questionable. Therefore, continued experimental work on in-cylinder heat transfer measurements in large two-stroke marine diesel engines is perhaps most important, although it is complicated and expensive.

References

[1] (2012, Feb.) U.S. Energy Information Administration. [Online]. http://www.eia.gov/

[2] (2012, Feb.) DieselNet. [Online]. http://www.dieselnet.com/

[3] MAN Diesel & Turbo, "Exhaust Gas Emission Control Today and Tomorrow," MAN Diesel & Turbo, Copenhagen, Denmark, 2009.

[4] (2011, Oct.) Marinediesels.co.uk. [Online]. http://www.marinediesels.info/

[5] MAN B&W Diesel A/S, "Thermo Efficiency System (TES) for Reduction of Fuel Consumption and CO2 Emission," MAN B&W Diesel A/S, Copenhagen, Denmark, 2005.

[6] Heinrich Schmid, "Less Emissions Through Waste Heat Recovery," Wärtsilä Switzerland Ltd., Winterthur, Switzerland, 2004.

[7] C. A. Finol and K. Robinson, "Thermal modelling of modern engines: a review of empirical correlations to estimate the in-cylinder heat transfer coefficient," *Proc. Inst. Mech. Eng. Part D - J. Automob. Eng.*, vol. 220, no. 12, pp. 1765-1781, 2006.

[8] K. Boulouchos, M. K. Eberle, B. Ineichen, and C. Klukowski, "New Insights into the Mechanisms of In-Cylinder Heat Transfer in Diesel Engines," *SAE paper 890573*, pp. 197-215, 1989.

[9] D. Woodyard, *Pounder's Marine Diesel Engines and Gas Turbines*, 9th ed. Great Britain: Butterworth-Heinemann, 2009.

[10] J. B. Heywood, *Internal combustion engine fundamentals*. Singapore: McGraw-Hill, 1988.

[11] S. C. Sorenson, *Engine Principles and Vehicles*. Kgs. Lyngby, Denmark, 2011.

[12] G. Borman and K. Nishiwaki, "Internal-combustion engine heat transfer," *Prog. Energy Combust. Sci.*, pp. 1-46, 1987.

[13] W. Nusselt, "Der Wärmeübergang in der Verbrennungskraftmaschine," *Z. Verdt. Ing.*, vol. 67, pp. 708-711, 1923.

[14] G. Eichelberg, "Some new investigations on old combustion engine problems," *Engineering*, vol. 148, pp. 463-466, 547-550, 1939.

[15] W. J. D. Annand, "Heat transfer in the cylinders of reciprocating internal combustion engines," *Proc. Inst. Mech. Eng.*, vol. 177, no. 36, pp. 973-990, 1963.

[16] G. Woschni, "A Universally Applicable Equation for the Instantaneous Heat Transfer Coefficient in the Internal Combustion Engine," *SAE paper 670931*, pp. 3065-3083, 1967.

[17] T. LeFeuvre, P. S. Myers, and O. A. Uyehara, "Experimental instantaneous heat fluxes in a diesel engine and their correlation," *SAE paper 690464*, 1969.

[18] J. C. Dent and S. J. Sulaiman, "Convective and radiative heat transfer in a high swirl direct injection diesel engine," *SAE paper 770407*, 1977.

[19] K. Boulouchos and D. Brunner, "Assessment of heat transfer models for large, low-speed diesel engines," in *Proceedings of the CIMAC Congress*, London, 1993.

[20] J. M. Desantes, J. Arrègle, and J. J. López, "Scaling laws for free turbulent gas jets and diesel-like sprays," *Atomization Sprays*, vol. 16, pp. 443-473, 2006.

[21] J. V. Pastor, J. J. López, J. M. García, and J. M. Pastor, "A 1D model for the description of mixing-controlled inert diesel sprays," *Fuel*, vol. 87, pp. 2871-2885, 2008.

[22] J. Abraham and V. Magi, "A Virtual Liquid Source (VLS) Model for Vaporizing Diesel Sprays," *SAE paper 1999-01-0911*, 1999.

[23] V. Iyer and J. Abraham, "The Computed Structure of a Combusting Transient Jet Under Diesel Conditions," *SAE paper 981071*, 1998.

[24] V. Iyer and J. Abraham, "Penetration and Dispersion of Transient Gas Jets and Sprays," *Combust. Sci. Technol.*, vol. 130, pp. 315-334, 1997.

[25] F. P. Incropera and D. P. DeWitt, *Introduction to heat transfer*, 4th ed. New York, USA: John Wiley & Sons, 2002.

[26] T. Oguri, A. Takeda, K. Torii, and S. Inaba, "Radiation Heat Transfer of Combustion Flames in a Diesel Engine," *Bull. JSME*, vol. 28, no. 238, pp. 638-655, 1985.

[27] S. Kimura, M. Koike, Y. Matsui, and Y. Enemoto, "Effects of Combustion Chamber Specifications and Swirl Ratio on Transient Heat Transfer and Combustion in a DI Diesel Engine," in *Proceedings of COMODIA 94*, Yokohama, 1994, pp. 589-594.

[28] C. Arcoumanis, P. Cutter, and D. S. Whitelaw, "Heat transfer processes in diesel engines," *Chem. Eng. Res. Design*, vol. 76, pp. 124-132, 1998.

[29] H. Ishii et al., "Heat Loss to The Combustion Chamber Wall with Deposit Adhering to The Wall Surface in D.I. Diesel Engine First Report: Influence of Deposit on Instantaneous Heat Flux into the Piston Surfaces," *SAE paper 2001-01-1811/4231*, 2001.

[30] S. Li, T. Kamimoto, S. Kobori, and Y. Enomoto, "Heat Transfer From Impinging Diesel Flames to the Combustion Chamber Wall," *SAE paper 970896*, pp. 149-162, 1997.

[31] T. Kamimoto, H. Takahashi, H. Kobayashi, and S. Matsuoka, "Convective Heat Transfer of an Impinging Diesel Flame in a Rapid Compression Machine," *SAE paper 821035*, pp. 15-22, 1982.

[32] R. S. Wolf and W. K. Cheng, "Heat Transfer Characteristics of Impinging Diesel Sprays," *SAE paper 890439*, 1989.

[33] Z. Han and R. D. Reitz, "A temperature wall function formulation for variable-density turbulent flows with application to engine convective heat transfer modeling," *Int. J. Heat Mass Transfer*, vol. 40, no. 3, pp. 613-625, 1997.

[34] M. Nuutinen, O. Kaario, and M. Larmi, "Conjugate Heat Transfer in CI Engine CFD Simulations," *SAE paper 2008-01-0973*, 2008.

[35] M. Nuutinen, O. Kaario, and M. Larmi, "Advanced Heat Transfer Modeling with Application to CI Engine CFD Simulations," in *Proceedings of the CIMAC Congress*, Bergen, 2010.

[36] MAN Diesel & Turbo, private communications, 2009.

[37] B. S. Dam, "Experimental and numerical investigations of sprays in two stroke diesel engines," Technical University of Denmark, Lyngby, Ph.D. thesis 2007.

[38] K. Petzold, "Der Wärmeübergang an einer senkrecht angeströmten Platte," *Wiss. Z. Techn. Univ. Dresden*, vol. 13, pp. 1157-1161, 1964.

[39] J. W. Baughn and S. Shimizu, "Heat Transfer Measurements From a Surface With Uniform Heat Flux and an Impinging Jet," *ASME J. Heat Transfer*, vol. 111, pp. 1096-1098, 1989.

[40] J. W. Baughn, A. E. Hechanova, and X. Yan, "An experimental study of entrainment effects on the heat transfer from a flat surface to a heated circular impinging jet," *J. Heat Transfer*, vol. 113, pp. 1023-1025, 1991.

[41] T. H. van der Meer, "Stagnation point heat transfer from turbulent low reynolds number jets and flame jets," *Exp. Therm. Fluid Sci.*, vol. 4, pp. 115-126, 1991.

[42] E. M. Sparrow and B. J. Lovell, "Heat Transfer Characteristics of an Obliquely Impinging Circular Jet," *ASME J. Heat Transfer*, vol. 102, pp. 202-209, 1980.

[43] H. Martin, "Heat and Mass Transfer Between Impinging Gas Jets and Solid Surfaces," *Adv. Heat Transfer*, vol. 13, pp. 1-60, 1977.

[44] R. Viskanta, "Heat Transfer to Impinging Isothermal Gas and Flame Jets," *Exp. Therm. Fluid Sci.*, vol. 6, no. 2, pp. 111-134, 1993.

[45] G. Woschni and K. Huber, "The Influence of Soot Deposits on Combustion Chamber Walls on Heat Losses in Diesel Engines," *SAE paper 910297*, 1991.

[46] J. H. Ferziger and M. Peric, *Computational Methods for Fluid Dynamics*, 3rd ed. Germany: Springer, 2002.

[47] H. K. Versteeg and W. Malalasekera, *An introduction to computational fluid dynamics - The finite volume mehtod*, 2nd ed. Harlow, England: Pearson, 2007.

[48] M. Behnia, S. Parneix, and P. A. Durbin, "Prediction of Heat Transfer in an Axisymmetric Turbulent Jet Impinging on a Flat Plate," *Int. J. Heat Mass Transfer*, vol. 41, no. 12, pp. 1845-1855, 1998.

[49] M. Behnia, S. Parneix, Y. Shabany, and P. A. Durbin, "Numerical Study of Turbulent Heat Transfer in Confined and Unconfined Impinging Jets," *Int. J. Heat Fluid Flow*, vol. 20, no. 1, pp. 1-9, 1999.

[50] H. M. Hofmann, R. Kaiser, M. Kind, and H. Martin, "Calculations of steady and pulsating impinging jets - An assessment of 13 widely used turbulence models," *Numer. Heat Transfer, Part B*, vol. 51, no. 5-6, pp. 565-583, 2007.

[51] ERCOFTAC. (2011) ERCOFTAC Classic Collection Database. [Online]. http://www.ercoftac.org/products_and_services/classic_collection_database/

[52] P. A. Durbin, "Near-Wall Turbulence Closure Modeling Without “Damping Functions"," *Theor. Comput. Fluid Dyn.*, vol. 3, no. 1, pp. 1-13, 1991.

[53] N. Zuckerman and N. Lior, "Impingement Heat Transfer: Correlations and Numerical Modeling," *ASME J. Heat Transfer*, vol. 127, no. 5, pp. 544-552, 2005.

[54] S. Gordeev, V. Heinzel, and V. Slobodchuk, "Simulation of Single and Multiple

Impinging Jet Cooling and Comparison with Experimental Data," in *Proceedings of 8th Biennial ASME Conference on Engineering Systems Design and Analysis, ESDA2006*, Torino, 2006, pp. 143-158.

[55] A. Sveningsson and L. Davidson, "Computations of Flow Field and Heat Transfer in a Stator Vane Passage Using the v2-f Turbulence Model," *ASME J. Turbomach.*, vol. 127, pp. 627-634, 2005.

[56] K. Hermanson, S. Kern, G. Picker, and S. Parneix, "Predictions of External Heat Transfer for Turbine Vanes and Blades With Secondary Flowfields," *J. Turbomach.*, vol. 125, pp. 107-113, 2003.

[57] F. S. Lien, W. L. Chen, and M. A. Leschziner, "Low-Reynolds-Number Eddy-Viscosity Modelling Based on Non-Linear Stress-Strain/Vorticity Relations," in *Proceedings of 3rd Symposium on Engineering Turbulence Modelling and Measurements*, Crete, 1996, pp. 91-100.

[58] V. Yakhot, S. A. Orszag, S. Thangam, T. B. Gatski, and C. G. Speziale, "Development of Turbulence Models for Shear Flows by a Double Expansion Technique," *Phys. Fluids A*, vol. 4, no. 7, pp. 1510–1520, 1992.

[59] CD-adapco, *Methodology, STAR-CD version 4.14*., 2010.

[60] P. A. Durbin, "Separated Flow Computations with the k-ε-v2 Model," *AIAA Journal*, vol. 33, no. 4, pp. 659-664, 1995.

[61] B. E. Launder and D. B. Spalding, "The Numerical Computation of Turbulent Flows," *Comput. Methods Appl. Mech. Eng.*, vol. 3, no. 2, pp. 269-289, 1974.

[62] P. A. Durbin, "On the k-3 stagnation point anomaly," *Int. J. Heat Fluid Flow*, vol. 17, pp. 89-90, 1996.

[63] R. H. Perry, D. W. Green, and J. O. Maloney, *Perry's Chemical Engineers' Handbook*, 6th ed. Singapore: McGraw-Hill, 1984.

[64] S. V. Patankar, *Numerical Heat Transfer and Fluid Flow*. USA: Taylor & Francis, 1980.

[65] CD-adapco, *CCM User Guide, STAR-CD version 4.14*., 2010.

[66] T. J. Craft, L. J. W. Graham, and B. E. Launder, "Impinging jet studies for turbulence model assessment - II. An examination of the performance of four turbulence models," *Int. J. Heat Mass Transfer*, vol. 36, no. 10, pp. 2685-2697, 1993.

[67] X. Yan, J. W. Baughn, and M. Mesbah, "The effect of Reynolds number on the heat transfer distribution from a flat plate to an impinging jet," *ASME Fundamental and Applied Heat Transfer Research for Gas Turbine Engines*, vol. 226, pp. 1-7, 1992.

[68] D. Cooper, D. C. Jackson, B. E. Launder, and G. X. Liao, "Impinging jet studies for turbulence model assessment - I. Flow-field experiments," *Int. J. Heat Mass Transfer*, vol. 36, no. 10, pp. 2675-2684, 1993.

[69] X. Yan, "A preheated-wall transient method using liquid crystals for the measurement of heat transfer on external surfaces and in ducts," University of California, Davis, Ph.D. thesis 1993.

[70] H. M. Hofmann, M. Kind, and H. Martin, "Measurements on Steady State Heat Transfer and Flow Structure and New Correlations for Heat and Mass Transfer in Submerged Impinging Jets," *Int. J. Heat Mass Transfer*, vol. 50, no. 19-20, pp. 3957-3965, 2007.

[71] D. Lee, R. Greif, S. J. Lee, and J. H. Lee, "Heat Transfer From a Flat Plate to a Fully Developed Axisymmetric Impinging Jet," *ASME J. Heat Transfer*, vol. 117, no. 3, pp. 772-776, 1995.

[72] C. den Ouden and C. J. Hoogendoorn, "Local Convective Heat-Transfer Coefficients for Jets Impinging on a Plate: Experiments Using a Liquid-Crystal Technique," in *Proceedings of 5th International Heat Transfer Conference*, New York, 1974, pp. 293-297.

[73] C. J. Hoogendoorn, "The Effect of Turbulence on Heat Transfer at a Stagnation Point," *Int. J. Heat Mass Transfer*, vol. 20, no. 12, pp. 1333-1338, 1977.

[74] B. R. Hollworth and L. R. Gero, "Entrainment Effects on Impingement Heat Transfer: Part II - Local Heat Transfer Measurements," *ASME J. Heat Transfer*, vol. 107, no. 4, pp. 910-915, 1985.

[75] D. Lytle and B. W. Webb, "Air jet impingement heat transfer at low nozzle-plate spacings," *Int. J. Heat Mass Transfer*, vol. 37, no. 12, pp. 1687-1697, 1994.

[76] M. Sibulkin, "Heat Transfer Near the Forward Stagnation Point of a Body of Revolution," *J. Aeronaut. Sci.*, vol. 19, pp. 570-571, 1952.

[77] F. M. White, *Viscous fluid flow*, 2nd ed. Singapore: McGraw-Hill, 1991.

[78] E. R. G. Eckert and R. M. Drake, *Analysis of heat and mass transfer*. Germany: Springer, 1987.

[79] W. M. Kays and M. E. Crawford, *Convective heat and mass transfer*, 3rd ed. USA: McGraw-Hill, 1993.

[80] Y. Shi, A. S. Mujumdar, and M. B. Ray, "Effect of large temperature difference on impingement heat transfer under a round turbulent jet," *Int. Comm. Heat Mass Transfer*, vol. 31, no. 2, pp. 251-260, 2004.

[81] Y. Shi, M. B. Ray, and A. S. Mujumdar, "Effect of large temperature differences on local Nusselt number under turbulent slot impingement jet," *Drying Technol.*, vol. 20, no. 9, pp. 1803-1825, 2002.

[82] H. Schlichting and K. Gersten, *Boundary layer theory*, 8th ed. Germany: Springer, 2000.

[83] E. U. Schlünder and V. Gnielinski, "Wärme- und Stoffübertragung zwischen Gut und aufprallendem Düsenstrahl," *Chem. Ing. Techn.*, vol. 39, no. 9-10, pp. 578-584, 1967.

Appendix A: Dimensionless parameters influencing the Nusselt number

In this appendix, a list is established of dimensionless parameters influencing the wall heat transfer in the jet impingement configuration considered in the present work. An analysis is first performed to establish a general list of dimensionless parameters influencing the wall heat transfer in convective heat transfer problems, whereafter the focus is turned to the specific jet impingement case of the current study.

Equations for mass, momentum and energy conservation can be written in coordinate-free form for a Newtonian fluid as [82]:

$$\frac{D\rho}{Dt} = -\rho\nabla\cdot\vec{v} \tag{A.1}$$

$$\rho\frac{D\vec{v}}{Dt} = \vec{f} - \nabla\mathrm{p} + \nabla\cdot\tau \tag{A.2}$$

$$\rho c_p\frac{DT}{Dt} = \nabla\cdot(\lambda\nabla\mathrm{T}) + \beta T\frac{Dp}{Dt} + \Phi \tag{A.3}$$

$\vec{f}$ denotes body force pr. unit volume, and τ is the viscous stress tensor:

$$\tau = \mu\left(2\dot{\varepsilon} - \tfrac{2}{3}\delta\nabla\cdot\vec{v}\right) \tag{A.4}$$

δ denotes the Kronecker unit tensor, and $\dot{\varepsilon}$ is the strain-rate tensor:

$$\dot{\varepsilon} = \frac{1}{2}[\nabla\vec{v} + (\nabla\vec{v})^T] \tag{A.5}$$

β is the coefficient of thermal expansion defined as:

$$\beta = -\frac{1}{\rho}\left(\frac{\partial\rho}{\partial T}\right)_p \tag{A.6}$$

Φ is the dissipation function:

$$\Phi = \nabla\cdot(\tau\cdot\vec{v}) - \vec{v}\cdot\nabla\cdot\tau \tag{A.7}$$

In the general form of the above equations, the thermophysical properties are variable. Therefore the following equations are added to the system:

$$\mu = f_\mu(T,p) \tag{A.8}$$

$$c_p = f_{c_p}(T, p) \tag{A.9}$$

$$\lambda = f_\lambda(T, p) \tag{A.10}$$

The coefficient of thermal expansion β is given by partial differentiation of the density with respect to the temperature at constant pressure multiplied by the reciprocal of the density, eq. (A.6), and therefore no separate function $f_\beta(T, p)$ for β is required [82]. To close the system of equations, a function relating the density, pressure and temperature is added:

$$\rho = f_\rho(T, p) \tag{A.11}$$

The equation system consisting of eqs. (A.1) - (A.3) and eqs. (A.8) - (A.11) can be non-dimensionalized using the dimensionless quantities:

$$\vec{r}^* = \frac{\vec{r}}{L} \qquad t^* = \frac{tV}{L} \qquad \vec{v}^* = \frac{\vec{v}}{V} \qquad T^* = \frac{T}{T_R}$$

$$p^* = \frac{p}{p_R} \qquad \mu^* = \frac{\mu}{\mu_R} \qquad \rho^* = \frac{\rho}{\rho_R} \qquad {c_p}^* = \frac{c_p}{c_{pR}} \qquad \lambda^* = \frac{\lambda}{\lambda_R}$$

$$\dot{\varepsilon}^* = \frac{L}{V}\dot{\varepsilon} \qquad \beta^* = \beta T_R \qquad \Phi^* = \frac{L^2}{V^2 \mu_R}\Phi \qquad \nabla^* = L\nabla \qquad \frac{D}{Dt^*} = \frac{L}{V}\frac{D}{Dt}$$

L and V are a characteristic length and velocity, respectively. Index R denotes suitable reference values for the flow case. When non-dimensionalized and with $\vec{f} = \rho g \vec{e}_g$, where $\vec{e}_g$ is a unit vector in direction of the gravitational force, and g is the gravitational acceleration, the equation system becomes:

$$\frac{D\rho^*}{Dt^*} = -\rho^* \nabla^* \cdot \vec{v}^* \tag{A.12}$$

$$\rho^* \frac{D\vec{v}^*}{Dt^*} = \frac{1}{Fr^2}\rho^* \vec{e}_g - \frac{p_R}{\rho_R V^2}\nabla^* \mathrm{p}^* + \frac{1}{Re}\nabla^* \cdot \left[\mu^* \left(2\dot{\varepsilon}^* - \tfrac{2}{3}\delta \nabla^* \cdot \vec{v}^*\right)\right] \tag{A.13}$$

$$\rho^* {c_p}^* \frac{DT^*}{Dt^*} = \frac{1}{RePr}\nabla^* \cdot (\lambda^* \nabla^* \mathrm{T}^*) + \frac{p_R}{\rho_R V^2} Ec \beta^* T^* \frac{Dp^*}{Dt^*} + \frac{Ec}{Re}\Phi^* \tag{A.14}$$

$$\mu^* = f_{\mu^*}(T^*, p^*) \tag{A.15}$$

$${c_p}^* = f_{{c_p}^*}(T^*, p^*) \tag{A.16}$$

$$\lambda^* = f_{\lambda^*}(T^*, p^*) \tag{A.17}$$

$$\rho^* = f_{\rho^*}(T^*, p^*) \tag{A.18}$$

The dimensionless characteristic parameters which appear in the dimensionless equations are [82]:

Reynolds number $$Re = \frac{\rho_R V L}{\mu_R} \tag{A.19}$$

Prandtl number $$Pr = \frac{\mu_R c_{pR}}{\lambda_R} \tag{A.20}$$

Froude number $$Fr = \frac{V}{\sqrt{gL}} \tag{A.21}$$

Eckert number $$Ec = \frac{V^2}{c_{pR} T_R} \tag{A.22}$$

The dimensionless equations (A.12) - (A.18) indicate that the dimensionless temperature T^* is a function of different dimensionless parameters:

$$T^* = f_{T^*}(\vec{r}^*, t^*, Re, Pr, Fr, Ec, \frac{p_R}{\rho_R V^2}, f_{\mu^*}, f_{c_p{}^*}, f_{\lambda^*}, f_{\rho^*}) \tag{A.23}$$

The inclusion of $f_{\mu^*}, f_{c_p{}^*}, f_{\lambda^*}$ and f_{ρ^*} in eq. (A.23) is to indicate that the dimensionless state relations will also influence the dimensionless temperature as noted by White [77] and by Eckert and Drake [78]. The dimensionless temperature gradient normal to a wall adjacent to the fluid depends on the same parameters as the dimensionless temperature itself. Thus:

$$\frac{\partial T^*}{\partial n^*} = f_{\partial T^*}(\vec{r}^*, t^*, Re, Pr, Fr, Ec, \frac{p_R}{\rho_R V^2}, f_{\mu^*}, f_{c_p{}^*}, f_{\lambda^*}, f_{\rho^*}) \tag{A.24}$$

n^* denotes the dimensionless wall normal coordinate. Multiplying by $-\lambda^*$ on both sides of eq. (A.24) gives:

$$-\lambda^* \frac{\partial T^*}{\partial n^*} = -\lambda^* f_{\partial T^*}(\vec{r}^*, t^*, Re, Pr, Fr, Ec, \frac{p_R}{\rho_R V^2}, f_{\mu^*}, f_{c_p{}^*}, f_{\lambda^*}, f_{\rho^*}) \tag{A.25}$$

λ^* is a function of T^* and p^* via f_{λ^*} (eq. (A.17)), and T^* and p^* depend on the same parameters as the dimensionless wall normal temperature gradient itself, see eq. (A.23) and eq. (A.24). Eq. (A.25) can therefore be written as:

$$-\lambda^* \frac{\partial T^*}{\partial n^*} = f_{q^*}(\vec{r}^*, t^*, Re, Pr, Fr, Ec, \frac{p_R}{\rho_R V^2}, f_{\mu^*}, f_{c_p{}^*}, f_{\lambda^*}, f_{\rho^*}) \quad \text{(A.26)}$$

where the function f_{q^*} is given by the function $f_{\partial T^*}$ multiplied by $-\lambda^*$. According to Fourier's law, the left hand side of eq. (A.26) is the dimensionless heat flux in the wall normal direction. At the wall, eq. (A.26) gives:

$$\left[-\lambda^* \frac{\partial T^*}{\partial n^*}\right]_w = f_{q^*}(\vec{r}_w^*, t^*, Re, Pr, Fr, Ec, \frac{p_R}{\rho_R V^2}, f_{\mu^*}, f_{c_p{}^*}, f_{\lambda^*}, f_{\rho^*}) \quad \text{(A.27)}$$

The left hand side of eq. (A.27) is thus the dimensionless heat flux at the wall in the wall normal direction, i.e. the dimensionless heat flux from the wall to the fluid. It thus depends on the parameters on the right hand side of eq. (A.27).

The dimensionless heat flux from the wall to the fluid can be rewritten as:

$$\left[-\lambda^* \frac{\partial T^*}{\partial n^*}\right]_w = \frac{L}{\lambda_R T_R}\left[-\lambda \frac{\partial T}{\partial n}\right]_w = \frac{-q_w}{T_R}\frac{L}{\lambda_R} = \frac{T_w - T_\infty}{T_R}\frac{hL}{\lambda_R} = \frac{T_w - T_\infty}{T_R} Nu \quad \text{(A.28)}$$

q_w is the heat flux from the fluid to the wall, T_w denotes the wall temperature, T_∞ is the free stream temperature, and h is the heat transfer coefficient defined by Newton's law of cooling:

$$q_w = h(T_\infty - T_w) \quad \text{(A.29)}$$

The dimensionless parameter Nu in eq. (A.28) is termed the Nusselt number, and it is the dimensionless parameter describing the convective heat transfer to a wall. Combining eqs. (A.27) and (A.28) gives:

$$Nu = f_{Nu}(\vec{r}_w^*, t^*, Re, Pr, Fr, Ec, \frac{p_R}{\rho_R V^2}, \frac{T_w - T_\infty}{T_R}, f_{\mu^*}, f_{c_p{}^*}, f_{\lambda^*}, f_{\rho^*}) \quad \text{(A.30)}$$

Hence, the Nusselt number depends on the parameters on the right hand side of eq. (A.30). The thermal conductivity in the Nusselt number in eq. (A.30) is the reference thermal conductivity λ_R. If instead a different thermal conductivity, say λ_θ, is used in the Nusselt number, then the ratio between λ_R and λ_θ would appear as an additional dimensionless parameter on the right hand side of eq. (A.30). This can be seen by multiplying both sides of eq. (A.30) by the ratio λ_R/λ_θ to replace λ_R by λ_θ in the Nusselt number.

Equation (A.30) is based on the general equation system eqs. (A.12) - (A.18). To describe a specific heat transfer problem, boundary and initial conditions for the dependent variables $\vec{v}^*$, ρ^* and T^* are added to the system. This may result in further dimensionless parameters, present in these conditions, to be included in the function on the right hand

side of eq. (A.30) [82]. If these additional dimensionless parameters are symbolized by $G_{BC,IC}$, then the Nusselt number is given by:

$$Nu = f_{Nu}(\vec{r}_w^*, t^*, Re, Pr, Fr, Ec, \frac{p_R}{\rho_R V^2}, \frac{T_w - T_\infty}{T_R}, f_{\mu^*}, f_{c_p{}^*}, f_{\lambda^*}, f_{\rho^*}, G_{BC,IC}) \qquad \text{(A.31)}$$

If all the parameters on the right hand side of eq. (A.31) are equal for two considered convective heat transfer problems with analogous dimensionless boundary and initial conditions, it is then expected that the Nusselt number will also be the same in the two cases. Based on the Nusselt number, the wall heat flux can then be determined if the wall temperature is known, or vice versa.

The temperature T can be non-dimensionalized by the temperature difference $\Delta T_R = T_w - T_\infty$ instead of by the reference temperature T_R. This may seem inappropriate as the temperature T will then be non-dimensionalized by a temperature difference rather than by an actual temperature. However, by doing so and by non-dimensionalizing β by ΔT_R as well, will result in that the temperature T_R appearing in the Eckert number (eq. (A.22)) will instead be the temperature difference ΔT_R, and eq. (A.22) will then be the usual definition of the Eckert number. Additionally, it will reduce the number of parameters on the right hand side of eq. (A.31) as the ratio $(T_w - T_\infty)/T_R$ will disappear due to the replacement of T_R by ΔT_R in eq. (A.28). Likewise, non-dimensionalizing the pressure p by $\rho_R V^2$ instead of by p_R will also be advantageous in terms of reducing the number of dimensionless parameters in eq. (A.31) as the ratio $p_R/\rho_R V^2$ will then disappear. With these definitions of T^*, β^* and p^*, eq. (A.31) will thus reduce to:

$$Nu = f_{Nu}(\vec{r}_w^*, t^*, Re, Pr, Fr, Ec, f_{\mu^*}, f_{c_p{}^*}, f_{\lambda^*}, f_{\rho^*}, G_{BC,IC}) \qquad \text{(A.32)}$$

The Eckert number appearing in eq. (A.32) is then given by:

$$\text{Eckert number} \qquad Ec = \frac{V^2}{c_{pR}\Delta T_R} \qquad \text{(A.33)}$$

The Nusselt number is often referred to as a dimensionless heat transfer coefficient. If the thermal conductivity in the Nusselt number equals the thermal conductivity of the fluid at the wall, then the Nusselt number can, according to eq. (A.28), additionally be interpreted as the dimensionless temperature gradient at the wall, where the temperature has been non-dimensionalized by the temperature difference $T_\infty - T_w$ [25], [78].

Equation (A.32) for the Nusselt number is a general equation. For the case of a jet impingement configuration, where a round steady gas jet impinges normally onto a plane surface, the Nusselt number has been suggested by Martin [43] to be given by:

$$Nu = f_1(\frac{r}{D}, \frac{H}{D}, Re, Pr) \qquad \text{(A.34)}$$

H is the distance between the surface and the nozzle exit, from where the jet issues, r is the radial distance from the stagnation point, and the characteristic length D is the diameter of the nozzle exit. The characteristic velocity in the Reynolds number is the mean velocity at the nozzle exit. The jet turbulence at the nozzle exit, Tu, has also been suggested as a parameter [72] as well as the dimensionless temperature difference between the jet temperature T_j at the nozzle exit and the ambient gas temperature T_a [83]:

$$\Delta T_{aj,Schlünder}{}^{*} = \frac{T_j - T_a}{T_w - T_a} \tag{A.35}$$

For the present work, it is more convenient to non-dimensionalize the difference between T_j and T_a by the difference between T_j and T_w:

$$\Delta T_{aj}{}^{*} = \frac{T_j - T_a}{T_j - T_w} \tag{A.36}$$

It can be shown that if $\Delta T_{aj,Schlünder}{}^{*}$ is constant for different jet impingement heat transfer cases then $\Delta T_{aj}{}^{*}$ will also be constant. With these additional parameters, the equation for the Nusselt number becomes:

$$Nu = f_2(\frac{r}{D}, \frac{H}{D}, Re, Pr, Tu, \Delta T_{aj}{}^{*}) \tag{A.37}$$

A large temperature variation exists in the jet impingement configuration investigated in the present work and causes a significant variation in the thermophysical properties and in the density. In such cases, it is expected that the influence of the dimensionless state relations $f_{\mu^*}, f_{c_p{}^*}, f_{\lambda^*}$ and f_{ρ^*} is important as well. Therefore, for the case of a jet impingement configuration, where a round steady gas jet impinges normally onto a plane surface, and where a large temperature variation exists, the Nusselt number is expected to be given by:

$$Nu = f(\frac{r}{D}, \frac{H}{D}, Re, Pr, Tu, \Delta T_{aj}{}^{*}, f_{\mu^*}, f_{c_p{}^*}, f_{\lambda^*}, f_{\rho^*}) \tag{A.38}$$

The thermal conductivity in the Nusselt number should be evaluated at the same reference state as the thermophysical properties and the density in the Reynolds and Prandtl numbers. If a different reference state is used, then the ratio between the thermal conductivities evaluated at each reference state should appear as an additional dimensionless parameter on the right hand side of eq. (A.38) as noted below eq. (A.30).

Appendix B: Paper I

ISI Journal Paper

M. V. Jensen and J. H. Walther, "Numerical analysis of jet impingement heat transfer at high jet Reynolds number and large temperature difference", Accepted for publication in *Heat Transfer Engineering*, vol. 34, no. 10, 2013.

Numerical Analysis of Jet Impingement Heat Transfer at High Jet Reynolds Number and Large Temperature Difference

Michael V. Jensen and Jens H. Walther *

Department of Mechanical Engineering,

Technical University of Denmark,

Nils Koppels Allé, building 403,

DK-2800 Kgs. Lyngby,

Denmark

* Also at: Chair of Computational Science, ETH Zürich,

CH-8092 Zürich, Switzerland

Corresponding author is Jens H. Walther:

E-mail: jhw@mek.dtu.dk

Phone: +45 45254327

Fax: +45 45884325

This work was financially supported by MAN Diesel & Turbo

and the Danish Center for Applied Mathematics and Mechanics (DCAMM).

ABSTRACT

Jet impingement heat transfer from a round gas jet to a flat wall was investigated numerically for a ratio of 2 between the jet inlet to wall distance and the jet inlet diameter. The influence of turbulence intensity at the jet inlet and choice of turbulence model on the wall heat transfer was investigated at a jet Reynolds number of 1.66×10^5 and a temperature difference between jet inlet and wall of 1600 K. The focus was on the convective heat transfer contribution as thermal radiation was not included in the investigation. A considerable influence of the turbulence intensity at the jet inlet was observed in the stagnation region, where the wall heat flux increased by a factor of almost 3 when increasing the turbulence intensity from 1.5% to 10%. The choice of turbulence model also influenced the heat transfer predictions significantly, especially in the stagnation region, where differences of up to about 100% were observed. Furthermore, the variation in stagnation point heat transfer was examined for jet Reynolds numbers in the range from 1.10×10^5 to 6.64×10^5. Based on the investigations, a correlation is suggested between the stagnation point Nusselt number, the jet Reynolds number and the turbulence intensity at the jet inlet for impinging jet flows at high jet Reynolds numbers.

INTRODUCTION

Jet impingement flows provide one of the most efficient ways to transfer energy by convection between a gas and a wall when phase change is not employed. Therefore, jet impingement heating and cooling have found widespread use in industrial applications such as material processing and in the manufacturing industry [1]. Jet impingement heat transfer has been investigated intensively over the last four decades, both experimentally

and numerically. Reviews describing the flow physics and proposed heat transfer correlations can be found in [2] and [3]. They treat both round jet and slot jet configurations. Additionally, [3] also includes flame jet impingement heat transfer. Although intensively investigated, most researchers have been focused on jet impingement studies with relatively low to moderate jet Reynolds numbers, i.e. generally below 10^5. These studies also focused almost exclusively on impingement flows with a relative small temperature difference between jet and wall, as also pointed out in [4], and thereby a small variation in temperature and density across the wall boundary layer and in the thermophysical gas properties.

The work presented in this paper is different from these previous works on jet impingement heat transfer by focusing on jet impingement heat transfer at high jet Reynolds numbers and a large temperature variation across the wall boundary layer in a high pressure environment. The motivation for the work was an interest in investigating the heat transfer from combustion gasses to the piston surface in large marine diesel engines during the combustion phase of the engine cycle.

In the present work a hot round turbulent gas jet impinging normally onto a colder flat wall was studied numerically at a high jet Reynolds number and a large temperature difference between jet and wall using the commercial computational fluid dynamics (CFD) code STAR-CD version 4.14. The study focused on the convective heat transfer contribution as thermal radiation was not included in the numerical investigation.

The local heat flux distribution along the wall was obtained as the main parameter of interest. The heat flux distribution was examined for different turbulence intensities at the jet inlet, and the influence on the distribution of applying three different turbulence

models was also studied. Furthermore, the influence of the jet Reynolds number and the turbulence intensity at the jet inlet on the stagnation point heat transfer was investigated. Based on this, a correlation is suggested between the stagnation point Nusselt number, the jet Reynolds number and the turbulence intensity at the jet inlet.

PROBLEM DESCRIPTION

The impinging jet configuration investigated in this study is shown in Figure 1. The impinging jet flow can be divided into three characteristic regions [2]: The free jet region, the stagnation region and the wall jet region. The jet first develops as a free jet in the free jet region, where momentum transfer with the surrounding gas broadens the jet while decreasing the average jet axial velocity. The jet then enters the stagnation region, where it is decelerated in the direction normal to the wall due to the presence of the wall and is turned into an accelerating flow parallel to the wall. The jet then transforms into a decelerating wall jet in the wall jet region due to momentum transfer across its outer boundary to the surrounding gas and due to momentum exchange with the wall. The radial nature of the flow also contributes to the deceleration of the wall jet. In the free jet region the potential core of the jet extends up to about 5 jet inlet diameters (D) from the inlet [5]. While almost constant within the potential core, the turbulence intensity increases after the core region due to the mixing of surrounding gas into the jet, and the axial velocity decreases. The increase in turbulence intensity increases the wall heat transfer in the stagnation region for configurations where the distance between the jet inlet and the wall (H) exceeds the length of the potential core as has been observed experimentally, e.g. [5, 6]. Continuing the increase in distance between the jet inlet and

the wall will lead to a decrease in wall heat transfer again. Additionally, the heat transfer distribution along the wall decreases monotonically if the H/D ratio is large, and it typically shows a non-monotonic behavior with a secondary peak if the H/D ratio is low. The transition is about H/D = 5 and associated with the potential core length.

The dimensions of the system investigated in this work as well as the thermophysical conditions were chosen based on relevant dimensions and conditions in the combustion chamber of a large marine diesel engine during combustion. The jet inlet diameter D was 0.05 m, and the distance between the jet inlet and the wall H was 0.10 m, resulting in a H/D ratio of 2. The jet temperature at the inlet (T_j) was 2273 K, while the wall temperature (T_w) was 673 K. The jet velocity at the inlet (V) was 10 m/s, and the pressure in the system (p) was 180×10^5 Pa. Both the jet and the surrounding fluid were air. These conditions resulted in a jet Reynolds number (Re) of 1.66×10^5, where $Re = \rho V D / \mu$ with the density (ρ) and the viscosity (μ) evaluated at the jet temperature at the inlet (T_j).

NUMERICAL MODEL

The numerical study of the impinging jet problem with dimensions and themophysical conditions as described above was carried out using the commercial CFD code STAR-CD version 4.14. The STAR-CD code employs the finite volume method and a discretisation up to second order of the governing Navier-Stokes equations, mass, energy and turbulence equations. Details on the numerical study are given below.

Geometry and boundary conditions

The impinging round jet configuration was simulated assuming an axisymmetric flow. The dimensions of the computational domain were 2D×6D in the vertical and horizontal directions, respectively. The geometry is shown in Figure 2. All simulations were performed on a cylindrical structured mesh with gradually refined cells in the wall normal direction close to the wall. In the azimuthal direction the grid consisted of only one cell due to the axisymmetric assumption of the configuration investigated. At the jet inlet an inlet boundary condition was imposed with a plug flow into the domain of 10 m/s and a temperature of 2273 K. The plug flow profile was based on a simplification of the turbulent profile of a jet of combustion products impinging on the piston surface in large marine diesel engines during combustion. The turbulence intensity at the inlet was specified to 5%. The turbulence length scale at the inlet was set to 7% of the jet inlet diameter. A no-slip wall boundary condition with a fixed temperature of 673 K was imposed on the bottom of the domain. At the right (outer) face of the domain and on the top of the domain pressure boundary conditions were imposed with a static pressure of 180×10^5 Pa. At the upper pressure boundary the temperature of incoming flow was fixed to 2273 K, which equaled the jet temperature at the inlet. On each side of the domain symmetry boundary conditions were imposed to enforce an axisymmetric flow. The assumption of axis symmetry is customary for round jet impingement configurations where the jet impinges normally onto a surface [7–9]. Further investigation of any 3D effects on the flow field in the present configuration was not performed. The above mentioned values for temperatures, velocity, pressure, turbulence intensity and length

scale were used in the numerical model for the investigations presented below unless otherwise stated.

Governing equations

The governing equations are the steady-state Reynolds-Averaged Navier-Stokes (RANS) equations:

$$\rho(u_j \frac{\partial u_i}{\partial x_j}) = -\frac{\partial p}{\partial x_i} + \frac{\partial}{\partial x_j}(\tau_{ij}) \qquad (1a)$$

$$\tau_{ij} = \mu(\frac{\partial u_i}{\partial x_j} + \frac{\partial u_j}{\partial x_i}) - \tfrac{2}{3}\mu\delta_{ij}\frac{\partial u_k}{\partial x_k} - \rho\overline{u_i' u_j'} \qquad (1b)$$

continuity equation:

$$\frac{\partial}{\partial x_j}(\rho u_j) = 0 \qquad (2)$$

and energy equation:

$$\rho(u_j \frac{\partial h}{\partial x_j}) = \frac{\partial}{\partial x_j}(\lambda \frac{\partial T}{\partial x_j} - \rho\overline{u_j' h'}) + (u_j \frac{\partial p}{\partial x_j}) + \tau_{ij}\frac{\partial u_i}{\partial x_j} \qquad (3)$$

The governing equations are formulated using the Einstein notation, and δ_{ij} is the Kronecker delta, u_i is the velocity component along the i'th coordinate (x_i) direction, and h is the enthalpy. The apostrophe denotes turbulent fluctuations and the overbar time averaged values of the fluctuation products. Variables without apostrophe represent time

averaged values, while turbulent fluctuations in density (ρ), dynamic viscosity (μ) and thermal conductivity (λ) were neglected. The density, dynamic viscosity and thermal conductivity were assumed temperature dependent but independent of pressure as the pressure variation in the impinging jet flow was small. The maximum Mach number in the flow was 0.01, and the incompressible treatment of the flow was therefore acceptable. As indicated by the momentum equation, Eq. (1), buoyancy effects were neglected. Simulations were also performed with buoyancy forces included in the flow calculations. These calculations, however, showed negligible influence of the buoyancy effects on the wall heat transfer due to the high fluid momentum in the flow.

Turbulence modeling

For modeling of turbulence the V2F model [10] was used, which is a RANS type eddy viscosity model. A RANS type eddy viscosity model was selected for two reasons. Firstly because they are less computational expensive than more advanced models such as Reynolds Stress Models (RSM) and Large Eddy Simulation (LES) models. Secondly because the aim of the study was to investigate the time averaged heat transfer in an impinging jet configuration, so instantaneous fluctuating values were not important to resolve. The V2F model does not employ wall functions, so it was necessary with a full resolution of the wall boundary layer (as indicated in Figure 2). The V2F turbulence model has been shown to be one of the most successful RANS type models for predicting heat transfer in impingement jet configurations, also in the stagnation region, where many other RANS type models are known to fail [1, 8-9, 11].

Calculations with other turbulence models were also performed. The models were a low-Re k-ε model [12] and a k-ε RNG model [13] (based on Re-Normalization Group theory) employing wall functions to model the viscous sub-layer of the flow.

Thermophysical properties and density model

Temperature dependent thermophysical properties and density were employed in the numerical model due to the large temperature difference of 1600 K in the investigated configuration. The properties were thermal conductivity (λ), specific heat capacity at constant pressure (c_p) and dynamic viscosity (μ). Polynomial expressions for the temperature dependency were derived based on real gas properties for air cf. [14].

Convergence and discretisation

A global residual tolerance of 10^{-7} was generally needed to ensure convergence of the mass, momentum and heat transfer computations, which typically resulted in more than 50000 iterations before convergence was obtained. The heat flux distribution on the wall was monitored to decide if convergence in the computations was reached. The large number of iterations required to obtain convergence may be due to the application of pressure boundary conditions on large parts of the domain surface and due to the presence of very small cells near the wall in order to resolve the wall boundary layer. The second order central difference scheme was applied for the discretisation of the governing momentum, mass, energy and turbulence equations in the numerical model. This may also have contributed to the need for a large number of iterations before convergence was reached.

RESULTS AND DISCUSSION

Results for the heat flux distribution along the wall are presented in terms of the Nusselt number (Nu) distribution. The Nusselt number is calculated as $Nu = \alpha D / \lambda$, where the heat transfer coefficient α is determined as $\alpha = q_w / (T_j - T_w)$ with q_w being the wall heat flux. λ is evaluated at the jet temperature at the inlet (T_j), consistent with the reference temperature used in the evaluation of the jet Reynolds number.

Validation

A direct validation of the numerical model was not possible as no data obtained in a configuration approximating that of the model were found. Instead predictions obtained with a modified version of the model were compared to experimental heat transfer data of Baughn and Shimizu [6]. In the jet impingement configuration of Baughn and Shimizu, a round air jet issuing from a pipe of 72 pipe diameters impinged normally onto a heated flat plate. The jet Reynolds number in the experiment was 23750, and the investigated H/D ratios were 2, 6, 10 and 14 (only results for H/D = 2 are considered here). The experiment was performed at atmospheric pressure, and the jet temperature at the pipe exit equaled the ambient air temperature. The numerical model was modified to closely approximate the configuration of Baughn and Shimizu in order to avoid differences in the results caused by differences in the configurations. The domain was extended to start two pipe diameters upstream of the pipe exit and hence included a piece of the pipe wall. In radial direction the domain was extended to 10 pipe diameters. A fully developed pipe flow profile, obtained in a separate pipe flow calculation, was imposed as inlet condition.

A constant heat flux was imposed on the wall, the pressure in the domain was 10^5 Pa, and the temperature at the inlet was 293 K, equaling the ambient temperature. Due to small temperature variations in the domain, thermophysical properties were assumed constant (evaluated at 293 K), and the ideal gas law was applied for density evaluation.

The obtained Nusselt number distribution is presented in Figure 3 together with the data of Baughn and Shimizu. In the figure are also included distributions obtained with the two other turbulence models mentioned previously, which are described in [15]: a low-Re k-ε model [12] and a k-ε RNG model [13] applying standard wall functions (WF) [16]. Computations with different turbulence models were performed as impinging jets in general are a difficult class of flows to handle for turbulence models in CFD computations, and hence it was relevant to observe the influence of the models on the heat transfer prediction. The low-Re k-ε model required a resolved wall boundary layer like the V2F model, whereas the k-ε RNG model was less computational demanding due to the application of wall functions and hence was applied on a coarser grid.

The Nusselt number distribution predicted by the numerical model applying the V2F turbulence model was in very good agreement with the experimental data. This is in accordance with previous findings in the literature as mentioned earlier. However, the model overpredicted the Nusselt number in the stagnation region, where the maximum deviation between numerical and experimental data was 15%. The Nusselt number distributions obtained when applying the low-Re k-ε and k-ε RNG models were in poor agreement with the experimental results in the stagnation region. The low-Re k-ε model overpredicted the stagnation point Nusselt number by 133%, and the Nusselt number

distribution predicted by the k-ε RNG model directly showed a wrong tendency in the stagnation region (maximum deviation was -58%).

Based on the results in Figure 3, predictions obtained in the validation study applying the V2F turbulence model were considered reasonable. This was taken as an indication of that the numerical model described in the "Numerical Model" section would produce reliable results. All results presented in the following were obtained with the model described in the "Numerical Model" section.

Grid independency

To examine grid independency in the numerical calculations of the investigated jet impingement configuration, computations were performed on three consecutively refined grids with 600×38 cells, 1200×90 cells and 2400×180 cells in the horizontal and vertical directions, respectively. No grid refinement was performed in the azimuthal direction due to the axisymmetric assumption in the calculations. The obtained Nusselt number distributions are shown in Figure 4. The maximum difference between the Nusselt number distributions obtained on the coarsest grid (600×38 cells) and the finest grid (2400×180 cells) was 9.1%, while the maximum difference was 1.7% between the distributions obtained on the medium refined grid (1200×90 cells) and the finest grid. In the stagnation region, which was of main interest in this work, the three curves nearly coincided with a difference in the distributions of less than 1.1%. Based on these results, the grid consisting of 1200×90 cells was considered to provide sufficient resolution of the computational domain for our investigations. This grid was used in all investigations reported below unless otherwise stated. The highest value of the dimensionless wall

distance $y^+ = y\sqrt{\tau_w \rho}/\mu$ of the near wall cells using this grid was 0.12. τ_w denotes the wall shear stress, and y is the distance to the wall.

Influence of domain extension

Nusselt number distributions obtained on grids with different domain sizes in horizontal direction are shown in Figure 5. Three cases were investigated: a maximum radial distance of r/D = 4, 6 and 10, respectively. The cell density on all three grids was the same. Hence, the grid resolution in the case of a maximum radial distance of r/D = 4, 6, and 10 was 800×90, 1200×90 and 2000×90, respectively. The deviation in the heat transfer predictions obtained on the grids with a maximum r/D of 6 and 10 was small: less than 1.5% for all radial positions. The largest deviation in the heat transfer predictions obtained on the grids with a maximum r/D of 4 and 10 was 4.9%. In the stagnation region, however, all three Nusselt number distributions nearly coincided. Based on this study, the grid with a maximum dimensionless radial distance of 6 was regarded to be sufficient for our purpose. It has previously been reported that for domain sizes larger than r/D = 8 + H/D in the horizontal direction there was no noticeable influence on the flow field and local heat transfer results [11].

Influence of turbulence intensity

The influence of the turbulence intensity at the jet inlet (TI) on the wall heat transfer was investigated by varying the turbulence intensity at the jet inlet boundary from 1.5% to 10%, see Figure 6. It was observed that the turbulence intensity at the jet inlet had a significant influence on the wall heat transfer. The maximum Nusselt number was 387 for

a turbulence intensity of TI = 1.5%, while it was 932 for TI = 10%. A secondary peak in the Nusselt number distribution was clearly observed at r/D = 2.4 for low turbulence intensities, i.e. for TI = 1.5% and TI = 2.5%. For TI = 5%, a secondary peak was also observed although it was weak. In the case of TI = 1.5%, the maximum Nusselt number occurred at the secondary peak, whereas for the other cases it was located at the stagnation point. For TI = 10%, the Nusselt number values decreased monotonically from the stagnation point without any visible secondary peak. The appearance of a secondary peak in the Nusselt number distribution has been reported in previous experimental works, e.g. [6, 17-18], where the location of the peak ranged from r/D = 2.0 to r/D = 2.25, possibly due to different Reynolds numbers. The secondary peak is believed to be caused by a transition from a laminar to a turbulent boundary layer flow [9, 19] or an augmentation of turbulence kinetic energy due to high shear in the region of streamline convergence [7, 11].

The strong influence of the turbulence intensity at the jet inlet on the wall heat transfer emphasizes the importance of knowing this parameter when comparing different experimental measurements or when comparing with numerical results as was also pointed out in [7].

Influence of turbulence model

Computations with the numerical model applying the previously mentioned low-Re k-ε and k-ε RNG turbulence models were performed to study the influence on the heat transfer prediction in the investigated configuration. The low-Re k-ε model was applied on the same grid as that used for the V2F turbulence model (1200×90 cells). The k-ε

RNG model with wall functions was applied on a much coarser grid consisting of 120×35 cells in the horizontal and vertical directions, respectively, without a full resolution of the wall boundary layer. Therefore, in the case of the k-ε RNG model, y^+ values of the near wall cells were between 38 and 77. The computation times showed that the calculations using the k-ε RNG model obtained convergence two orders of magnitude faster than the calculations using the other models. The obtained heat transfer results are presented in Figure 7.

A large variation in the predicted wall heat transfer was observed when applying the different turbulence models, both in magnitudes and trends, as was also found in the validation study. The Nusselt number predictions using the V2F model was first decaying until r/D = 1.6, whereafter a local maximum was seen at r/D = 2.2. The global maximum was at the stagnation point. In the cases of the two other models, the Nusselt number predictions showed a minimum at the stagnation point, and the global maximum was at r/D = 0.5 and r/D = 1.6, respectively, in contrast to the V2F predictions. The magnitude of the Nusselt number differed also greatly between the different model predictions, especially in the stagnation region. Most pronounced were the low-Re k-ε model predictions, which e.g. in the stagnation point resulted in a Nusselt number of 1181. This is 94% higher than the V2F model prediction of Nu = 608 in the stagnation point. Also the Nusselt number prediction in the stagnation point by the k-ε RNG model, Nu = 279, deviated significantly from the V2F model result by -54%.

In summary, the results in Figure 7 emphasize the problem of handling impinging jet flows for the turbulence models, especially in the stagnation region, which was also observed in the validation study. Except for the tendency in the stagnation region Nusselt

number distribution predicted by the low-Re k-ε model, the tendencies in the different Nusselt number distributions shown in Figure 7 are in general similar to those observed in Figure 3. Therefore, of the three turbulence models examined in the present work, the V2F model is considered to provide the most reliable predictions for the investigated jet impingement case.

Stagnation point heat transfer

Wall heat flux distributions were obtained for different variations of the jet velocity at the inlet and the pressure in the numerical model. One parameter was varied at a time while the other was kept at the reference value stated in the model description section. The velocities were of 10 m/s, 20 m/s and 40 m/s, and the pressures were 120×10^5 Pa, 150×10^5 Pa and 180×10^5 Pa. This led to jet Reynolds numbers in the range from 1.10×10^5 to 6.64×10^5. The calculations were performed with a turbulence intensity at the jet inlet of 5%. Additional calculations were performed with turbulence intensities at the jet inlet of 1.5%, 2.5% and 10% at some of the jet Reynolds numbers in order to study the influence on the stagnation point heat transfer. The corresponding stagnation point Nusselt numbers (Nu_0) are plotted against the jet Reynolds numbers in Figure 8.

In the case of a fixed turbulence intensity at the jet inlet, the relationship between the stagnation point Nusselt number and the jet Reynolds number can be approximated by a correlation of the form $Nu_0 = CRe^{\gamma}$, where γ and C are constants, i.e. a linear relationship on the log-log plot in Figure 8. However, for different values of the turbulence intensity at the jet inlet, γ and C vary. Therefore, γ and C should be functions of TI. In the cases of TI = 1.5%, 2.5%, 5% and 10%, the exponent γ was found to be 0.79, 0.84, 0.96 and 1.10,

respectively. The form of the correlation between Nu_0 and Re is similar to that previously found in both experimental and numerical works on jet impingement heat transfer [11, 19, 20]. However, the exponent value, ranging from 0.79 to 1.10, is higher than the values previously reported, which are typically about 0.5. This may be due to the high jet Reynolds number range investigated in this work as the jet Reynolds numbers reported in the previous works were considerably lower (from 4000 to 70000). A higher jet Reynolds number may result in the development of higher turbulence levels when approaching the stagnation point and therefore increased heat transfer. For a purely laminar jet flow, the exponent value has been reported to be 0.5 [20, 21]. Differences in the turbulence intensity at the jet inlet would also influence the stagnation point heat transfer. However, we did not find statements about the turbulence intensity at the jet inlet in the cited works.

The stagnation point Nusselt numbers are plotted against the turbulence intensities at the jet inlet in Figure 9 for the data points in Figure 8 at Re = 1.10×10^5, 1.66×10^5, 3.32×10^5 and 6.64×10^5 in order to study the variation in stagnation point Nusselt number with the turbulence intensity at the jet inlet.

For a fixed jet Reynolds number, a linear relationship is observed between the stagnation point Nusselt number and the turbulence intensity at the jet inlet, thus $Nu_0 = aTI + b$, where a and b are constants. However, for different jet Reynolds numbers, a and b vary. Therefore, a and b should be functions of the jet Reynolds number.

Based on the observed relationships between Nu_0, Re and TI, a correlation is suggested of the form: $Nu_0 = (c_1TI + c_2)Re^{\gamma} + (c_3TI + c_4)$, where c_1, c_2, c_3, c_4 and γ are constants. The correlation was fitted to the data points presented in Figures 8 and 9 to determine c_1, c_2,

c_3, c_4 and γ. A least squares method was applied to minimize the relative error between the stagnation point Nusselt numbers obtained from the simulations and those predicted by the correlation. The resulting correlation is:

$$Nu_0 = (0.103\ TI + 7.41\times10^{-4})Re^{0.96} - (2626\ TI - 124) \quad (4)$$

The correlation is valid for jet Reynolds numbers from 1.10×10^5 to 6.64×10^5 and turbulence intensities at the jet inlet from 1.5% to 10%, given as TI = 0.015 to TI = 0.10 in Eq. (4). Within these limits, the maximum deviation between the stagnation point Nusselt numbers obtained from the simulations and the corresponding Nusselt numbers predicted by the correlation is 7%. Stagnation point Nusselt numbers obtained using the correlation are presented in Figures 8 and 9.

In a previous experimental work by den Ouden and Hoogendoorn [5], a correlation between Nu_0, Re and TI was suggested of the form:

$$Nu_0 = (0.497 + 3.48\times10^{-2}(TI\ Re^{0.5}) - 3.99\times10^{-4}(TI\ Re^{0.5})^2)Re^{0.5} \quad (5)$$

The correlation is apparently valid for jet Reynolds numbers up to 2.64×10^5, turbulence intensities at the jet inlet up to 7.25% and H/D ratios below 4. However, the validity ranges were not clearly stated in [5]. Hofmann et al. [17] recently suggested a correlation for the local Nusselt number Nu in terms of Re, r/D and the Prandtl number ($Pr = \mu c_p/\lambda$), but with no explicit description of the influence of the turbulence intensity at the jet inlet:

$$Nu = 0.055(Re^3 + 10\,Re^2)^{0.25}\,Pr^{0.42}\exp(-0.025(r/D)^2) \quad (6)$$

The correlation of Hofmann et al. [17] was stated to be valid for jet Reynolds numbers between 1.40×10^4 and 2.30×10^5, H/D ratios from 0.5 and up to 10 and r/D ratios up to 8. Hence, the correlation in Eq. (6) is also valid in the stagnation point. No validity range was given for Pr. For comparison, the correlation suggested in the present work (Eq. (4)), the correlation by den Ouden and Hoogendoorn [5] and the correlation by Hofmann et al. [17] have been applied for the jet Reynolds numbers where their validity range overlap, i.e. jet Reynolds numbers between 1.10×10^5 and 2.30×10^5. The turbulence intensity was varied between 2.5% and 7.5%, and as the Prandtl number in all the performed simulations in the present work was 0.67, this value was applied for the correlation in Eq. (6). The resulting stagnation point Nusselt numbers are presented in Figure 10.

Stagnation point Nusselt number predictions obtained by the correlation suggested in the current work (Eq. (4)) are observed to lie above the predictions obtained by the correlation of den Ouden and Hoogendoorn [5] (Eq. (5)) for all three turbulence intensities in the investigated jet Reynolds number range (the average deviation is 43%). Predictions by the correlation of Hofmann et al. [17] are also found to be lower than those of the correlation in Eq. (4). Between TI = 2.5% and TI = 5% (typical intensity range for fully developed pipe flows), predictions by the suggested correlation in Eq. (4) are in average 31% higher than predictions by the correlation of Hofmann et al. [17]. These findings may indicate that the suggested correlation in the present work to some degree overpredicts the stagnation point Nusselt number. An overprediction by the numerical model in the stagnation region was also observed in the validation study.

However, the correlations used for comparison are based on jet impingement heat transfer data obtained in configurations that differ from the configuration investigated in the present work. Considerably lower temperature differences and pressures were present in these configurations, and the jets were issuing from pipe nozzles with fully developed flow profiles, contrary to the investigated case in the present work. A proper evaluation of the suggested correlation needs to be performed against detailed experimental data for conditions similar to those in the investigated configuration.

Besides the investigated effects of Re and TI on the stagnation point Nusselt number, the dimensionless groups Pr and H/D also influence Nu_0, but the influence of these groups was not studied in the present work.

CONCLUSIONS

Jet impingement heat transfer was investigated numerically in a configuration with a high jet Reynolds number and a large temperature difference between jet inlet and wall. The configuration conditions were based on the conditions in a large marine diesel engine during combustion when hot combustion products impinge on the piston surface.

The turbulence intensity at the jet inlet was found to have a pronounced influence on the wall heat transfer, especially in the stagnation region. Additionally, a linear relationship was observed between the Nusselt number in the stagnation point and the turbulence intensity at the jet inlet.

Application of three different turbulence models showed a large variation in both the magnitude and the distribution of the predicted wall heat transfer, especially in the stagnation region.

Furthermore, the variation of stagnation point heat transfer with jet Reynolds number and the turbulence intensity at the jet inlet was investigated. A correlation was suggested for impinging jet flow cases with a jet Reynolds number between 1.10×10^5 and 6.64×10^5 and a turbulence intensity at the jet inlet between 1.5% and 10%. Further experimental validation of the suggested correlation is however needed, which requires detailed experimental data at high jet Reynolds numbers and a large temperature difference between jet inlet and wall.

NOMENCLATURE

c_1,c_2,c_3,c_4	Constants in Nu_0, Re, TI correlation [-]
c_p	Specific heat capacity at constant pressure [J/(kg K)]
D	Jet inlet diameter [m]
H	Distance between jet inlet and wall [m]
h	Enthalpy [J/kg]
Nu	Nusselt number, $Nu = \alpha D / \lambda$ [-]
Nu_0	Stagnation point Nusselt number [-]
p	Pressure [Pa]
Pr	Prandtl number, $Pr = \mu c_p / \lambda$ [-]
q_w	Wall heat flux [W/m^2]
r	Radial distance from center axis [m]
Re	Jet Reynolds number, $Re = \rho V D / \mu$ [-]
T_j	Temperature at jet inlet [K]
T_w	Wall temperature [K]

TI	Turbulence intensity at jet inlet [-]
u_i	Velocity component along the i'th coordinate direction [m/s]
V	Velocity at jet inlet [m/s]
x_i	i'th Cartesian coordinate [m]
y	Wall distance [m]
y^+	Dimensionless wall distance, $y^+ = y\sqrt{\tau_w \rho} / \mu$ [-]

Greek symbols

α	Heat transfer coefficient [W/(m^2 K)]
γ	Exponent in Nu_0, Re, TI correlation [-]
δ_{ij}	Kroneckers delta [-]
λ	Thermal conductivity [W/(m K)]
μ	Dynamic viscosity [N s/m^2]
ρ	Density [kg/m^3]
τ_{ij}	Stress tensor [N/m^2]
τ_w	Wall shear stress [N/m^2]

Superscripts

$\overline{}$	Time averaged value
´	Turbulent fluctuation

REFERENCES

[1] Zuckerman, N., and Lior, N., Impingement Heat Transfer: Correlations and Numerical Modeling, *ASME J. Heat Transfer*, vol. 127, no. 5, pp. 544-552, 2005.

[2] Martin, H., Heat and Mass Transfer Between Impinging Gas Jets and Solid Surfaces, *Adv. Heat Transfer*, vol. 13, pp. 1-60, 1977.

[3] Viskanta, R., Heat Transfer to Impinging Isothermal Gas and Flame Jets, *Exp. Therm. Fluid Sci.*, vol. 6, no. 2, pp. 111-134, 1993.

[4] Shi, Y., Mujumdar, A. S., and Ray, M. B., Effect of Large Temperature Difference on Impingement Heat Transfer Under a Round Turbulent Jet, *Int. Comm. Heat Mass Transfer*, vol. 31, no. 2, pp. 251-260, 2004.

[5] den Ouden, C., and Hoogendoorn, C. J., Local Convective Heat-Transfer Coefficients for Jets Impinging on a Plate: Experiments Using a Liquid-Crystal Technique, *Proceedings of 5th International Heat Transfer Conference*, pp. 293-297, 1974.

[6] Baughn, J. W., and Shimizu, S., Heat Transfer Measurements From a Surface With Uniform Heat Flux and an Impinging Jet, *ASME J. Heat Transfer*, vol. 111, no. 4, pp. 1096-1098, 1989.

[7] Behnia, M., Parneix, S., Shabany, Y., and Durbin, P. A., Numerical Study of Turbulent Heat Transfer in Confined and Unconfined Impinging Jets, *Int. J. Heat Fluid Flow*, vol. 20, no. 1, pp. 1-9, 1999.

[8] Hofmann, H. M., Kaiser, R., and Kind, M., Calculations of Steady and Pulsating Impinging Jets - an Assessment of 13 Widely used Turbulence Models, *Numer. Heat Transfer, Part B*, vol. 51, no. 6, pp. 565-583, 2007.

[9] Gordeev, S., Heinzel, V., and Slobodchuk, V., Simulation of Single and Multiple Impinging Jet Cooling and Comparison with Experimental Data, *Proceedings of 8th Biennial ASME Conference on Engineering Systems Design and Analysis*, *ESDA2006*, pp. 143-158, 2006.

[10] Durbin, P. A., Near-Wall Turbulence Closure Modeling Without "Damping Functions", *Theor. Comput. Fluid Dyn.*, vol. 3, no. 1, pp. 1-13, 1991.

[11] Behnia, M., Parneix, S., and Durbin, P. A., Prediction of Heat Transfer in an Axisymmetric Turbulent Jet Impinging on a Flat Plate, *Int. J. Heat Mass Transfer*, vol. 41, no. 12, pp. 1845-1855, 1998.

[12] Lien, F. S., Chen, W. L. and Leschziner, M. A., Low-Reynolds-Number Eddy-Viscosity Modelling Based on Non-Linear Stress-Strain/Vorticity Relations, *Proceedings of 3rd Symposium on Engineering Turbulence Modelling and Measurements*, 1996.

[13] Yakhot, V., Orszag, S. A., Thangam, S., Gatski, T. B., and Speziale, C. G., Development of Turbulence Models for Shear Flows by a Double Expansion Technique, *Phys. Fluids A*, vol. 4, pp. 1510–1520, 1992.

[14] Perry, R. H., Green, D. W., and Maloney, J. O., *Perry's Chemical Engineers' Handbook*, Sixth edition, McGraw-Hill, Singapore, 1984.

[15] CD-adapco, *Methodology*, *STAR-CD version 4.14*, 2010.

[16] Launder, B. E., and Spalding, D. B., The Numerical Computation of Turbulent Flows, Comput. Methods Appl. Mech. Eng., vol. 3, no. 2, pp. 269-289, 1974.

[17] Hofmann, H. M., Kind, M., and Martin, H., Measurements on Steady State Heat Transfer and Flow Structure and New Correlations for Heat and Mass Transfer in Submerged Impinging Jets, *Int. J. Heat Mass Transfer*, vol. 50, no. 19-20, pp. 3957-3965, 2007.

[18] Petzold, K., Der Wärmeübergang an einer senkrecht angeströmten Platte, *Wiss. Z. Techn. Univ. Dresden*, vol. 13, pp. 1157-1161, 1964.

[19] Lee, D., Greif, R., Lee, S. J., and Lee, J. H., Heat Transfer From a Flat Plate to a Fully Developed Axisymmetric Impinging Jet, *ASME J. Heat Transfer*, vol. 117, no. 3, pp. 772-776, 1995.

[20] Hollworth, B. R., and Gero, L. R., Entrainment Effects on Impingement Heat Transfer: Part II - Local Heat Transfer Measurements, *ASME J. Heat Transfer*, vol. 107, no. 4, pp. 910-915, 1985.

[21] Hoogendoorn, C. J., The Effect of Turbulence on Heat Transfer at a Stagnation Point, *Int. J. Heat Mass Transfer*, vol. 20, no. 12, pp. 1333-1338, 1977.

FIGURE CAPTIONS

Figure 1 Impinging jet configuration.

Figure 2 Computational mesh.

Figure 3 Model predictions vs. experimental data [6] for Re = 23750 and H/D = 2.

Figure 4 Nusselt number distributions obtained on three consecutively refined grids.

Figure 5 Nusselt number distributions obtained on grids with different domain sizes.

Figure 6 Nusselt number distributions obtained for varying degrees of turbulence intensity at the jet inlet.

Figure 7 Nusselt number distributions obtained using different turbulence models.

Figure 8 Stagnation point Nusselt number versus jet Reynolds number.

Figure 9 Stagnation point Nusselt number versus turbulence intensity at the jet inlet.

Figure 10 Stagnation point Nusselt number predictions by different correlations.

Figure 1

Jet impingement sketch

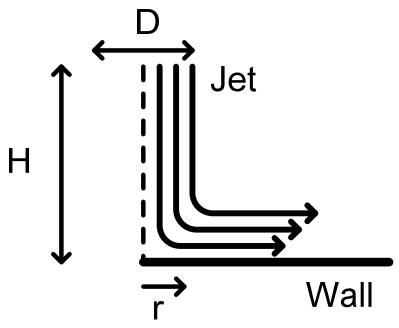

Figure 2

Mesh geometry and boundary conditions applied in the numerical model

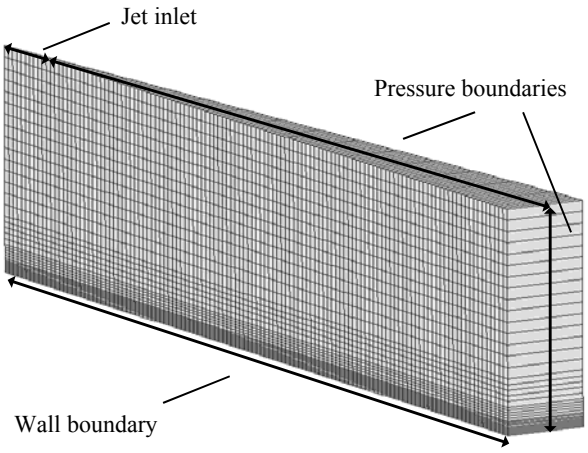

Figure 3

Comparison of experimental and numerical Nusselt number distributions for validation of numerical model

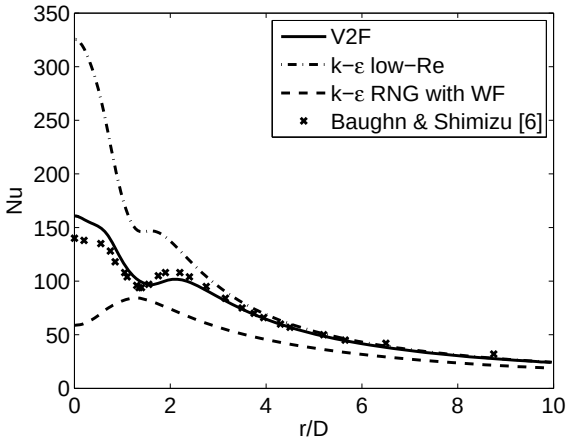

Figure 4

Nusselt number distributions obtained in the grid independency study

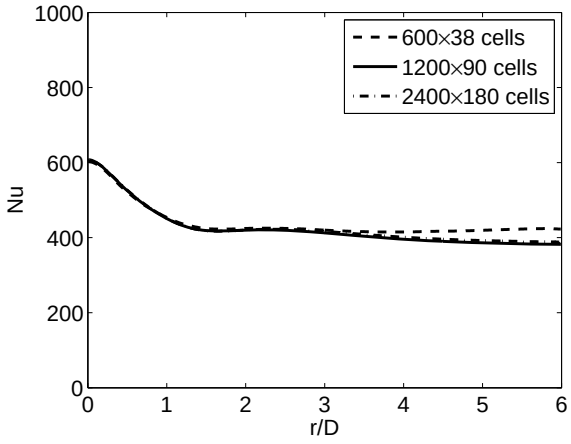

Figure 5

Nusselt number distributions obtained in the domain size study

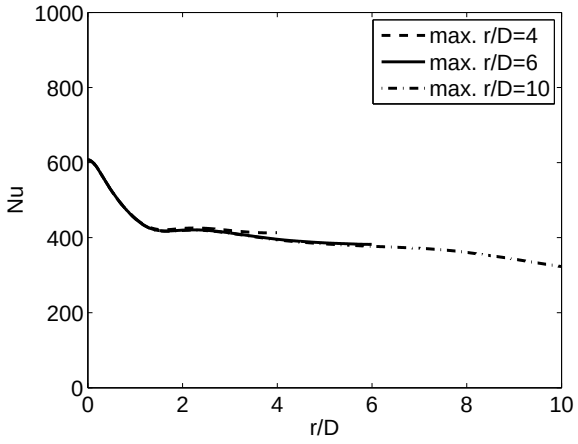

Figure 6

Nusselt number distributions for different degrees of turbulence intensity at the jet inlet

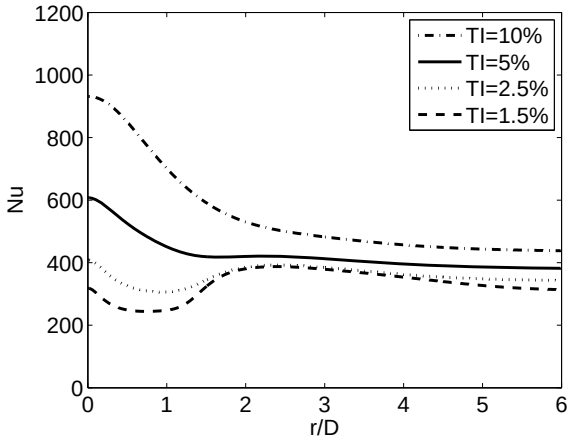

Figure 7

Nusselt number distributions obtained when applying different turbulence models

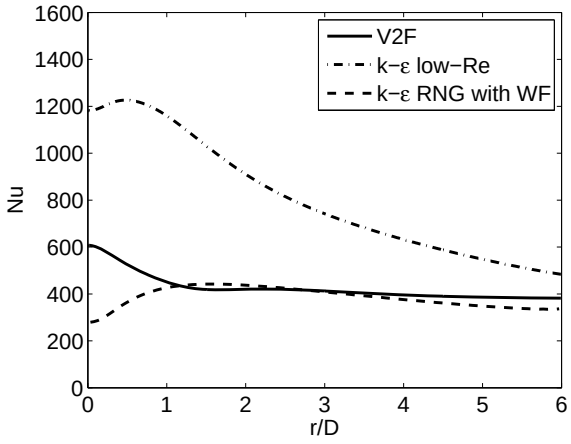

Figure 8

Stagnation point Nusselt number versus jet Reynolds number for different turbulence intensities at the jet inlet

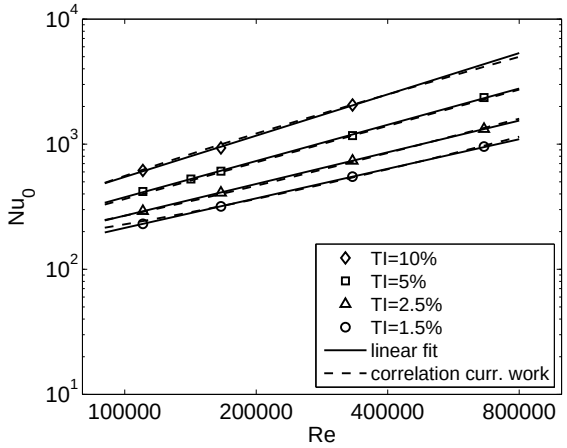

Figure 9

Stagnation point Nusselt number versus turbulence intensity at the jet inlet for different jet Reynolds numbers

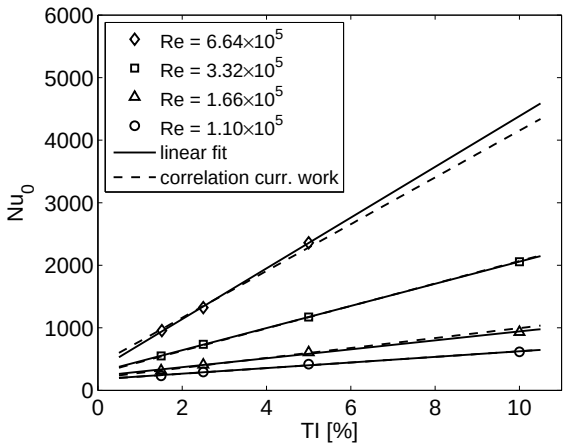

Figure 10

Stagnation point Nusselt numbers predicted by correlation suggested in the current work and by correlations from the literature

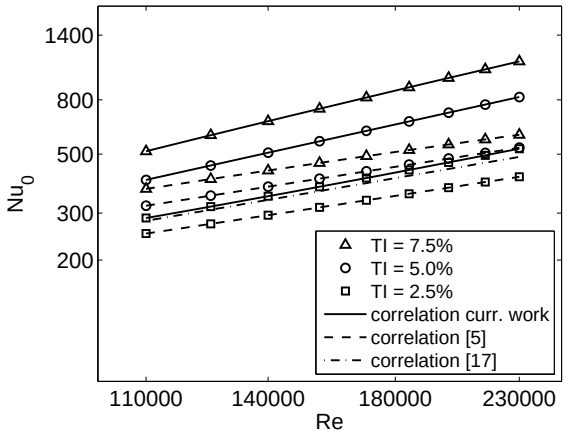

Michael Vincent Jensen is a Ph.D. student at the Department of Mechanical Engineering at the Technical University of Denmark (DTU), Denmark. He received his M.Sc. degree in mechanical engineering in 2006 from the Technical University of Denmark. His research field is heat transfer in large two-stroke marine diesel engines.

Jens H. Walther is associate professor in fluid mechanics at the Technical University of Denmark (DTU), Denmark. He is also a research associate at the Chair of Computational Science at ETH Zurich, Switzerland. He received his Ph.D. in 1994 from the Technical University of Denmark. His main research interests are in numerical fluid dynamics and range from atomistic simulations of fluid flow at the nanoscale to large scale simulations in bluff body aerodynamics.

DTU Mechanical Engineering
Section of Fluid Mechanics, Coastal and Maritime Engineering
Technical University of Denmark

Nils Koppels Allé, Bld. 403
DK- 2800 Kgs. Lyngby
Denmark
Phone (+45) 4525 1360
Fax (+45) 4588 4325
www.mek.dtu.dk
ISBN: 978-87-7475-364-3

DCAMM
Danish Center for Applied Mathematics and Mechanics

Nils Koppels Allé, Bld. 404
DK-2800 Kgs. Lyngby
Denmark
Phone (+45) 4525 4250
Fax (+45) 4593 1475
www.dcamm.dk
ISSN: 0903-1685